

HETEROEPTAXIAL GROWTH OF CHEMICALLY DERIVED $\text{Ba}_2\text{YCu}_3\text{O}_{7-x}$
THIN FILMS

by

PAUL CAMERON MCINTYRE

B.A.Sc., Metals and Materials Engineering
University of British Columbia
(1988)

Submitted to the Department of Materials Science and Engineering
on April 30, 1993 in Partial Fulfillment of
the Requirements for the Degree of

Doctor of Science
in Ceramics
at the

Massachusetts Institute of Technology

June, 1993

© Massachusetts Institute of Technology, 1993. All rights reserved.

Signature of Author _____
Department of Materials Science and Engineering
April 30, 1993

Certified by _____
Michael J. Cima, Norton Associate Professor of Ceramics
Thesis Supervisor

Accepted by _____
Linn W. Hobbs, John F. Elliot Professor of Materials
Chair, Departmental Committee on Graduate Students

ARCHIVES

MASSACHUSETTS INSTITUTE
OF TECHNOLOGY

JUL 30 1993

LIBRARIES

HETEROEPITAXIAL GROWTH OF CHEMICALLY DERIVED $\text{Ba}_2\text{YCu}_3\text{O}_{7-x}$ THIN FILMS

Paul C. McIntyre

Submitted to the Department of Materials Science and Engineering
on April 30, 1993
in partial fulfillment of the requirements for the degree of
Doctor of Science in Ceramics

ABSTRACT

Chemical approaches to oxide thin films based on deposition of metalorganic precursor solutions have been investigated recently because of their potential for producing multi-cation oxide coatings of controlled stoichiometry over large area substrates. A chemical method for synthesizing thin films of $\text{Ba}_2\text{YCu}_3\text{O}_{7-x}$ (BYC) with excellent superconducting properties has been developed by the author and coworkers. This is an *ex situ* method in which the desired oxide phase grows from a metalorganic solution derived precursor film during a high temperature, post-deposition anneal. This thesis reviews important details of the metalorganic solution deposition technique, describes the superconducting properties and morphology of the films, discusses the process of epitaxial nucleation and growth in this system, and characterizes important microstructural defects in the films. The film growth process in this system is compared with the epitaxial grain growth and solid phase heteroepitaxial nucleation and growth mechanisms observed in other chemically derived oxide films.

Nucleation of the epitaxial BYC was studied by cross-section TEM characterization of films deposited on artificially stepped (001) LaAlO_3 substrates. The steps were found to act as preferred sites for nucleation of 90°-misoriented grains in the chemically derived BYC thin films. Comparison with the microstructures of films prepared by *in situ* pulsed laser deposition on the same substrates indicated the growth rate:nucleation rate ratio was higher in the chemically derived films. These studies indicated the importance of the substrate surface in determining the nature of epitaxy in this system. Large native steps may form on nominally flat (001) LaAlO_3 due to shear strain associated with the rhombohedral to cubic phase transformation that occurs in this crystal at ~450°C. These native steps appeared to be responsible for the misoriented (c-axis in-plane) BYC grains observed in the films.

The BYC nucleated heterogeneously on the substrate surface between 720 and 770°C during rapid heating to the annealing temperature of 830°C. The epitaxial film grew from a polycrystalline intermediate that consisted of 20-50 nm diameter Cu- and Y-rich particles and a Ba-rich nanocrystalline phase. The BYC crystallites with c-axis normal to the film plane coalesced early on in the transformation process, and grew more

slowly upward into the overlying polycrystalline material. Epitaxial growth and densification may have been assisted by the transient presence of a liquid phase early in the growth heat treatment. Thermal analysis of the intermediate material detected evidence of partial melting at $\sim 715^{\circ}\text{C}$, under the same $\text{P}(\text{O}_2)$ conditions used in the furnace heat treatments.

Cross-sectional TEM examination of chemically derived films of ~ 80 nm nominal thickness indicates the films are faulted, with numerous polytypoidal stacking faults and anti-phase boundaries. The stacking fault density was found to decrease with increasing distance above the film/substrate interface in several thicker films. The transport J_c ($H_{\text{app}}=0$, $T=77$ K) of films annealed at 830°C in a 250 ppm oxygen atmosphere fell from $> 5 \text{ MA/cm}^2$ to $\sim 1 \text{ MA/cm}^2$ as the film thickness was increased from ~ 80 nm to ~ 500 nm. These observations suggest that extended microstructural defects in the BYC films may play a larger role in flux vortex pinning at low magnetic induction than is commonly recognized.

Thesis Supervisor: Michael J. Cima

Title: Norton Associate Professor of Ceramics

TABLE OF CONTENTS

| | <u>Page #</u> |
|--|---------------|
| TITLE PAGE | 1 |
| ABSTRACT | 2 |
| TABLE OF CONTENTS | 4 |
| LIST OF FIGURES | 6 |
| LIST OF TABLES | 12 |
| ACKNOWLEDGEMENTS | 13 |
| Chapter 1 INTRODUCTION | 14 |
| Chapter 2 BACKGROUND | 19 |
| 2.1 Crystal Structure and Epitaxy of $\text{Ba}_2\text{YCu}_3\text{O}_{7-x}$ | 19 |
| 2.2 BYC Film Deposition Methods | 27 |
| 2.3 Metalorganic Deposition | 31 |
| 2.3.1 Introduction | 31 |
| 2.3.2 MOD Synthesis of BYC Thin Films | 33 |
| 2.3.3 Microstructural Evolution Following MOD | 35 |
| Chapter 3 EFFECTS OF FILM GROWTH CONDITIONS ON PROPERTIES AND MORPHOLOGY | 42 |
| 3.1 Introduction | 42 |
| 3.2 Experimental Procedure | 43 |
| 3.3 Observations | 48 |
| 3.4 Discussion | 65 |
| 3.4.1 Sample Preparation | 65 |
| 3.4.2 Transport Properties and Morphology | 66 |
| 3.5 Summary | 72 |
| Chapter 4 NUCLEATION AND GROWTH OF TFA-DERIVED EPITAXIAL BYC FILMS | 74 |
| 4.1 Background | 74 |
| 4.2 Effect of Substrate Topography on Nucleation | 78 |
| 4.2.1 Introduction | 78 |

| | <u>Page #</u> |
|--|---------------|
| 4.2.2 Experimental Procedure | 81 |
| 4.2.3 Observations | 83 |
| 4.2.4 Discussion | 98 |
| 4.3 Transformation of the TFA-derived Intermediate to BYC | 104 |
| 4.3.1 Introduction | 104 |
| 4.3.2 Experimental Procedure | 105 |
| 4.3.3 Observations | 106 |
| 4.3.4 Discussion | 115 |
| 4.4 Summary | 127 |
| Chapter 5 MICROSTRUCTURAL DEFECTS IN CHEMICALLY DERIVED BYC FILMS | 130 |
| 5.1 Introduction | 130 |
| 5.2 Experimental Procedure | 131 |
| 5.3 Morphological Defects | 132 |
| 5.4 Extended Crystallographic Defects | 141 |
| 5.4.1 Observations | 141 |
| 5.4.2 Discussion | 151 |
| 5.5 Summary | 159 |
| Chapter 6 CONCLUSIONS AND FUTURE WORK | 161 |
| 6.1 Conclusions | 161 |
| 6.2 Future Work | 164 |
| BIBLIOGRAPHY | 168 |

LIST OF FIGURES

| <u>Figure #</u> | | <u>Page #</u> |
|------------------|---|---------------|
| <u>CHAPTER 2</u> | | |
| 2.1 | Crystal structures of a) tetragonal and b) orthorhombic modifications of $\text{Ba}_2\text{YCu}_3\text{O}_{7-x}$, and c) oxygen vacancy ordering in the CuO layers during the <i>t-o</i> transformation. | 20 |
| 2.2 | Schematic representations of a) Frank-van der Merwe, b) Volmer-Weber, and c) Stranski-Krastinov modes of epitaxial growth. | 22 |
| 2.3 | Schematic illustrations of a) epitaxy of the type (001) BYC/(001) LaAlO_3 and b) two-fold epitaxy of BYC on cubic perovskite-like substrates. | 24 |
| 2.4 | Scanning electron photomicrograph of a chemically derived BYC film of 200-250 nm thickness on (001) LaAlO_3 , showing mosaic structure of 90°-misoriented epitaxial crystallites. | 28 |
| 2.5 | Schematic illustrations of <i>in situ</i> a) off-axis magnetron sputtering and b) pulsed laser deposition. | 30 |
| 2.6 | Schematic representation of spin coating a substrate with a metalorganic precursor solution. | 30 |
| <u>CHAPTER 3</u> | | |
| 3.1 | Heating profile for the low temperature heat treatment. | 46 |
| 3.2 | Heating profile for the high temperature (BYC growth and oxygenation) heat treatment. | 46 |
| 3.3 | Effect of furnace oxygen partial pressure on J_c ($H_{app}=0$, $T=77$ K) of films of 200-250 nm thickness annealed at 780°C. | 49 |

| <u>Figure #</u> | | <u>Page #</u> |
|-----------------|---|---------------|
| 3.4 | X-ray diffraction patterns (in the θ - 2θ configuration) for films of 200-250 nm thickness annealed at 780°C in a) 0.032 atm and b) 1000 ppm oxygen atmospheres (balance nitrogen). Unidentified reflections marked by asterisks. | 52 |
| 3.5 | X-ray diffraction a) θ - 2θ scan and b) θ rocking curve (of the (005) BYC reflection) of a TFA-derived film of 70-80 nm thickness annealed at 830°C in 250 ppm oxygen atmosphere. | 53 |
| 3.6 | Rutherford backscattering spectra in random and channeling orientations of TFA-derived films of 200-250 nm thickness annealed at 780°C in a) 0.032 atm and b) 500 ppm oxygen atmospheres. | 55 |
| 3.7 | Plan view SEM micrographs of TFA-derived films of 200-250 nm thickness annealed at 780°C in a) 0.032 atm, b) 3000 ppm, and c) 500 ppm oxygen atmospheres (balance nitrogen). | 56 |
| 3.8 | Fractured cross-section SEM images of the films in Fig. 3.7 annealed in a) 0.032 atm and b) 500 ppm oxygen atmospheres. | 59 |
| 3.9 | Variation in J_c ($H_{app}=0$, $T=77$ K) with film thickness for several sets of annealing conditions. | 60 |
| 3.10 | Plan view SEM micrographs of TFA-derived films of a) 70-80 nm thickness, b) 200-250 nm thickness, and c) ~500 nm thickness annealed at 830°C in a 250 ppm oxygen atmosphere. | 60, 61 |
| 3.11 | Scanning electron micrographs of films of ~350 nm thickness annealed in 250 ppm oxygen atmosphere at a) 780°C and b) 830°C. | 63 |
| 3.12 | Chemically derived films of 70-80 nm thickness annealed in 250 ppm oxygen atmosphere at a) 720°C and b) 830°C. | 64 |

| <u>Figure #</u> | | <u>Page #</u> |
|-----------------|---|---------------|
| 3.13 | Thermogravimetric analysis (TGA) trace including 1st derivative for a dried powder sample of the mixed metal TFA precursor. | 67 |
| 3.14 | Van't Hoff plot of the annealing temperature and $P(O_2)$ conditions investigated in this chapter. | 67 |
| 3.15 | Plot, calculated from data in Fig. 3.9, of current that could potentially be carried in a one micron-wide line of TFA-derived BYC film as a function of film thickness. | 71 |

CHAPTER 4

| | | |
|-----|--|----|
| 4.1 | Idealized structures of [100] 90° grain boundaries in $Ba_2YCu_3O_{7-x}$. | 80 |
| 4.2 | Grain boundary microfacet structures in approximately symmetric (AS) 90° [100] tilt boundaries in BYC. | 80 |
| 4.3 | Scanning electron photomicrographs in a) plan view and b) cross-section of a BYC film deposited <i>in situ</i> by pulsed laser deposition on an artificially stepped single crystal substrate. | 84 |
| 4.4 | Bright field cross-sectional TEM image near the [100] zone axis of a PLD-derived BYC film on artificially stepped (001) $LaAlO_3$. | 85 |
| 4.5 | Higher magnification image of the lower step corner region on the right side of the image in Fig. 4.3. | 87 |
| 4.6 | Cross-sectional bright field image of the PLD-derived film and $LaAlO_3$ step slope above the lower step corner in Fig. 4.3. | 88 |
| 4.7 | High magnification bright field image of $LaAlO_3$ microsteps and 90°-misoriented domains in a PLD-derived film on a step slope. | 90 |

| <u>Figure #</u> | | <u>Page #</u> |
|-----------------|---|---------------|
| 4.8 | Plan view SEM micrographs of TFA-derived films of 200-250 nm nominal thickness deposited on a) artificially stepped and b) nominally flat (001) LaAlO_3 . | 91 |
| 4.9 | Cross-sectional bright field TEM image near the [100] zone axis of a TFA-derived BYC film on stepped (001) LaAlO_3 . | 93 |
| 4.10 | Higher magnification cross-sectional image of the TFA-derived BYC film at the top corner of an artificial step. | 94 |
| 4.11 | Optical photomicrographs taken from different positions on the surface of a TFA-derived BYC film of ~350 nm thickness and a "map" showing the regions of the film from which the images were taken. | 96, 97 |
| 4.12 | Cross-sectional bright field image near the [100] zone axis of a TFA-derived film of ~350 nm thickness showing a nearly- c_1 grain on a LaAlO_3 region containing a large surface step (near the right side of the image). | 101 |
| 4.13 | Optical micrographs of a film of 400-500 nm thickness on nominally flat (001) LaAlO_3 . | 103 |
| 4.14 | X-ray diffraction θ - 2θ scans of films quenched from a) 720°C, b) 770°C, and c) 795°C in the ramp portion of the high temperature heat treatment. | 107 |
| 4.15 | Cross-sectional bright field TEM image of the TFA-derived intermediate film quenched from 720°C. | 109 |
| 4.16 | Cross-sectional image near the [100] zone axis of a TFA-derived BYC film quenched from 770°C. | 110 |
| 4.17 | Image from another region of the specimen shown in Fig. 4.16. | 111 |
| 4.18 | Energy dispersive X-ray spectroscopy maps for barium, yttrium, and copper acquired during STEM imaging of the regions in a) Fig. 4.16 and b) Fig. 4.17. | 113 |

| <u>Figure #</u> | | <u>Page #</u> |
|-----------------|---|---------------|
| 4.19 | Cross-sectional bright field TEM image of a TFA-derived BYC film quenched from 795°C. | 114 |
| 4.20 | Van't Hoff plot showing the temperature/ $P(\text{O}_2)$ dependence of the invariant reactions near $\text{Ba}_2\text{YCu}_3\text{O}_{7-x}$ at subatmospheric oxygen partial pressures (see Table 4.2). | 120 |
| 4.21 | Cross-sectional TEM micrograph of a crystalline inclusion, tentatively identified as $\text{Y}_2\text{Cu}_2\text{O}_5$, and a fluorine-containing amorphous region at the substrate surface. | 122 |
| 4.22 | X-ray diffraction scans of TFA-derived films annealed in a humidified gas mixture containing 250 ppm oxygen at a) 700°C for 2h and b) 830°C for 1h. | 124 |
| 4.23 | Scanning electron photomicrograph of the film annealed at 700°C. | 126 |
| 4.24 | Schematic representation of intermediate film-BYC transformation process. | 128 |

CHAPTER 5

| | | |
|-----|--|-----|
| 5.1 | Field emission SEM image taken at 15 kV of a TFA-derived BYC film of 70-80 nm thickness annealed at 830°C in 250 ppm oxygen. | 133 |
| 5.2 | Plan view bright field TEM micrograph of a BYC film in a region containing a c_{\parallel} grain. | 135 |
| 5.3 | Higher magnification TEM bright field image near the [001] zone axis of the c_{\perp} material surrounding two c_{\parallel} grains. | 136 |
| 5.4 | Cross-sectional TEM image showing a roughly hemispherical second phase particle that was identified as $\text{Y}_2\text{Cu}_2\text{O}_5$ by EDS. | 138 |

| <u>Figure #</u> | | <u>Page #</u> |
|-----------------|--|---------------|
| 5.5 | Annular dark field STEM image of a chemically derived BYC film of 70-80 nm thickness showing second phase particles, and EDS chemical analyses of b) the BYC film, c) a BaSO ₄ surface particle, and d) a CuO particle. | 140 |
| 5.6 | Cross-sectional TEM image near the [010] zone axis of a film of 70-80 nm thickness showing the BYC/LaAlO ₃ interfacial region. | 142 |
| 5.7 | Another region of the specimen shown in Fig. 5.6. | 143 |
| 5.8 | Schematic illustrations of the polytype structures of BYC (213): a) 214 and b) the proposed structure of 224. | 144 |
| 5.9 | High magnification lattice image on the [100] zone axis of a TFA-derived BYC film showing a large intergrowth of the 214-type near the film/substrate interface. | 146 |
| 5.10 | Cross-sectional TEM image of the BYC/LaAlO ₃ interface of a film deposited <i>in situ</i> by pulsed laser deposition. | 147 |
| 5.11 | Cross-sectional TEM micrographs taken from a TFA-derived film of ~350 nm thickness showing a) the film/substrate interface and b) the upper portion of this area of the film. | 148 |
| 5.12 | Cross-sectional TEM image of a specimen similar to the one in Fig 5.11. | 150 |
| 5.13 | Scanning tunneling microscope image of the surface of a TFA-derived film of 70-80 nm thickness. | 155 |
| 5.14 | Schematic depiction of a CuO dislocation formed when a 214-type stacking fault terminates at a region of fault-free 213. | 157 |
| 5.15 | Critical current density (T=77 K) of a TFA-derived film of 200-250 nm thickness annealed at 830°C in 250 ppm oxygen as a function of applied magnetic field for two field orientations: parallel to the (001) plane (90°) and parallel to the c-axis (0°). | 157 |

LIST OF TABLES

| <u>Table #</u> | | <u>Page #</u> |
|------------------|--|---------------|
| <u>CHAPTER 2</u> | | |
| 2.1 | Lattice matched substrates for BYC thin films. | 26 |
| <u>CHAPTER 3</u> | | |
| 3.1 | Superconducting properties of TFA-derived BYC thin films. | 51 |
| <u>CHAPTER 4</u> | | |
| 4.1 | Densities and molecular weights of intermediate phases and $\text{Ba}_2\text{YCu}_3\text{O}_{7-x}$. | 118 |
| 4.2 | Invariant reactions near $\text{Ba}_2\text{YCu}_3\text{O}_{7-x}$ at 850°C. | 118 |
| <u>CHAPTER 5</u> | | |
| 5.1 | Superconducting properties and anisotropy of $\text{Ba}_2\text{YCu}_3\text{O}_{7-x}$. | 133 |

ACKNOWLEDGEMENTS

I am indebted to my advisor, Michael Cima, for his support and guidance, and his constant enthusiasm for this work. I feel very fortunate to have been part of a research group in which the students interact and communicate with their supervisor on a daily basis. I am aware of some of the personal sacrifices that Professor Cima has made to achieve this situation, and I thank him for his commitment to us.

I thank Dr. Wendell Rhine for his advice, friendship, and impromptu chemistry lessons. Wendell has patiently answered my dumb questions for four years and has frequently supplied me with some of "my" best ideas. And where would I be without Dr. Richard Pober, who has enlightened and (often unintentionally) entertained me on so many occasions? Over the years, Wendell and Dick have been important sources of advice and assistance for numerous graduate students in the Ceramics Processing Research Lab. I join a multitude of previous graduates in thanking them for their help.

I thank the other members, past and present, of the Superconductor/Thin Film/Dielectric research group for their assistance and camaraderie: Bertha Chang, Dr. Robert Hallock, Angela Longo, Man Fai Ng, Dr. Simone Peterson, Kevin Ressler, Dr. Maryrose Scozzafava, John A. Smith IV (or is it VI?), and Dr. Neville Sonnenberg. Jack Smith, with help from Bertha, Man Fai, and Lenny Rigione, developed the low temperature heat treatment shown in Figure 3.1 of this thesis. Without this work, I could not have even begun the later studies of nucleation and growth phenomena and structure/property relationships that are described herein. I also acknowledge Lenny's assistance in spin coating most of the thin films discussed in this thesis.

Transmission electron microscopy and STEM were performed at the CMSE electron microscopy facility at MIT. I thank Dr. Tony Garratt-Reed for operating the STEM. I am indebted to Michael Frongillo for instruction and advice in the area of practical electron microscopy. Field emission SEM was performed at the Center for Advanced Materials Research at Brown University, and I acknowledge the assistance of Alan Schwartzman there.

Completing this thesis would not have been possible without having an extensive network of friends with whom I could relax, unwind, and vent my frustrations. I thank Fred Haubensak, Ralph Mason, Rick Mlcak, Rick Constantino, Jack Smith and Fran Justice, Robin Michnick and the other members of the DMSE intramural hockey team, Tom Quinn and the Caustic Rebels, and John Matz for weight-room inspiration.

I would never have made it to MIT without the love, support, and understanding of my family. I thank my parents, Sharon and Bruce McIntyre, for providing my brothers and me with stable and nurturing home environments, despite some difficult circumstances. I also thank my grandparents for spoiling me all these years. Finally, I thank Angela for her love, her emotional support, and for being such a sweetheart.

CHAPTER 1

INTRODUCTION

The discovery in the late 1980's of superconductivity at temperatures above 77 K in several copper-containing multi-cation oxides¹⁻³ prompted a period of intense research activity that continues to this day. Barium yttrium cuprate ($\text{Ba}_2\text{YCu}_3\text{O}_{7-x}$), the 93 K superconductor, has been the most thoroughly investigated of the high temperature superconducting (HTSC) oxides largely because it is easier to prepare as a phase pure material than the higher T_c bismuth- and thallium-based cuprates. This compound's metal ion stoichiometry is fixed at a 2:1:3 Ba:Y:Cu ratio, whereas the metal compositions of the 110 K superconducting BSCCO phase (nominal composition $\text{Bi}_2\text{Sr}_2\text{Ca}_2\text{Cu}_3\text{O}_{10}$) and its thallium analog are quite variable.⁴ An early result of HTSC research was the observation that epitaxial $\text{Ba}_2\text{YCu}_3\text{O}_{7-x}$ (BYC) thin films could support current densities one to two orders of magnitude greater than those of single crystals and several orders of magnitude greater than those of polycrystalline samples prepared by traditional ceramic processing techniques.⁵ Although this behavior has proved to be a serious impediment to the development of large, high-power HTSC components such as superconducting cables, magnets, and electric motors, it has stimulated significant interest in the preparation of BYC thin films.

Several approaches to BYC thin film deposition that yield films with high J_c and low surface resistance at 77 K (for applications in microwave electronics) have been demonstrated. These approaches can be classified as *in situ* methods⁶, in which crystallization of the oxide occurs during deposition on a heated substrate, or *ex situ* methods⁷, in which nucleation and growth of the BYC occur during a post-deposition heat

treatment. Both *in situ* and *ex situ* techniques are capable of producing thin films with excellent superconducting transport properties and many similar microstructural features.⁸

An *ex situ* method for preparing epitaxial BYC thin films through deposition of a metalorganic precursor solution has been developed in our laboratory recently. This metalorganic deposition (MOD) technique produces films with excellent superconducting properties and offers several practical advantages over the better known vacuum-based approaches to BYC films. However, the details of the nucleation and growth process in this BYC film synthesis technique must be better understood if the microstructure and properties of the films are to be controlled. Furthermore, a greater understanding of the microstructural evolution process and its effects on superconducting properties may shed light on important phenomena such as flux vortex pinning in these high T_c cuprates. Finally, it is hoped that knowledge of microstructural evolution in MOD-derived BYC thin films may be of value in understanding similar processes in other multi-cation oxide systems. The purpose of this thesis, therefore, is to investigate heteroepitaxial nucleation and growth and their effects on the microstructures and properties obtained in these MOD-derived $\text{Ba}_2\text{YCu}_3\text{O}_{7-x}$ films.

Scope of this Thesis

The primary goal of this thesis is to characterize the mechanisms by which a polycrystalline intermediate film, derived from thermal decomposition of a metalorganic precursor solution, is transformed to an epitaxial BYC thin film. A secondary goal is to characterize microstructure/property relationships in this system to account for the observed superconducting transport properties. Three experimental approaches were pursued to achieve these objectives.

One extensive series of experiments involved examining the effects of changing post-deposition heat treatment conditions on the film morphology, T_c , and J_c in zero applied field. Preliminary work⁹ had indicated that the annealing (hold) temperature and

oxygen partial pressure in the furnace have the greatest impact on the microstructure and properties of the final BYC films. These processing variables, therefore, were studied most thoroughly. The objective of these experiments was to identify the high temperature heat treatment conditions that produced films with optimum microstructures and superconducting properties, and to infer from the results a rudimentary understanding of the microstructural evolution process.

A second set of experiments focused on nucleation and growth of the BYC in more detail. Preparation of MOD-derived thin films on topographically complex substrates and a comparison with the final microstructures of *in situ*-derived films were performed to study the effect of substrate surface features on nucleation of heteroepitaxial BYC films. In addition, partially transformed specimens were quenched from various points in the growth heat treatment and characterized by X-ray diffraction (XRD) and high resolution transmission electron microscopy (TEM). These experiments followed the phase development process in the intermediate film, identified the temperature/time regime in the heat treatment in which the transformation to BYC occurred, and characterized the changing micro-chemistry of the film during this process. The results obtained in the quenching experiments prompted a differential thermal analysis (DTA) study to investigate possible partial melting at relatively low temperatures in this system.

The third experimental approach involved detailed characterization of microstructural defects in the MOD-derived BYC films. Scanning transmission electron microscopy (STEM) was used to probe the chemistry of second-phase surface particles on the films. Plan view TEM was used to characterize the structure of 90°-misoriented in the films. Field emission SEM and scanning tunneling microscopy (STM) were used to probe the films' fine surface structure. Finally, extended defects within the films were studied by high resolution cross-sectional TEM and their possible role in pinning magnetic flux vortices was analyzed.

Thesis Organization

Chapter 2 is a review of literature that is relevant to microstructural evolution in epitaxial BYC thin films, with emphasis on chemical approaches to these films. The crystal structure of $\text{Ba}_2\text{YCu}_3\text{O}_{7-x}$ and the nature of epitaxy between BYC and several important substrate materials are discussed. A qualitative review of general issues in epitaxial growth is also presented. Both physical and chemical methods for synthesizing BYC thin films are then reviewed. Finally, important issues in microstructural evolution of other MOD-derived oxide thin films are discussed, with attention given to nucleation, epitaxial growth, the presence of intermediate phases, and the development of common microstructural defects.

Chapter 3 describes an experimental study of film growth conditions and their effects on the properties and morphology of the MOD-derived BYC thin films. A reproducible MOD process for synthesizing the films is described in detail. High temperature annealing conditions that result in the growth epitaxial BYC films with excellent superconducting properties are identified. The relationships between the annealing temperature/ $P(\text{O}_2)$ and the properties, crystalline, quality, and microstructure of the films are presented, and the results compared with reports in the literature for other *ex situ*-derived BYC films.

Detailed studies of the epitaxial BYC nucleation and growth processes in these MOD-derived films are presented in Chapter 4. Nucleation was investigated by studying both MOD-derived and *in situ* pulsed laser deposited BYC films that were deposited on the same LaAlO_3 substrates. The substrates had been artificially stepped through an ion etching process to provide locations that were preferred nucleation sites for the film. Differences in the nucleation kinetics of the two film synthesis techniques are inferred from the observed microstructures. The importance of the substrate surface structure in nucleation of 90° -misoriented BYC crystallites on nominally flat (001) LaAlO_3 is also discussed.

Studies of epitaxial growth of the MOD-derived films in which specimens were quenched from the high temperature heat treatment are presented next. The temperature range in which the transformation to BYC occurred, the crystallographic anisotropy of growth rates, and the origin of porosity in the fully-transformed films are discussed. Finally, evidence of transient partial melting in the temperature range over which the transformation takes place is presented, in light of the observations of rapid coalescence of the film following nucleation.

Characterization of the microstructural defects in the fully-converted films is described in Chapter 5. Defects such as pin holes and high angle grain boundaries which reduce the continuity of the superconducting properties are discussed. The origin of the second-phase particles that are observed to decorate the surface of the films is also described. Finally, characterization of extended crystallographic defects, such as stacking faults and anti-phase boundaries, is presented. These defects are significant because they may act as strong flux vortex pinning sites in the films, and their occurrence is likely related to the nature of the epitaxial growth mechanism. The extended defect structure in the MOD-derived is compared to that observed in *in situ* pulsed laser deposited BYC films.

The most important conclusions of the preceding chapters are summarized in Chapter 6. In addition, suggestions for future work related to this thesis research are presented.

CHAPTER 2

BACKGROUND

2.1 CRYSTAL STRUCTURE AND EPITAXY OF $\text{Ba}_2\text{YCu}_3\text{O}_{7-x}$

The crystal structures of the tetragonal (high temperature) and orthorhombic (low temperature) modifications of $\text{Ba}_2\text{YCu}_3\text{O}_{7-x}$ are shown schematically¹⁰ in Figure 2.1a and 2.1b. The unit cells of tetragonal and orthorhombic BYC shown in the figure are composed of three smaller structural units or blocks.¹¹ The central block contains the Y ion and has the formula YCuO_2 ; the adjacent two units along the c-axis contain the BaO layers and have the formula $\text{BaCuO}_{2.5-x/2}$. The oxygen nonstoichiometry in BYC is manifest as oxygen vacancies in the O(1) sites of both the high and low temperature structures. Following growth of BYC at high temperatures, the nonsuperconducting tetragonal phase transforms on cooling to the orthorhombic superconductor through a second order phase transition that involves oxygen uptake and vacancy ordering to produce the CuO chain layers (Fig. 2.1c). Twinning along the {110} planes of orthorhombic BYC occurs to relieve the strain associated with the phase transformation.¹² Barium yttrium cuprate crystals tend to grow as high aspect ratio platelets, with c-axis parallel to the shortest edge of the plates. This crystalline habit is a consequence of the highly anisotropic growth kinetics of BYC, with growth in the a-b plane at least one order of magnitude faster than growth along the c-axis under most growth conditions.¹³ The equilibrium faces of BYC single crystals are the (100), (010), and (001) planes.¹⁴

Epitaxy is defined in this thesis as crystallographic registration of a thin film due to the presence of an underlying single crystal substrate. Three modes of epitaxial growth

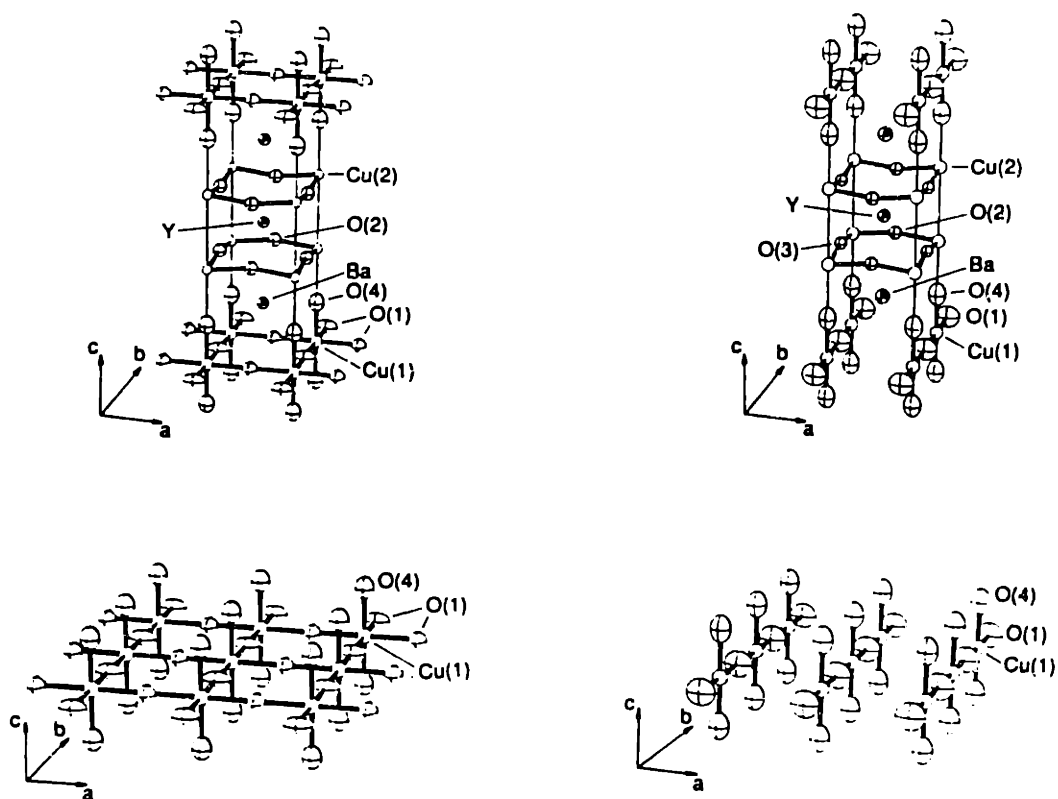


Figure 2.1 Crystal structures of a) tetragonal and b) orthorhombic modifications of $\text{Ba}_2\text{YCu}_3\text{O}_{7-x}$, and c) oxygen vacancy ordering in the CuO layers during the t - o transformation (from reference 10).

are generally recognized.¹⁵ Frank-van der Merwe (FM) growth (or layer-by-layer growth) occurs by step flow in the film plane, with each atomic layer completely covering the substrate before nucleation and growth of the next layer. Volmer-Weber (VM) growth involves nucleation of isolated three dimensional clusters on the substrate with subsequent growth leading to coalescence of the islands. Stranski-Krastinov (SK) growth is an intermediate case between the extremes of FM and VM growth and involves formation of three dimensional islands on a thin, uniform layer of film. The growth modes are illustrated schematically in Figure 2.2.

The growth mode that operates in an epitaxial system depends on the relative surface energies of the film and substrate materials, and on the misfit between film and substrate.¹⁶ The VM growth mode is favored in cases where the balance of the film and substrate surface energies and the film/substrate interfacial energy favors formation of islands, leaving bare portions of the substrate surface. In contrast, epitaxial films that have surface energy less than that of the substrate will tend to form via the FM growth mode.¹⁷ Strain due to coherence between film and substrate in systems with epitaxial misfit will also affect the growth mode. For a film/substrate interface plane that has a square two dimensional lattice and purely dilatational misfit, the misfit ϵ is given by $\epsilon = |a_f - a_s|/a_s$, where a_f and a_s are the lattice parameters (in the interface plane) of the film and substrate, respectively. In FM growth, coherent, elastically strained films form if the misfit does not exceed a critical value ϵ_c .¹⁸ If $\epsilon > \epsilon_c$, epitaxial registry may still exist in the film through the formation of misfit dislocations that relieve strain and allow partial coherence between the film and substrate. The value of ϵ_c depends upon the total strain energy stored in the film and, therefore, is a function of the film thickness. Layer-by-layer growth requires coherence between the film and substrate and is never the equilibrium growth mode in systems with nonzero misfit. Recent theoretical work indicates that the layer-by-layer growth morphology is metastable with respect to formation of three dimensional islands on a thin wetting layer (SK growth).^{19, 20}

Growth of epitaxial BYC thin films has been demonstrated on a number of cubic

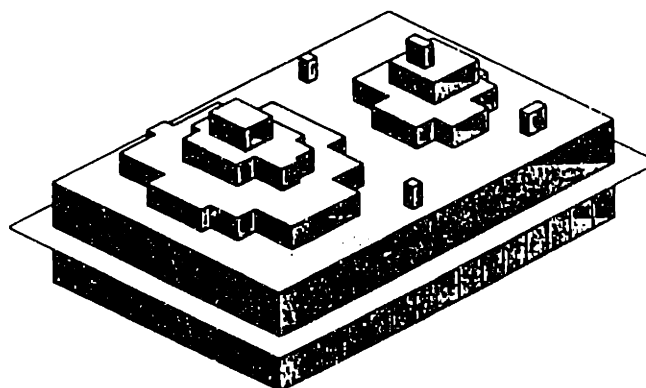
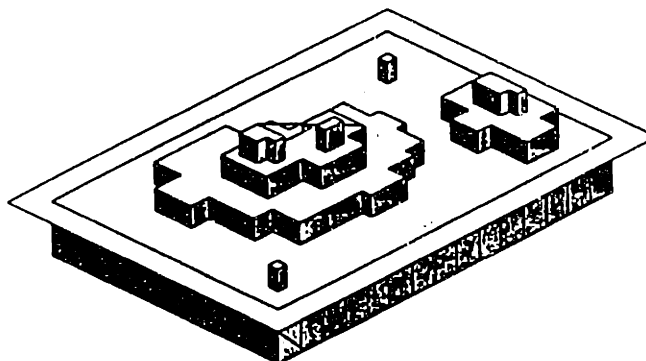
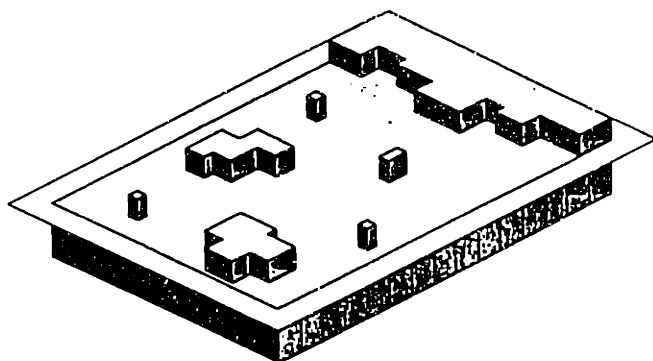


Figure 2.2 Schematic representations of a) Frank-van der Merwe, b) Volmer-Weber, and c) Stranski-Krastinov modes of epitaxial growth (from reference 16).

and near-cubic oxide substrates including SrTiO_3 ²¹, yttria-stabilized-zirconia (YSZ)²², LaAlO_3 ²³, and MgO .²⁴ Most of these materials are well-matched to BYC in terms of their lattice parameters and coefficients of thermal expansion (CTE). Lattice spacings and CTE's for BYC and several substrate materials are compiled in Table 2.1. Magnesium oxide has a room temperature lattice mismatch of $\sim +9\%$ relative to BYC (for growth on (001) MgO , based on epitaxial registry of the type (100) BYC// (200) MgO). This is the largest mismatch of any substrate material used in the growth of high quality BYC thin films. Magnesium oxide has the rocksalt structure and, therefore, its (100) plane does not have the same structure as the (001) BYC plane, although the two crystals share a coincidence site lattice. High resolution TEM studies and studies of the effects of MgO surface structure on BYC orientation suggest growth of BYC thin films on (001) MgO is, in fact, an example of graphoepitaxy.^{25, 26} Steps on the MgO (001) surface have been found to act as preferred nucleation sites for BYC films prepared by pulsed laser deposition, and are believed to determine the final orientation of the film by channeling growth along particular crystallographic directions.²⁶

Lanthanum aluminate is a perovskite-like oxide that is widely used as a substrate material for heteroepitaxial growth of BYC films because of its close lattice match and relatively low dielectric constant (compared to SrTiO_3). A low dielectric constant substrate is desirable for growth of BYC films intended for microwave applications, to avoid dielectric losses. Lanthanum aluminate is a rhombohedral crystal at room temperature that contains a perovskite-like pseudocell.²⁷ The difference between the rhombohedral and the cubic perovskite structures is so small, however, that crystallographic planes and directions quoted for LaAlO_3 are typically referred to a cubic lattice. Therefore, the a-axis lattice parameter listed in Table 2.1 is that of the perovskite-like pseudo-cell at room temperature. The rhombohedral phase undergoes a second order phase transformation to a cubic phase at 450°C .²⁸ Strain associated with the cubic-rhombohedral transformation is accommodated by formation of twins on {100} and {110} planes (referred to the cubic lattice) of the low temperature phase.²⁹ Lanthanum aluminate is one of the least reactive substrate materials used in epitaxial growth of BYC thin films.

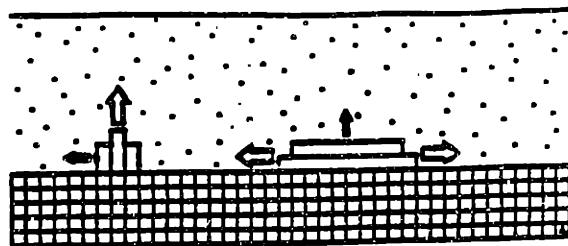
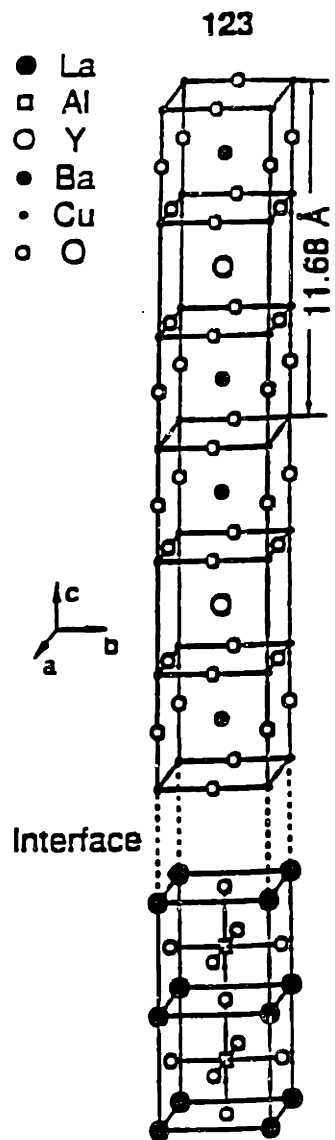


Figure 2.3 Schematic illustrations of a) epitaxy of the type (001) BYC// (001) LaAlO_3 (from reference 31) and b) two-fold epitaxy of BYC on cubic perovskite-like substrates (from reference 13).

In a recent survey of *ex situ* BYC film growth on a variety of substrate materials, Phillips and coworkers³⁰ found that films with high T_c and J_c could be grown on (001) LaAlO_3 at annealing temperatures as high as 950°C. Detailed TEM cross-sectional examination of *in situ* processed BYC films on LaAlO_3 ³¹ failed to detect any evidence of interfacial reaction between the film and substrate. A schematic comparison of the $\text{Ba}_2\text{YCu}_3\text{O}_{7-x}$ unit cell and the LaAlO_3 perovskite pseudocell is shown in Fig.2.3.

Norton and Carter³² studied the effect of substrate type on the coherence of very thin (001)-oriented BYC films. Films were deposited by *in situ* pulsed laser deposition at a substrate stage temperature of 670°C in 350 mTorr of oxygen. The substrate materials investigated were (100) SrTiO_3 , (001) LaAlO_3 , and (100) MgO . Microstructural characterization using plan view TEM indicated the films deposited on MgO grow by the VM mechanism. Discrete islands nucleated which did not coalesce to form a continuous at film thicknesses below 35 nm. Moiré fringe patterns were evident throughout the films on MgO (including films of only ~17 nm thickness), indicating the absence of coherence between the BYC and MgO . A film of 12 nm thickness deposited on SrTiO_3 was continuous, and appeared to consist of islands that had coalesced early in the deposition process. No Moiré fringes were detected in this film, implying that BYC films on (100) SrTiO_3 remain coherent up to a thickness of at least 12 nm. A film of 12 nm thickness deposited on (001) LaAlO_3 had a similar microstructure, except that a network of very finely-spaced Moiré fringes was detected in the images. This result suggests that misfit dislocations are present in (001) BYC films of 12 nm or greater thickness grown on the (001) LaAlO_3 surface.

Early observations^{13, 33} of BYC films grown on lattice-matched perovskite substrates indicated that two-fold epitaxy can occur over a wide range of film growth conditions. Inspection of the lattice parameters listed in Table 2.1 reveals that the c-axis spacing in BYC is approximately 3 times the length of the a- and b-axis lattice spacings. Therefore, based on consideration of the lattice parameters alone, it is not unreasonable that the (001) surfaces of SrTiO_3 and LaAlO_3 (with 0.383 nm and 0.379 nm lattice

Table 2.1: Lattice matched substrates for BYC thin films.

| | Lattice Parameters | | | Mismatch | | | CTE |
|--------------------|--------------------|--------|--------|--------------|--------------|--------------|--------|
| | a | b | c | ϵ_a | ϵ_b | ϵ_c | |
| | nm | nm | nm | % | % | % | ppm/°C |
| SrTiO ₃ | 0.3905 | - | - | +2.0 | +0.7 | +0.1 | 10.4 |
| LaAlO ₃ | 0.3793 | - | - | -0.9 | -2.2 | -3.0 | 11 |
| LaGaO ₃ | 0.3885 | 0.3903 | 0.3885 | +1.5 | +0.7 | -0.5 | 10.3 |
| NdAlO ₃ | 0.3911 | 0.4032 | 0.4075 | +2.2 | +4.0 | +4.4 | |
| NdGaO ₃ | 0.3837 | 0.3889 | 0.3853 | +0.3 | +0.3 | -1.3 | 8.0 |
| YSZ | 0.3607 | - | - | -6.1 | -7.5 | -8.2 | 9.2 |
| MgO | 0.4213 | - | - | +9.2 | +8.0 | +7.4 | 12.6 |
| BYC | 0.3827 | 0.3877 | 0.3903 | - | - | - | 12.0 |

- 1) C-axis lattice parameter listed for BYC is actually c/3.
- 2) CTE for BYC is the average value for a polycrystalline sample.¹⁵⁵
- 3) Data compiled from references 30 and 155.

spacings, respectively) can support epitaxial growth of BYC with both c-axis normal and c-axis in-plane orientations. This is illustrated schematically in Figure 2.4. Close examination of the BYC unit cells shown in Figures 2.1a and 2.1b suggests, however, that significant bond distortions in the CuO_2 layers are required for lattice matching across a (100) BYC/(001) LaAlO_3 interface, implying substantial interfacial strain.

The two-fold epitaxy of BYC on (001) LaAlO_3 results in a granular mosaic microstructure, as shown in Figure 2.5. Platelet-shaped BYC grains oriented with their c-axes in the film plane protrude from the surrounding matrix of c-axis normal BYC. High resolution TEM studies of *in situ* pulsed laser deposited BYC films indicate that these c-axis in-plane outgrowths can also result from nucleation at steps and second-phase particles on the growing BYC surface during deposition.³⁴ Elimination of these misoriented grains is required for use of epitaxial BYC thin films in a variety of technological applications, in part because the high angle grain boundaries that are associated with them may act as weak links for current transport.³⁵

2.2 BYC FILM DEPOSITION METHODS

Future applications of HTSC materials in integrated electronics require the development of deposition techniques that can produce high quality thin films with controlled microstructures and composition. The most thoroughly investigated methods for depositing $\text{Ba}_2\text{YCu}_3\text{O}_{7-x}$ thin films can be classified as physical vapor deposition techniques in which films are deposited by ablation of a target material or by evaporative processes, frequently employing nonthermal sources of energy, inside a vacuum chamber. Examples of physical vapor deposition processes include magnetron sputtering, pulsed laser deposition, molecular beam epitaxy, and electron beam evaporation. In many cases, crystalline films are grown *in situ* in the vacuum chamber by deposition onto heated substrates. In *ex situ* physical deposition processes, amorphous precursor films are deposited onto unheated substrates. Nucleation and growth of the desired crystalline phase occurs in subsequent furnace heat treatments.

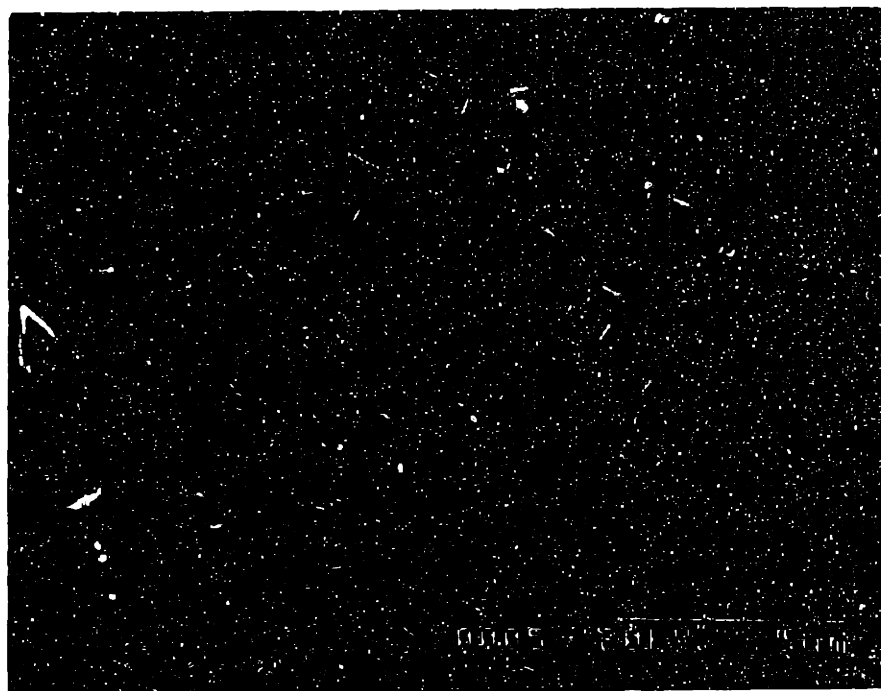


Figure 2.4 Scanning electron photomicrograph of a chemically derived BYC film of 200-250 nm thickness on (001) LaAlO_3 , showing mosaic structure of 90°-misoriented epitaxial crystallites.

The most popular methods for preparing epitaxial BYC thin films are *in situ* pulsed laser deposition and off-axis magnetron sputtering and *ex situ* electron beam coevaporation using BaF_2 as the barium source (the " BaF_2 process"). The *in situ* techniques (illustrated schematically in Fig. 2.6) have several advantages. They are capable of growing epitaxial superlattice structures with abrupt interfaces between adjacent layers, and, by condensing the film directly from the vapor, they may produce metastable phases with unique properties.³⁶ The disadvantages associated with the physical vapor deposition methods are most significant when one considers using these techniques to manufacture large numbers of devices. Control of overall film composition can be problematic due to variations in evaporation/ablation rates from the multiple sources that are often required to deposit multi-cation oxides. Control of oxygen stoichiometry is also an issue because of the low pressures required by many of the deposition systems. Composition and temperature control across the surface of the film is an additional challenge. In *in-situ* film growth in high vacuum, maintaining reproducibly good thermal contact between the substrate heater and the substrate can be a significant problem³⁷. The use of transparent oxide substrate materials makes it difficult to thermally couple to the film in vacuum. Substrate temperatures can vary by more than 100°C depending on the quality of the thermal contact. Local variations in film composition and structure can occur due to the geometry of the vapor plume relative to the substrate, or, in methods like pulsed laser ablation, due to the presence of particulate contamination from the target ablation process. The economics of integrated electronics fabrication require that device-quality BYC thin films be deposited uniformly over large area substrates (often, greater than 10 cm diameter).

Chemical synthesis techniques are alternative approaches to thin film growth that include chemical vapor deposition (CVD) and metalorganic deposition (MOD). In CVD, a volatile precursor compound is evaporated and transported to a heated substrate via a carrier gas. Film growth occurs through heterogeneous chemical reactions at the substrate surface, or through homogeneous reactions in the gas phase above the substrate.³⁸ Metalorganic deposition involves preparation of inorganic thin films from metalorganic

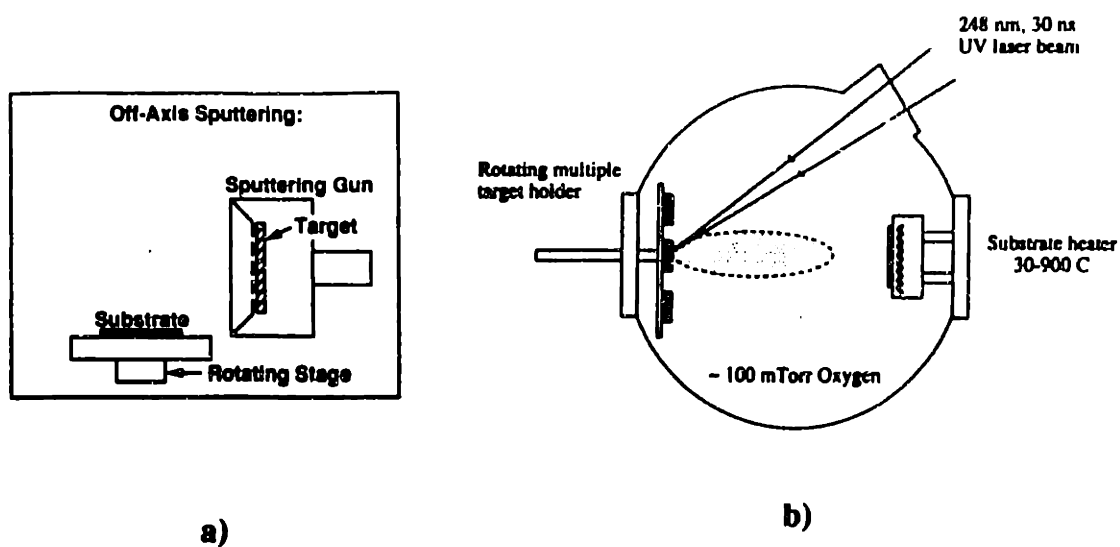


Figure 2.5 Schematic illustrations of *in situ* a) off-axis magnetron sputtering and b) pulsed laser deposition (from reference 138).

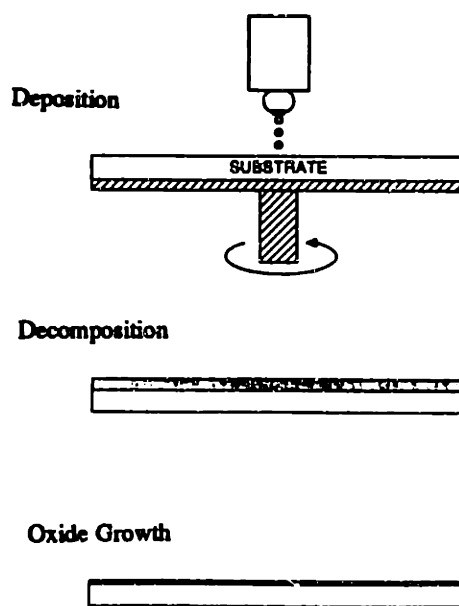


Figure 2.6 Schematic representation of spin coating a substrate with a metalorganic precursor solution (from reference 39).

precursor solutions.³⁹ Typically, metal carboxylates or alkoxides dissolved in an organic solvent are deposited onto polished substrates by dip coating or by spin coating with a photoresist spinner (see Fig. 2.7). This is an *ex situ* process in the sense that the final oxide film grows during a post-deposition furnace heat treatment. This thesis focuses on thin film growth via MOD. Further references to chemical methods in the text are intended to apply only to synthesis of BYC films through deposition of metalorganic precursor solutions, not through CVD.

2.3 METALORGANIC DEPOSITION

2.3.1 Introduction

Growth of crystalline thin films from metalorganic solution precursors can occur following thermal decomposition or pyrolysis of the precursor compounds (metalorganic decomposition), or following condensation and drying of colloidal or polymeric gels (the sol-gel approach). In both cases, the precursor compounds and solvents are selected so as to enhance precursor solubility and substrate wetting and to discourage the formation of undesirable intermediate compounds during heat treatment.⁴⁰ The precursor compounds must be highly soluble in the chosen solvent to avoid crystallization as the green films dry during dip coating or spin coating. In multiple cation systems, crystallization causes segregation of the cationic species in the green films, destroying the microscopic homogeneity of the films. Moreover, many of the precursor compounds used in sol-gel methods are highly air sensitive.⁴¹ Spin coating and dip coating operations using metal alkoxide solutions, for example, are typically performed in dry nitrogen environments to prevent uncontrolled hydrolysis or reaction with CO₂.

The mechanical behavior of the films during solvent evaporation and precursor decomposition is also an important issue. In the metalorganic decomposition process, the green films will commonly lose more than 50% of their starting weight during heating to 400°C. The associated volume change can lead to cracking on both macroscopic and

microscopic length scales, and uncontrolled evolution of gaseous decomposition products can cause blistering and delamination of the films.⁴² In the sol-gel process, intentional hydrolysis of the precursor solution prior to deposition causes condensation of a gel film with intimate mixing of cations, as long as the various cationic species hydrolyze at similar rates.⁴³ The condensation reactions cause the green film to become brittle and subject to cracking during the shrinkage that occurs in post-deposition heat treatments.⁴⁴ Cracking due to shrinkage of a gel film on a constraining substrate creates a thickness limitation for oxide films derived from a single coating of precursor. Thicker films can be prepared by multiple coating/baking operations or by modifying the precursor chemistry to reduce the rate of gelation relative to solvent evaporation.⁴⁵ These chemical and mechanical issues limit the number of technically feasible precursor systems for preparation of high quality oxide thin films via MOD.

The primary advantages of chemical synthesis techniques for preparing oxide thin films are control of overall film composition and uniformity of composition across the film. These are particularly important issues in the growth of the multi-cation HTSC oxides. Growth of the desired oxide occurs in a furnace heat treatment at essentially atmospheric pressure; thus temperature control is much easier than in *in situ* film growth. Deposition of metalorganic precursors is suitable for preparation of large area films. In addition, epitaxial growth of oxide thin films using chemical deposition techniques has been demonstrated by several investigators.⁴⁶⁻⁴⁸

The disadvantages of the precursor solution route include a tendency to develop significant porosity in the oxide films due to the substantial film density changes in the drying, decomposition, and crystallization processes. In order to densify the films, extended heat treatments at relatively high temperatures ($> 800^{\circ}\text{C}$) may be required, possibly causing substrate/film reactions.

The remainder of this chapter reviews the film growth process in MOD-derived multi-cation oxides. Many of the published studies of chemical synthesis of oxide thin

films have emphasized the details of precursor synthesis, film forming and drying, and precursor decomposition chemistry. The focus here is on microstructural evolution during the post-deposition anneal at elevated temperatures.

2.3.2 MOD Synthesis of BYC Thin Films

Chemical methods for preparation of BYC thin films have been investigated almost since the date of the compound's discovery.^{49, 50} Most of the work in this area focused on oxide growth via metalorganic decomposition because of the difficulty in obtaining soluble copper alkoxides for sol-gel syntheses.⁵¹ Gross and coworkers⁵² reported the preparation of BYC films on MgO and ZrO₂ substrates by spin coating solutions of mixed-metal 2-ethyl hexanoates in chloroform. Crack-free films were produced by adjusting the solution concentration so that the final film thickness was less than 1 μm . The films were calcined at temperatures between 800°C and 990°C in flowing oxygen to decompose the precursor and form the tetragonal Ba₂YCu₃O_{7-x} phase, and were then annealed at 400°C in oxygen to transform to the orthorhombic phase. The fired films were textured with the c-axis of the defect-perovskite unit cell normal to the film plane. Zero resistance was reported at 77 K and the J_c was approximately 10⁴ A/cm² at 65 K in the absence of an applied field. More recent work by Chu et al.⁵³ focussed on synthesis of BYC films on LaAlO₃ single crystal substrates through metalorganic decomposition of metal trimethylacetate solutions. The authors reported T_c ($R=0$) of 87.8 K and J_c (transport) in excess of 10⁵ A/cm² at 77 K for a specimen annealed in a multi-step heat treatment that included a 10 min hold at 920°C in a mixed N₂/O₂ atmosphere containing 0.01 atm oxygen.

A problem that has been common to almost all chemical synthesis routes to BYC films has been the stability of BaCO₃, which forms as an intermediate compound during the decomposition of most of the metalorganic precursors investigated or due to carbon residues in precursor gels.⁵⁴⁻⁵⁶ Thermal decomposition of this phase frequently requires extended annealing at high temperatures which can promote film/substrate reaction or

undesirable microstructural changes in the BYC film. Chen et al.⁵⁷ prepared Ba-Y-Cu-O and Ba-Yb-Cu-O films on (211) and (100) SrTiO₃ single crystal substrates by MOD of the metal neodecanoates dissolved in xylene and pyridine. Thin films were fired in oxygen using one of two different methods: (1) furnace annealing at 850°C-880°C for 6h followed by slow cooling to room temperature, and (2) rapid thermal annealing (RTA) at 850°C for 60 s, cooling to room temperature, and then RTA at 920°C for 30 s followed by cooling to room temperature. X-ray diffraction of the furnace-annealed films detected the presence of BaSrYCu₃O₇, presumably formed by reaction between the film and substrate during the long high temperature hold. This phase was not observed in the RTA-processed films which had strong c-axis-normal preferred orientation and much sharper resistive transitions than the furnace-annealed samples. Hirano et al.⁵⁵ used dilute metalorganic precursor solutions to prepare Ba₂YCu₃O_{7-x} films on (100) MgO and SrTiO₃ substrates by dip coating. Heat treatments were performed in a mixed ozone/oxygen furnace atmosphere to aid in the decomposition of BaCO₃. The low measured critical temperatures (zero resistivity below 75 K) and broad resistive transitions were attributed to composition changes due to excessive substrate/film reaction.

A fluorinated precursor for BYC film preparation that avoids formation of a BaCO₃ intermediate was initially investigated by Gupta and coworkers.⁵⁸ Subsequent work in our laboratory has demonstrated the production of epitaxial thin films with excellent superconducting properties through spin-on deposition and decomposition of this precursor.^{9, 48} The trifluoroacetate (TFA) salts of barium, yttrium, and copper are highly soluble in water and methyl alcohol and dry to a glass during spin coating. The as-deposited TFA precursor films are thermally decomposed to oxy-fluoride intermediate films by slowly heating to 400°C in humid oxygen. These intermediate films are subsequently converted to crystalline oxide films of the tetragonal modification of BYC through reaction with water vapor injected into the furnace atmosphere during a high temperature (> 700°C) anneal. The high-T_c orthorhombic phase is then obtained by slow cooling in dry oxygen below 525°C.

2.3.3 Microstructural Evolution Following MOD

Nucleation and growth

Nucleation in thin film materials is frequently controlled by the presence of the substrate surface. Heterogeneous nucleation at interfaces can significantly reduce the crystallization temperature in solid state systems.⁵⁹ The areal density and locations of preferred sites for heterogeneous nucleation on a substrate can determine the final average grain size and size distribution in a thin film. Tuttle et al.⁶⁰, in a study of chemically derived $\text{Pb}(\text{Zr}, \text{Ti})\text{O}_3$ (PZT) thin films grown on platinized, SiO_2 -coated Si(100) wafers, observed heterogeneous nucleation of perovskite PZT spherulites on platinum crystallites on the substrate surface. Kwok and Desu⁶¹ found a polycrystalline PbTiO_3 (PT) "seed layer" deposited onto single crystal sapphire substrates lowered the temperature of transformation from the intermediate pyrochlore phase to the ferroelectric perovskite phase of $\text{PbZr}_{.53}\text{Ti}_{.47}\text{O}_3$ by as much as to 100°C . The microstructure of the sol-gel derived PZT film mimicked that of the PT seed layer (similar grain size and grain size distribution) although the average grain size in PZT films deposited directly onto sapphire and heat treated identically was an order of magnitude larger ($\sim 3 \mu\text{m}$). These observations suggest the seed layer provided a large number of nucleation sites for the perovskite PZT film. The final grain size was apparently determined by impingement of crystallites that had nucleated at the surfaces of grains in the seed layer. Further grain growth would have required extended annealing at high temperatures.⁶²

Growth of a good quality epitaxial film requires heterogeneous nucleation to create the desired crystallographic orientation. The results of Nashimoto and coworkers⁶³ indicate prehydrolysis of sol-gel precursors for lithium niobate destroys epitaxy in the final oxide films. This phenomenon can be explained based on the nucleation process in the films. Prehydrolysis of alkoxide precursors in the sol-gel method is a common technique for reducing the amount of residual organic material present in chemically derived films prior to thermal treatment. This procedure is often intended to avoid the

formation of stable carbon-containing intermediate compounds and to reduce the crystallization temperature of the oxides.^{64, 65} However, a number of investigators have reported that prehydrolysis of sol-gel precursors adversely affects the crystallization of oxide thin films. Nashimoto⁶³ and Endo⁶⁶ reported increased film roughness and loss of preferred orientation in niobate films deposited on lattice matched oxide substrates using prehydrolyzed solutions. Joshi et al.⁶⁷ found sol-gel derived LiNbO_3 films became increasingly porous and inhomogeneous with increasing solution prehydrolysis. Amini and Sacks⁶⁸ reported that solution prehydrolysis weakened crystallization of KNbO_3 , and Chen et al.⁶⁹ reported loss of crystallographic orientation in PbTiO_3 thin films with increasing hydrolysis of the precursor. This behavior appears to be related to the homogeneity of the green film that results from precursor deposition. Prehydrolysis of the moisture sensitive alkoxides forms a sol. When deposited onto the substrate, the particles in the precursor sol may provide sites for preferential nucleation of the oxide. The loss of crystallographic orientation in oxide films on lattice matched substrates derived from prehydrolyzed solution precursors may be caused by competition between nucleation sites within the film, that will produce randomly oriented crystallites, and heterogeneous nucleation sites on the substrate surface.

A similar competition between heterogeneous nucleation sites within a chemically derived intermediate film and sites on the substrate surface was observed in the growth of SrTiO_3 films on (100) SrTiO_3 single crystals by metalorganic decomposition.⁷⁰ In this case, the nucleation sites within the film were apparently crystallites of a carbonaceous intermediate compound that the authors tentatively identified as $\text{Sr}_2\text{Ti}_2\text{O}_5\text{CO}_3$. Thermal decomposition of this phase and growth of the SrTiO_3 occurred simultaneously at temperatures in excess of 600°C. Films annealed at 650°C for 30 min were randomly oriented polycrystalline SrTiO_3 . These films could be transformed to homoepitaxial SrTiO_3 by heat treating at much higher temperatures. Annealing at 1050°C for 30 min resulted in the formation of an epitaxial SrTiO_3 layer near the substrate surface, with an overlying layer of polycrystalline SrTiO_3 . Annealing for 30 min at 1100°C was required to completely transform the 150 nm thick polycrystalline films to homoepitaxial SrTiO_3 .

These observations are consistent with an epitaxial grain growth (EGG) mechanism.⁷¹ Epitaxial grain growth is commonly observed during high temperature annealing of polycrystalline Si films deposited on Si single crystals.⁷² Minimization of film/substrate interfacial energy provides the driving force for growth of grains that are lattice matched to substrate at the expense of those that are not. Significant epitaxial grain growth in oxide systems is typically observed only at relatively high temperatures^{70,73} (ie. > 1000°C in SrTiO₃ and ZrO₂).

Braunstein and coworkers⁷⁰ found epitaxial films could be grown directly from the weakly crystalline, carbon-containing intermediate material by heat treating the SrTiO₃ single crystal substrates prior to deposition of the MOD precursors. Atomic force microscopy indicated annealing the substrates at 1100°C in air for 1 h resulted in the development of surface steps with heights that were multiples of the lattice parameter of SrTiO₃. These steps appeared to act as effective sites for heterogeneous nucleation of epitaxial SrTiO₃ crystallites. Growth of homoepitaxial SrTiO₃ with good crystalline quality was achieved by annealing the chemically derived films at 650°C for 1 h on the heat treated substrates. No evidence of nucleation and growth of randomly oriented SrTiO₃ grains was observed by electron microscopy or Rutherford backscattering spectroscopy. The epitaxial growth of these MOD-derived oxide films appears to be similar, in some respects, to solid phase epitaxial (SPE) growth⁷⁴ of silicon from amorphous Si films on single crystal Si substrates. Silicon SPE is frequently inhibited by the presence of a native oxide coating at the single crystal Si/amorphous Si interface, which can result in epitaxial growth by a columnar mechanism.⁷² Growth of these homoepitaxial SrTiO₃ films is expected to occur by a layer-by-layer mechanism in the absence of an interfacial impurity.

Nashimoto and coworkers⁷⁵ also demonstrated a transformation from a carbon-containing intermediate film to an epitaxial oxide film in the synthesis of LiNbO₃ thin films on (0001) sapphire from non-prehydrolyzed alkoxides. Earlier studies of this sol-gel synthesis approach^{63,76} suggested thermal decomposition of the as-deposited films led to

the formation of a carbonate or oxocarbonate phase below 300°C. Transformation to the LiNbO_3 was immediately preceded by the decomposition of this carbonaceous intermediate at approximately 400°C. Results of TEM characterization of a film annealed for 1 h at 400°C in humid oxygen indicated nucleation of epitaxial LiNbO_3 occurred at the substrate surface, followed by growth into the overlying intermediate material. The observation of small, faceted pores enclosed in the epitaxial film, suggested that film growth occurred rapidly. The crystallization front appeared to have swept through the intermediate film quickly, trapping pre-existing porosity. The significant porosity that is likely present in the amorphous material from which the LiNbO_3 grows⁴⁶ may have encouraged the formation of crystallographic defects such as dislocations and subgrain boundaries separating film regions with slight mutual misorientations. Alternatively, much of the enclosed porosity found in the sol-gel derived films annealed at 400°C may have resulted from the local volume change as the crystallization front swept through the film. The observed microstructures do not suggest the films form by columnar growth. A solid phase epitaxial nucleation and growth mechanism may be at work in this system; however, the large misfit between the (0001) LiNbO_3 and sapphire (8.1%) may preclude layer-by-layer growth of the epitaxial film.

The examples described above illustrate that epitaxy is possible in oxide thin films derived from metalorganic solution precursors. Growth of heteroepitaxial films from chemically derived intermediates can occur by at least two different mechanisms: 1) epitaxial grain growth, requiring high temperatures and extended annealing times to convert a polycrystalline oxide film to an epitaxial one; 2) a solid phase mechanism in which epitaxial films nucleate and grow at relatively low temperatures into an amorphous or weakly crystalline intermediate film. The observations presented in Chapters 3 and 4 of this thesis indicate that neither of these mechanisms is consistent with the epitaxial growth of BYC thin films derived from metal trifluoroacetate precursor solutions.

Transient Phase Decomposition Kinetics

An important characteristic of microstructural evolution in chemically derived oxide thin films is that the desired materials grow through decomposition and reaction of intermediate phases. The process of elimination of the intermediates has a strong effect on the final microstructure and properties of the films. This is evident from attempts to synthesize BYC films from metalorganic precursors. One reason for the success of the TFA process is that it produces BaF_2 as an intermediate compound instead BaCO_3 . The fluoride-containing intermediate film is then reacted with water vapor at high temperature to form crystalline oxides. Carbonate and oxocarbonate intermediates are also present during metalorganic decomposition synthesis of BaTiO_3 , but they apparently do not persist in the films to high temperatures and degrade film properties to the same extent as in BYC.^{77, 78}

Similar to Nashimoto's studies of sol-gel derived LiNbO_3 ^{63, 75}, recent work by Endo⁶⁶ on KNbO_3 thin films indicated the importance of intermediate phase decomposition in microstructural evolution of chemically derived films. Potassium niobate is a perovskite-type oxide with a 4.7% a-axis lattice mismatch relative to MgO, which has the NaCl structure. Alkoxide precursor films were spin coated onto (100) MgO substrates and annealed at temperatures between 400°C and 800°C for a total of 1 h in humid (30 min) and dry (30 min) oxygen atmospheres. The onset of crystallization of the KNbO_3 was observed at an annealing temperature of 600°C. Below this temperature, the films were believed to consist of a mixture of X-ray amorphous carbonates and hydroxides. Highly crystalline KNbO_3 thin films with (100) preferred orientation were grown on MgO(100) from the non-prehydrolyzed precursor films at annealing temperatures greater than 700°C. These films, although of similar nominal thickness, were substantially rougher than the epitaxial LiNbO_3 films grown at 400°C on sapphire by Nashimoto. The KNbO_3 film consisted of elongated grains with grain boundaries near the film/substrate interface and poor grain-grain connectivity. The roughness of the film was found to increase as the annealing temperature was raised

above 700°C and as hold time at a given annealing temperature was increased.

The stability of K_2CO_3 is the probable reason that crystallization of alkoxide derived $KNbO_3$ was not observed by Endo in films heated at temperatures below 600°C. The rough morphology of the films may have been a consequence of the high heat treatment temperature required to decompose the carbonate and crystallize $KNbO_3$. The fact that extended annealing caused the film morphology to roughen suggests the niobate film did not form a stable coating on (100) MgO due to strain caused by epitaxial misfit or to interfacial energy effects. Processing the films at the high temperatures required for carbonate decomposition tended to exacerbate the film roughness and discontinuity. The microstructures of the $KNbO_3$ films were markedly different from those of the $LiNbO_3$ films prepared by Nashimoto et al.^{63, 75, 76} using a similar sol-gel method. These observations suggest that a major reason for the successful heteroepitaxial growth of $LiNbO_3$ was the ease of decomposition of the carbon-containing intermediate of the sol-gel derived $LiNbO_3$.

Film Structural Defects

The volume changes that chemically derived films undergo during solvent evaporation, precursor decomposition/gel condensation, intermediate compound decomposition, and final crystallization can result in the formation of various kinds of structural defects. Cracks, ruptures, and blisters are common larger-scale defects that can occur due to constrained film shrinkage, capillary pressure during gel drying, and uncontrolled evolution of gaseous decomposition products following deposition.^{39, 42, 44} These problems can be avoided by limiting the film thickness and modifying the low temperature segments of the post-deposition heat treatment. Slowing the furnace heating rate through the temperature range of greatest weight loss (as determined by TGA) has been observed to eliminate blister formation in sol-gel derived $KNbO_3$ ⁶⁶ and TFA-derived BYC thin films.⁴²

Porosity may be present in chemically derived oxide films due to the volume change on decomposition of intermediate compounds, or due to porosity already present in the intermediate films. These mechanisms may account for the the closed nano-sized pores observed by Nashimoto in sol-gel derived LiNbO_3 films annealed at 400°C .⁷⁵ The pores may have been remanent porosity from the intermediate film that were trapped by the LiNbO_3 growth front, or they may have formed due to local volume changes as the growth front advanced. The relatively large pin holes surrounded by dense LiNbO_3 observed in thin films heated to 700°C indicate the nano-sized pores present at 400°C coalesced on further heating.

Summary

Recent detailed studies of several technologically significant oxide systems indicate that microstructural evolution in chemically derived thin films is strongly dependent on the nature of the underlying substrate, the growth heat treatment conditions, and the intermediate phase decomposition kinetics. Growth of epitaxial oxide films on lattice matched substrates has been reported in several systems. Epitaxial growth was found to occur in homoepitaxial SrTiO_3 films prepared by metalorganic decomposition by either an epitaxial grain growth mechanism at high temperatures, or by an SPE-like mechanism at low temperatures, depending upon the availability of effective nucleation sites on the substrate surface. Heteroepitaxial growth of LiNbO_3 films deposited on (0001) sapphire by a sol-gel technique was ascribed to a solid phase epitaxial nucleation and growth mechanism. The exact nature of the nucleation and growth in chemically derived oxide films is often difficult to establish with certainty because the films typically form through the chemical reaction of intermediate compounds. The phase development process during post-deposition annealing must be controlled so as to avoid morphological defects in the final films. Formation of porosity may, however, be unavoidable in many cases due to the volume change associated with transformation of the intermediate phase(s) to the final crystalline oxide.

CHAPTER 3

EFFECTS OF FILM GROWTH CONDITIONS ON PROPERTIES AND MORPHOLOGY

3.1 INTRODUCTION

An important technological goal of this project was to develop a *reproducible* process for synthesizing high- J_c BYC thin films from metalorganic solution precursors. Preliminary results⁹ indicated TFA-derived heteroepitaxial films annealed at $\sim 800^\circ\text{C}$ in atmospheres with subatmospheric oxygen partial pressure could support critical current densities in excess of 10^6 A/cm^2 at 77 K. Further work was required, however, to improve the reproducibility of the process and identify the film growth conditions that produced optimal superconducting properties and microstructure. Investigating the "processing window" for preparing BYC films with good properties and structure was also expected to yield information about the nature of the nucleation and growth process and microstructure/property relations in films made by this MOD technique. In this chapter, a description is given of the experimental procedure developed to reproducibly synthesize BYC thin films with excellent superconducting properties from TFA precursors. The effects of annealing temperature, annealing time, and oxygen partial pressure on BYC epitaxial quality and superconducting transport properties are also discussed. Particular attention is given to the occurrence of microstructural defects such as 90° -misoriented grains and pores as a function of high temperature annealing conditions and film thickness. The results are compared to those reported for BYC films produced by *ex situ* coevaporation of BaF_2 , Y, and Cu and implications for BYC nucleation and growth

mechanisms are discussed.

Factors that contribute to the final microstructure of these chemically derived films include those affecting the structure and chemistry of the intermediate film produced by thermal decomposition of the TFA precursor, and the heat treatment conditions used to convert the intermediate films to BYC. Chemical and structural inhomogeneities in the intermediate films are expected to influence the nucleation and growth of the BYC oxide, which may be limited by diffusional processes during the high temperature heat treatment. Preliminary work indicated that the maximum annealing temperature and the partial pressure of oxygen in the furnace during annealing strongly affect microstructure development. In this early work, preferential growth of c-axis normal BYC was observed in TFA-derived films on (001) SrTiO_3 annealed in a humid, low $\text{P}(\text{O}_2)$ environment at relatively low temperatures (ie. below 800°C).⁹ Feenstra et al.⁷⁹ have studied the effects of post-deposition annealing temperature and $\text{P}(\text{O}_2)$ on the microstructure development and electrical properties of coevaporated BYC thin films on SrTiO_3 which contained BaF_2 , and have also reported improvements in film quality by firing in reduced $\text{P}(\text{O}_2)$ atmospheres. They suggested that the epitaxial quality and smooth morphology of their films resulted from improved BYC growth kinetics due to the enhanced oxygen vacancy concentration and associated lattice instabilities that may promote cation diffusion.

3.2 EXPERIMENTAL PROCEDURE

A metal trifluoroacetate solution precursor for BYC was prepared by dissolving the acetates of barium, yttrium, and copper in the 2:1:3 cation ratio in de-ionized water with a stoichiometric quantity of trifluoroacetic acid at room temperature. The resulting aqueous solution was dried overnight in air to yield a glassy blue residue. The residue was dissolved in sufficient methyl alcohol to give a solution with a copper ion concentration of ~ 0.75 M. This stock solution was subsequently diluted with addition methyl alcohol to adjust the final thickness of the films. The TFA precursor solution was

deposited onto approximately square (6.26 mm x 6.26 mm) (001)-oriented LaAlO_3 single crystal substrates by spin coating with a photoresist spinner. Circular LaAlO_3 wafers (50 mm diameter) were purchased from a commercial vendor⁸⁰ and diced into the smaller square substrates using a wire saw with a diamond-impregnated wire blade. Substrates were cleaned in successive ultrasonic baths of chloroform, acetone, and methyl alcohol with cleaning cycles typically lasting 15-20 minutes. The substrates were transferred quickly from solvent to solvent in order to prevent deposits from forming on the surfaces due to drying. Immediately prior to coating with the TFA precursor solution, the substrates were wiped with methanol and examined under an optical microscope at approximately 40X magnification. A spinning rate in the range of 2000-4000 rpm and an acceleration time of 0.4 s were used in depositing the precursor films. Spin-on deposition of a single coating of the TFA precursor solution with 0.4 M Cu ion concentration at 4000 rpm was found to result in a final BYC film thickness of 70-80 nm. The spin coater was started as soon as possible after applying enough precursor to cover the substrate. The samples were spun for 2 min. Spin coating was performed at ambient temperatures in the range 23-31°C and relative humidities in the range 5-40%. The photoresist spinner was located in a containment hood to avoid contamination of the samples by airborne dust and lint.

The samples were given two post-deposition heat treatments. In the first heat treatment, the precursors films were decomposed to an intermediate oxygen and fluorine-containing material by slowly heating to 400°C in a humid (20°C dew point) oxygen atmosphere (see Figure 3.1). Humid oxygen was injected into the furnace once the furnace temperature reached 100 to 120°C. The flow of humid oxygen was maintained until the furnace temperature reached 400°C, at which point the furnace power and the flow of gas in the furnace were shut off. The furnace was then allowed to cool with the samples in stagnant, humid oxygen. The room-temperature dew point oxygen flow was obtained by passing dry, ultrahigh purity oxygen through de-ionized water contained in three large (3 L) flasks in series, prior to entering the furnace. Measurements of the humidity of the exit gas showed that saturation required multiple sparged water reservoirs

in series. The water level in the flasks was maintained at approximately two-thirds full. Oxygen was injected into the flasks at a flow rate in the range of 2-4 L/min using gas dispersion tubes.

The intermediate films that resulted from decomposition of the metal trifluoroacetates were subsequently converted to $\text{Ba}_2\text{YCu}_3\text{O}_{7-x}$ by annealing in humid nitrogen/oxygen gas mixtures at temperatures greater than 700°C. Furnace atmospheres used for annealing the BYC thin films described in this report were saturated at either 20 or 65°C dew point. The heat treatment consisted of heating to the annealing temperature at a rate of 25°C/min, holding for various periods at that temperature, cooling at approximately 2.6°C/min to 525°C, and then furnace cooling (~1.7°C/min) to room temperature. Water vapor was introduced into the furnace by bubbling the incoming furnace gas through an attached reservoir of de-ionized water. The water reservoir consisted of a 2 L flask and a 500 ml flask connected in series. In the high dew point runs, the inlet gas was humidified to a dew point of 65°C by bubbling it through the larger flask in which the water was heated to approximately 80°C using a heating mantle, and then passing it through the smaller water-filled flask which was kept at 65°C by means of a constant temperature bath. In the 20°C dew point runs, the flasks were not heated.

Low $\text{P}(\text{O}_2)$ furnace atmospheres for the high temperature heat treatments were prepared using mass flow controllers to mix ultrahigh purity nitrogen with analyzed oxygen/nitrogen gas mixtures. The total flow rate of gas through the furnace was kept in the range 2.20-3.0 L/min. The oxygen partial pressure in the furnace was altered by changing the relative flow rates of the nitrogen and the oxygen/nitrogen mixture. The uncertainty in flow rates of the individual gases prior to mixing is estimated to be ± 0.05 L/min. The oxygen partial pressure of the furnace atmosphere was confirmed by measurements with a zirconia oxygen sensor in several of the runs. The heating profile for the 65°C dew point high temperature anneal is presented in Figure 3.2. During this heat treatment, the dry low $\text{P}(\text{O}_2)$ mixture was passed over the samples as the furnace

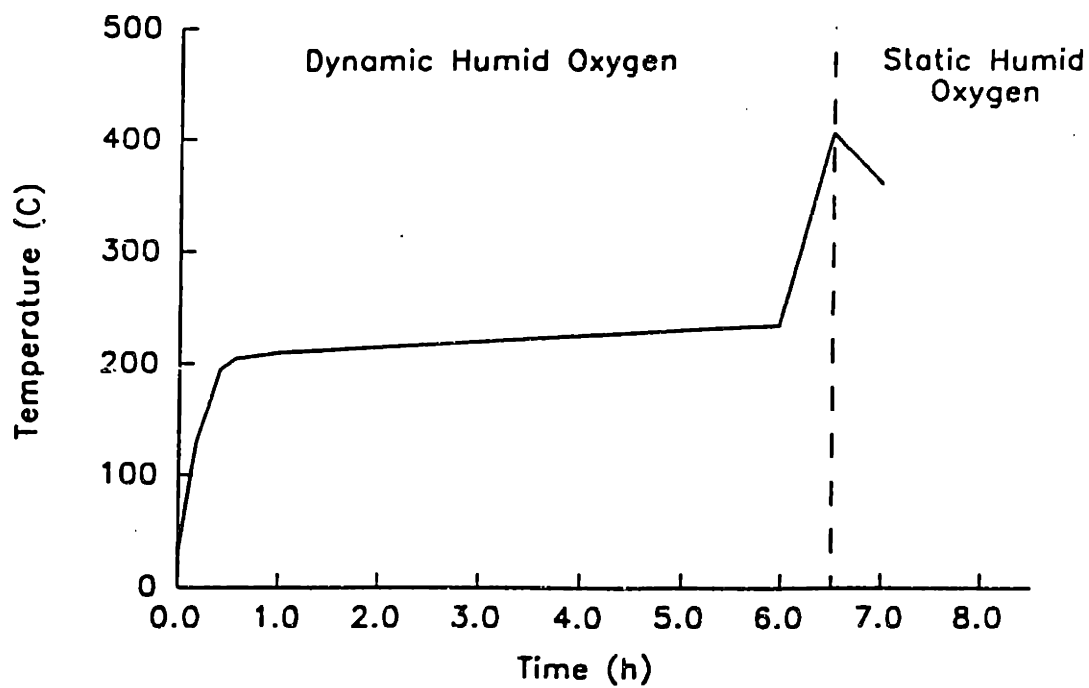


Figure 3.1 Heating profile for the low temperature heat treatment.

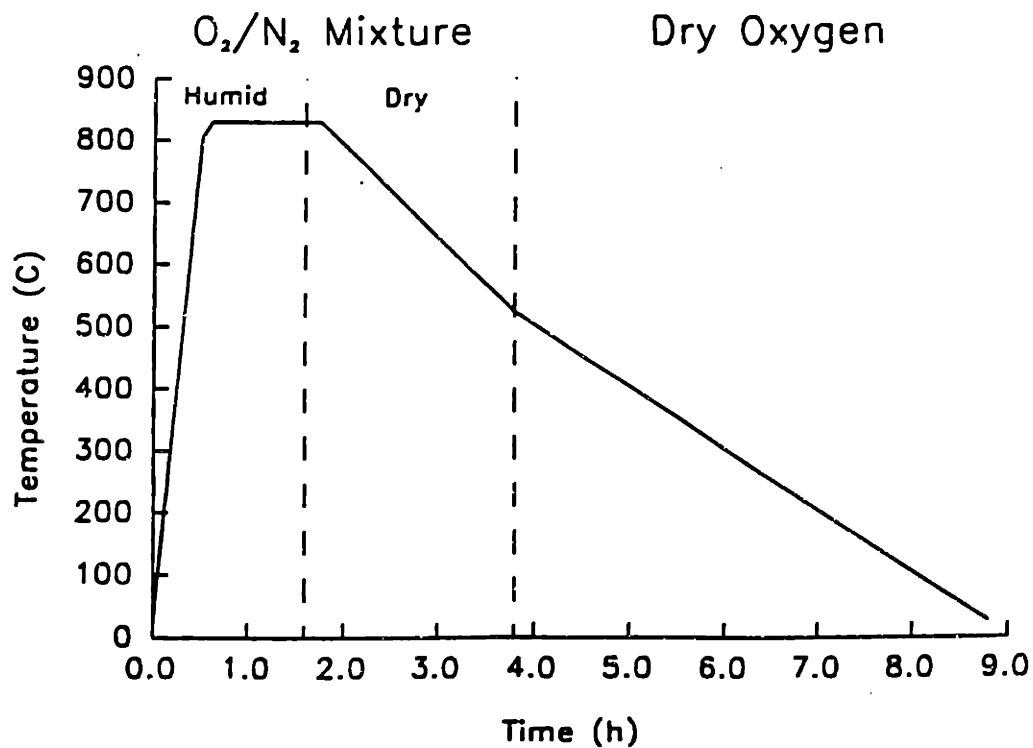


Figure 3.2 Heating profile for the high temperature (BYC growth and oxygenation) heat treatment.

(heating element) temperature increased from room temperature to 400°C. This initial dry purge avoided condensation of moisture inside the furnace near the samples (due to the temperature difference between the heating elements and the inside of the quartz tube) that was observed when the high humidity gas was introduced during the early part of the heat treatment. At a furnace temperature of 400°C, the incoming gas was diverted through the water reservoir and the flow of humid gas into the furnace was initiated. The humid low $P(O_2)$ atmosphere was passed over the samples throughout the remainder of the ramp to the annealing temperature and throughout all but the last 10 min of the high temperature hold. With 10 min remaining in the high temperature anneal, flow of the dry gas mixture was resumed. Following this dry purge at the annealing temperature, the dry gas flow was maintained as the samples were cooled to 525°C. At 525°C, the flow of dry oxygen was initiated and the films were furnace-cooled in oxygen to room temperature. The high temperature anneals in 20°C dew point furnace atmospheres were similar to the heat treatment shown in Figure 3.2, except that humid gas flow was initiated at a furnace temperature of 100°C.

All heat treatments described in this thesis were carried out in quartz tubes heated in CM 2200 horizontal furnaces.⁸¹ During the high temperature anneal, the sample temperature was measured using a type-K thermocouple sealed inside a high-purity alumina protection tube that was mounted along the centerline of the furnace. The tip of the thermocouple was placed several millimeters downstream of the samples on the quartz setter plate that supported them. At annealing temperatures greater than 700°C, a discrepancy of approximately 20°C was observed between the temperature measured by the furnace thermocouple (located in the heating elements) and that measured by the sample thermocouple. All annealing temperatures reported herein were determined from the output of the sample thermocouple.

Phase development in the annealed samples was observed by X-ray powder diffraction with $Cu K_{\alpha}$ radiation. The microstructures of the BYC films were observed and characterized by scanning electron microscopy (SEM). The epitaxial quality of

several of the samples was characterized by Rutherford backscattering spectroscopy (RBS) in the ion channeling mode with 1.8 MeV $^4\text{He}^+$ ions. Ions were backscattered through 175° . Electrical properties were determined directly by four point dc current-voltage measurements. Prior to the high temperature anneal, the intermediate films were mechanically scribed to produce a region of reduced cross-section for transport J_c measurements of the final, superconducting films. Silver electrodes were deposited onto the fired films by evaporation in a vacuum chamber. Following deposition of the electrodes, the films were annealed at 450°C for 30 min in oxygen to improve the adhesion of the silver electrodes. Multiple filaments of 0.025 mm diameter aluminum wire were used to connect the vacuum-deposited silver electrodes to a chip carrier using an ultrasonic wire bonder. Copper leads were then soldered to the chip carrier, and the carrier (containing the sample) was connected to a thermometer probe that was gradually lowered into a dewar of liquid helium for T_c and J_c measurements. The critical current density data were calculated using average thicknesses measured from SEM cross-section images in the scribed regions of the films. It was assumed that the films were fully dense for the sake of these calculations, although significant porosity was often observed in micrographs of the fired films. The films were assumed to have become normal when the applied current caused a voltage drop of 10^{-7} V across the samples. For the dimensions of the scribed bridges used in this work, this J_c criterion is not substantially different from a 10^{-6} V/cm criterion.⁸²

3.3 OBSERVATIONS

The effects of furnace $P(\text{O}_2)$ and annealing temperature on the superconducting transport properties were investigated for a large number of TFA-derived BYC films. Figure 3.3 shows the variation in zero-field J_c (at 77K) with oxygen partial pressure used during the high-temperature annealing at 780°C for films of 200-250 nm thickness. The critical current density varied from approximately 8×10^5 A/cm² for an annealing atmosphere containing .032 atm oxygen to approximately 2.5×10^6 A/cm² for an atmosphere containing ~500 ppm of oxygen. The magnitude of the J_c 's and their

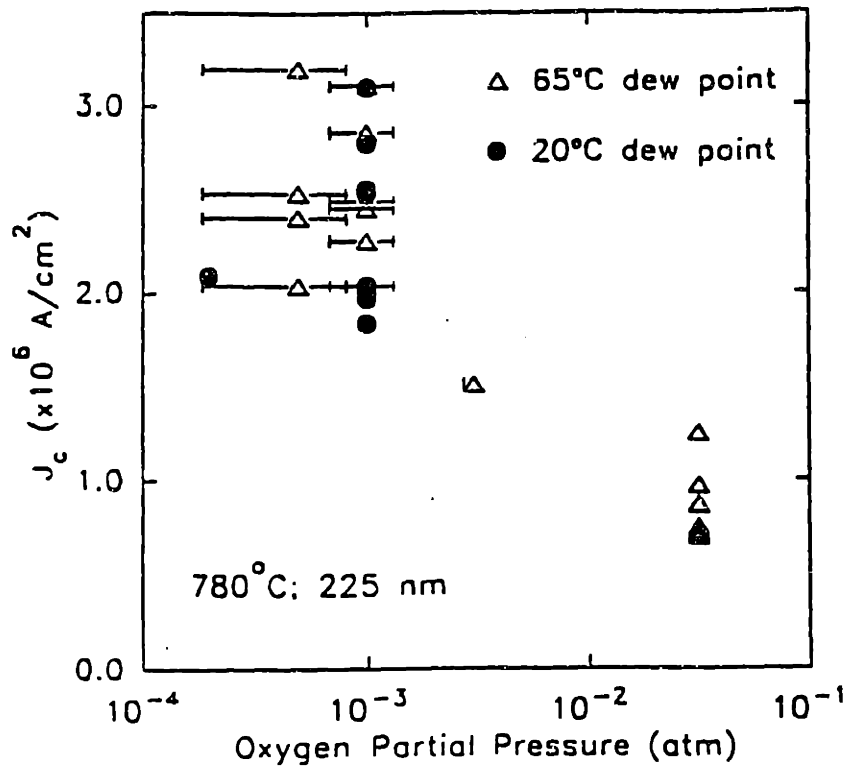


Figure 3.3 Effect of furnace oxygen partial pressure on J_c ($H_{app}=0$, $T=77$ K) of films of 200-250 nm thickness annealed at 780°C.

relationship with the annealing $P(O_2)$ did not appear to depend upon the dew point of the humidified furnace atmosphere. Furthermore, there was little change in the critical current density data between the two lowest $P(O_2)$ conditions (1000 ppm and 500 ppm). The other electrical properties of the films varied in a similar manner with decreasing furnace $P(O_2)$. Critical temperature transition widths decreased, and T_c 's and resistivity ratios increased as the oxygen partial pressure was lowered. The J_c , T_c , and resistivity ratios (ratio of the measured sample resistance at 300 K to that at 100 K) for samples annealed under several different $P(O_2)$ conditions are summarized in Table 3.1. Increasing the annealing temperature from 780°C to 830°C at a given oxygen partial pressure tended to increase the zero-resistance T_c somewhat, but had little effect on the magnitude of the J_c .

The X-ray diffraction powder patterns of films of ~220 nm thickness annealed at 780°C in 0.032 atm and 1×10^{-3} atm oxygen are shown in Figures 3.4a and 3.4b. The diffraction patterns of the epitaxial thin films prepared using this MOD technique did not change dramatically as a function of annealing $P(O_2)$ or temperature. It should be noted, however, that theta/two theta X-ray diffraction scans of BYC films on (001) $LaAlO_3$ are frequently unable to detect reflections from (*h*00) or (0*k*0) oriented BYC crystallites because of their coincidence with the (00*l*) substrate peaks. Therefore, the XRD measurements presented here do not provide information about the relative amounts of c-axis normal and c-axis in-plane orientation in these epitaxial films. Thin films produced under both $P(O_2)$ conditions in Figure 3.4 had very sharp and intense (00*l*) BYC reflections. The low intensity reflections detected in the 0.032 atm oxygen sample (Fig. 3.4a) between 25° and 30°, which cannot be assigned to $Ba_2YCu_3O_{7-x}$ or the substrate, were absent from the very low $P(O_2)$ pattern (Fig. 3.4b). Intense and narrow (00*l*) BYC peaks are also evident in the X-ray diffraction pattern of a film of 70-80 nm thickness annealed at 830°C in a 250 ppm oxygen atmosphere (Fig. 3.5a). Figure 3.5b is the theta rocking curve of the (005) reflection for the same film, with a FWHM of 0.4°.

Table 3.1: Superconducting properties of TFA-derived BYC thin films.

| Sample | d ¹ (nm) | P(O ₂) (ppm) | Dew Pt. (°C) | T _{anneal} (°C) | T _c (R=0) (K) | J _c (T=77 K) (MA/cm ²) | ρ ₃₀₀ /ρ ₁₀₀ |
|--------|------------------------|-----------------------------|-----------------|-----------------------------|-----------------------------|--|------------------------------------|
| NXS23 | 225 | 3.2x10 ⁴ | 65 | 780 | 90.8 | 0.9 | 2.90 |
| NXS28 | 225 | 3.2x10 ⁴ | 65 | 780 | 90.0 | 1.0 | 2.70 |
| NXS39 | 225 | 1000 | 65 | 780 | 92.3 | 2.5 | 3.30 |
| NXS40 | 225 | 1000 | 65 | 780 | 92.3 | 3.1 | 3.35 |
| NXS43 | 225 | 1000 | 65 | 780 | 92.0 | 2.0 | 3.15 |
| NXS46 | 225 | 500 | 65 | 780 | 91.6 | 2.0 | 3.25 |
| NXS47 | 225 | 500 | 65 | 780 | 91.3 | 3.2 | 3.45 |
| NXS62 | 225 | 1000 | 20 | 780 ² | 92.6 | 2.0 | 3.05 |
| NXS63 | 225 | 1000 | 20 | 780 ² | 92.4 | 2.6 | 3.20 |
| NXS68 | 150 | 1000 | 20 | 780 ² | 91.7 | 3.7 | 3.30 |
| NXS76 | 225 | 1000 | 20 | 780 ² | 93.5 | 2.8 | 3.30 |
| NXS78 | 225 | 250 | 20 | 830 | 93.8 | 3.2 | 3.55 |
| NXS79 | 225 | 250 | 20 | 830 | 93.2 | 2.8 | 3.50 |
| NXS80 | 70 | 250 | 20 | 830 | 93.7 | 5.8 | 3.25 |
| NXS81 | 70 | 1000 | 20 | 780 ² | 93.6 | 9.2 | 3.20 |
| NXS82 | 70 | 1000 | 20 | 830 | 93.4 | 4.6 | 3.40 |
| NXS85 | 70 | 250 | 20 | 830 | 93.6 | 5.1 | 3.50 |
| NXS89 | 70 | 250 | 20 | 830 | 93.0 | 6.5 | 3.40 |
| NXS96 | 70 | 250 | 20 | 830 | 92.4 | 6.2 | 3.75 |
| NXS104 | 500 | 250 | 20 | 830 | 93.3 | 1.2 | 3.80 |
| NXS111 | 225 | 250 | 20 | 830 | 93.6 | 2.3 | 3.60 |
| NXS112 | 70 | 250 | 20 | 720 | 92.7 | 3.3 | 3.10 |
| NXS114 | 350 | 250 | 20 | 830 | 92.2 | 1.1 | 3.80 |
| NXS115 | 350 | 250 | 20 | 780 | 93.6 | 1.0 | 3.70 |

Samples annealed for 70 min at T_{anneal} unless otherwise indicated.

¹ Nominal film thickness.

² Annealed for 100 min.

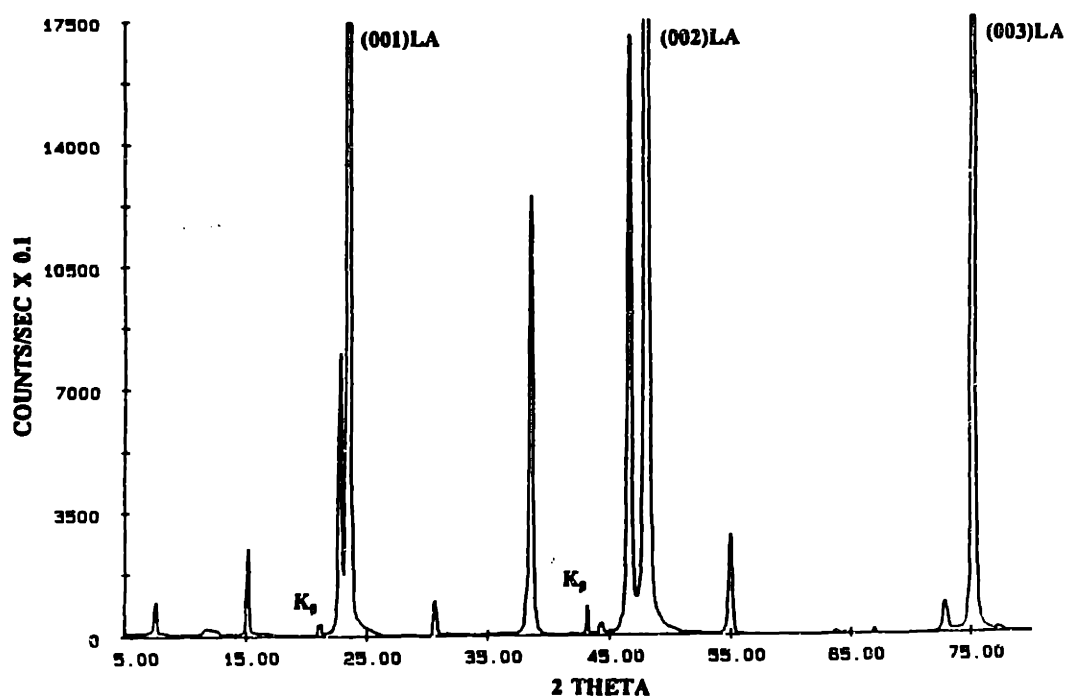
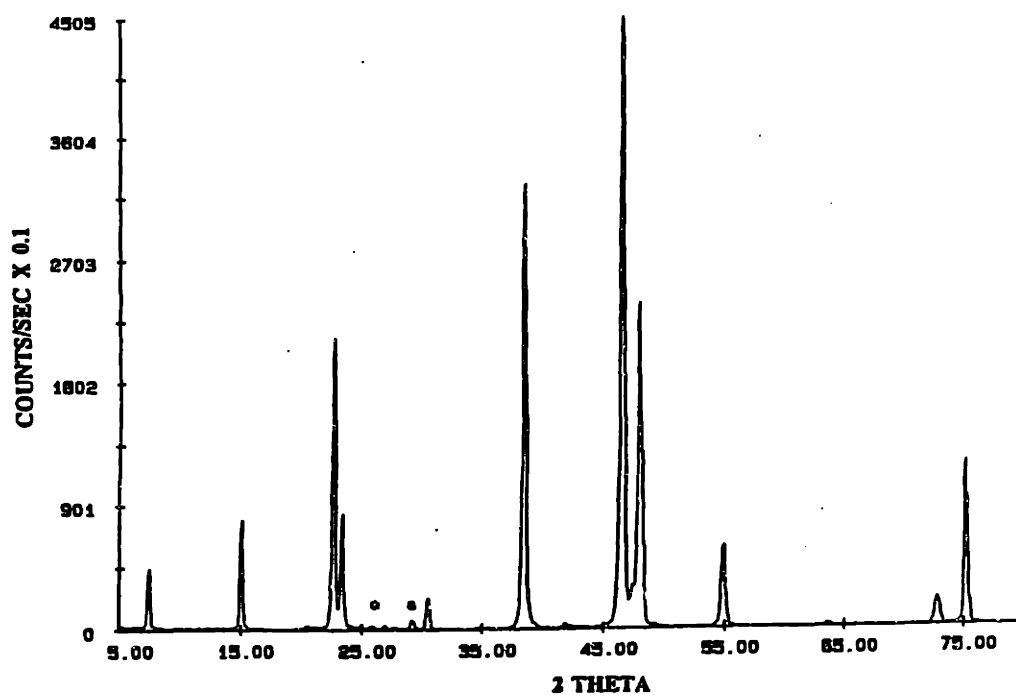


Figure 3.4 X-ray diffraction patterns (in the θ - 2θ configuration) for films of 200-250 nm thickness annealed at 780°C in a) 0.032 atm and b) 1000 ppm oxygen atmospheres (balance nitrogen). Unidentified reflections marked by asterisks.

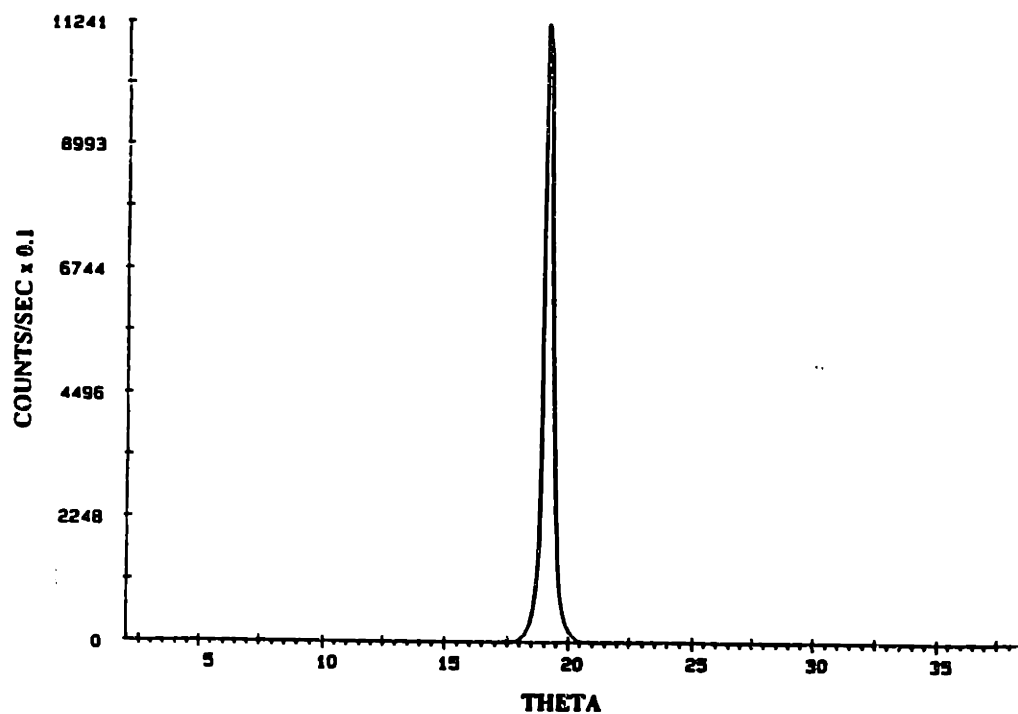
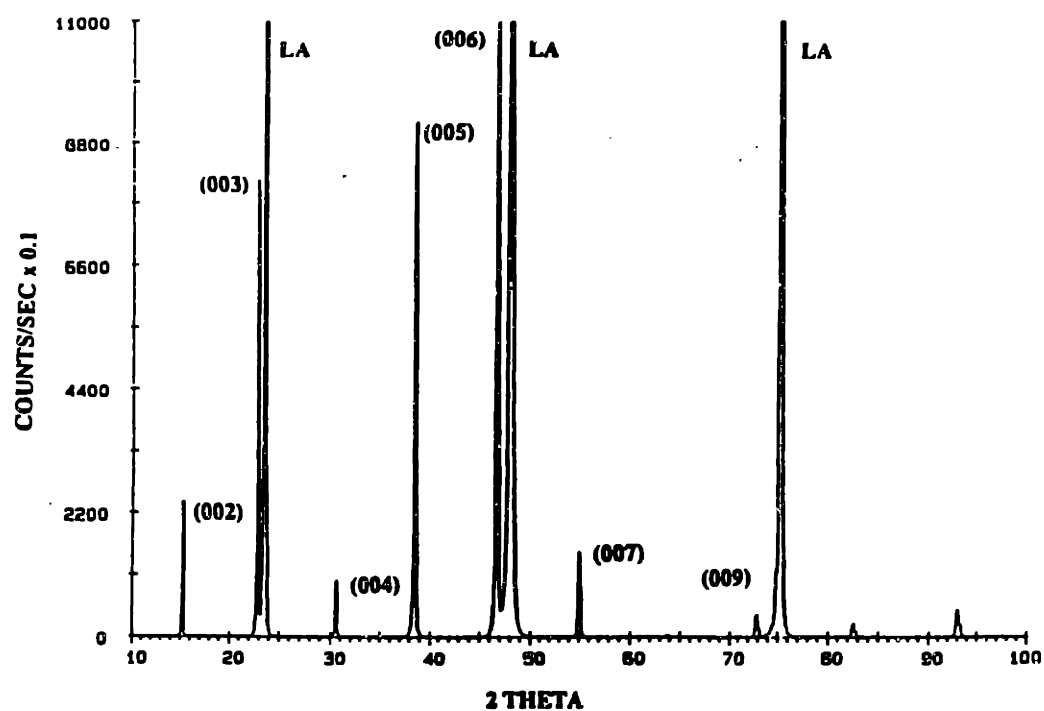


Figure 3.5 X-ray diffraction a) θ - 2θ scan with substrate peaks marked "LA" and b) θ rocking curve (of the (005) BYC reflection) of a TFA-derived film of 70-80 nm thickness annealed at 830°C in a 250 ppm oxygen atmosphere.

A stronger dependence on annealing oxygen partial pressure was observed in the RBS ion channeling spectra in Figure 3.6, measured from films of ~220 nm thickness annealed at 780°C. This technique, which measures the degree of crystalline order in the films, is sensitive to the presence of grain boundaries and is, therefore, better able to detect the presence of 90°-misoriented grains. The value of χ_{\min} , the ratio of the RBS yield behind the barium surface peak in the channeling spectrum to that yield in the random spectrum, decreased from 28% in a sample annealed in 0.032 atm of oxygen to 10% in a sample annealed in 500 ppm of oxygen.

The scanning electron micrographs in Figures 3.7 and 3.8 show the effect of the annealing $P(O_2)$ on the morphology of films of 200-250 nm nominal thickness. Commonly observed morphological features in films fired under all the $P(O_2)$ conditions examined in this study include pores; relatively large (~ 1 μm diameter) irregularly-shaped segregate regions (see Fig. 3.10a); small spherical particles (clearly visible in Figure 3.7c); and a granular mosaic pattern of orthogonal BYC platelets seen edge-on (see Fig. 3.7b and 3.7c). The second phase surface particles originate due to reaction with contaminants in the furnace environment during the high temperature anneal. Experiments undertaken to identify the particles and determine their origin are discussed in Chapter 5. The area fraction of the film occupied by pores is approximately the same in the three micrographs in Figure 3.7; however, the average pore size in Figures 3.7b and 3.7c is larger than that visible in Figure 3.7a. Also, finer scale surface roughness appeared to be present in the 0.032 atm oxygen sample than in the reduced $P(O_2)$ samples. The mosaic microstructure was observed frequently in the TFA-derived films. A clear pattern of BYC grains with c-axes in the film plane growing up out of the surrounding c-axis normal material is present in Figures 3.7b and 3.7c, but is not evident in the Fig. 3.7a. The density of these outgrowths tended to decrease as the furnace $P(O_2)$ was reduced from 3000 ppm to <1000 ppm at 780°C, as shown in the figure. The fractured cross-section SEM images in Figure 3.8 also suggest a reduction in the fine surface roughness of the films as the annealing $P(O_2)$ was decreased. The film grown in the 0.032 atm oxygen gas mixture (Fig. 3.8a) has a somewhat columnar appearance, while the relatively smooth, c-axis normal BYC

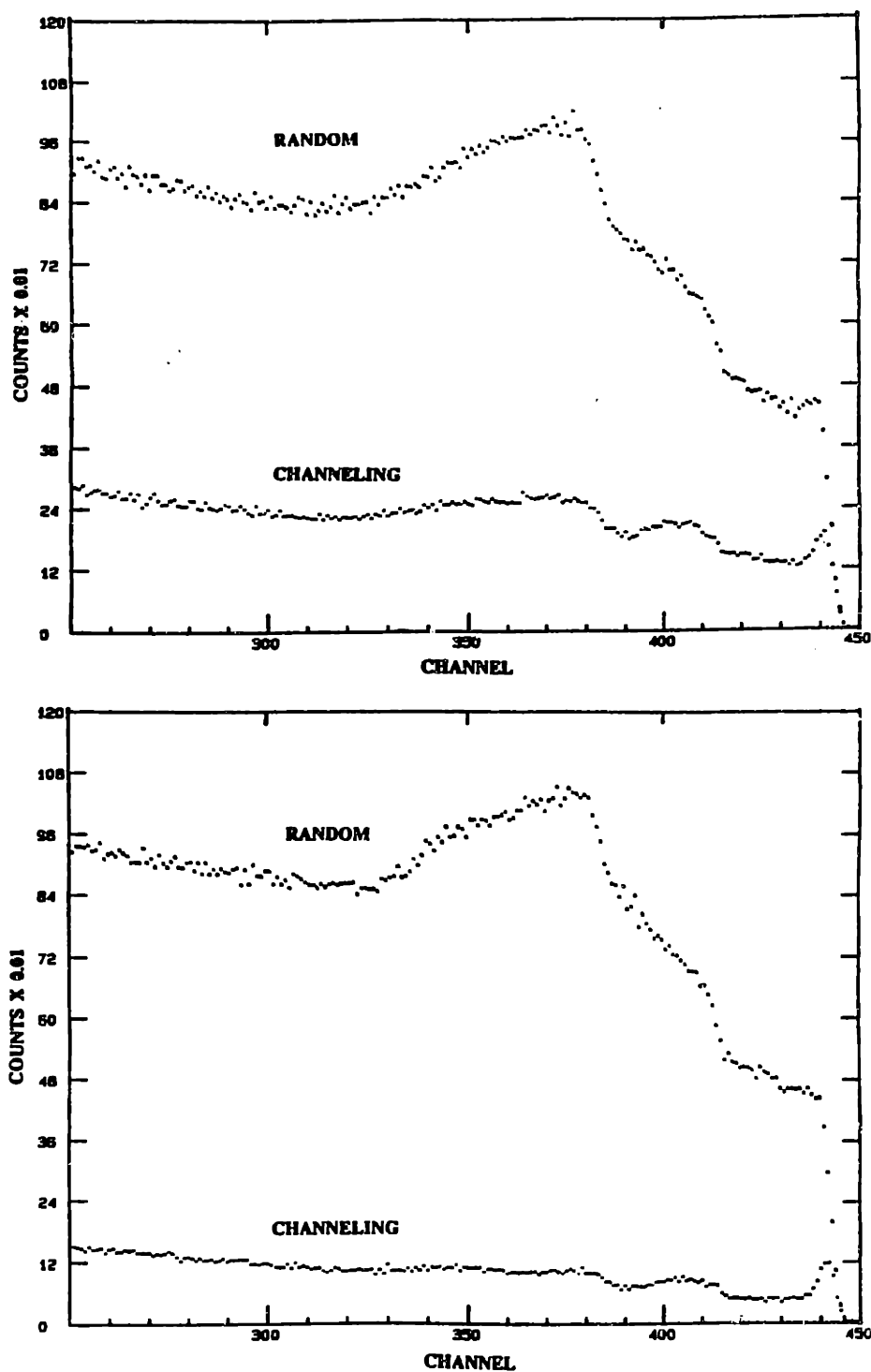


Figure 3.6 Rutherford backscattering spectra in random and channeling orientations of TFA-derived films of 200-250 nm thickness annealed at 780°C in a) 0.032 atm and b) 500 ppm oxygen atmospheres.

a)



b)

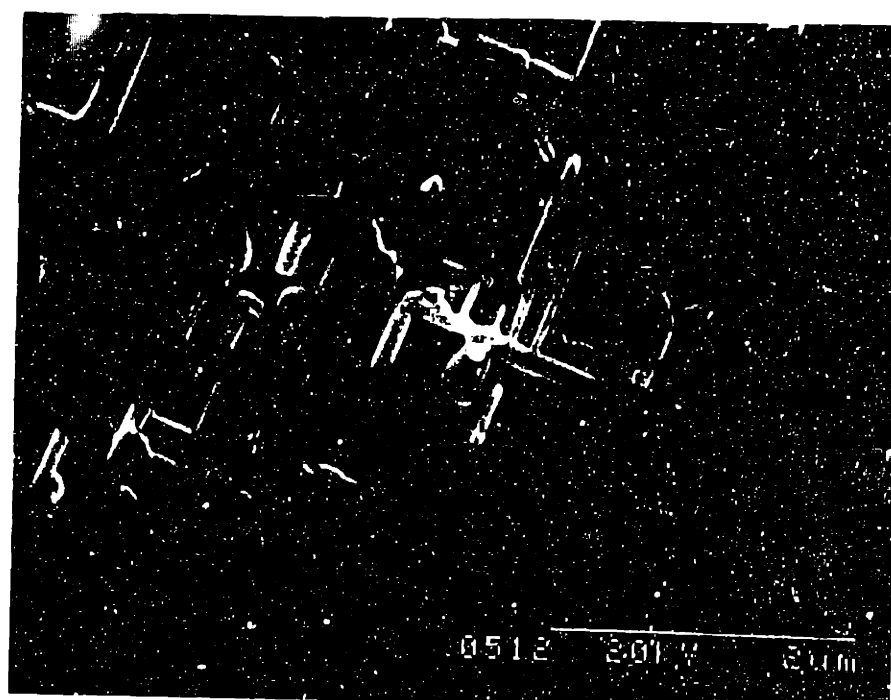


Figure 3.7 Plan view SEM micrographs of TFA-derived films of 200-250 nm thickness annealed at 780°C in a) 0.032 atm, b) 3000 ppm, and c) 500 ppm oxygen atmospheres (balance nitrogen).

c)

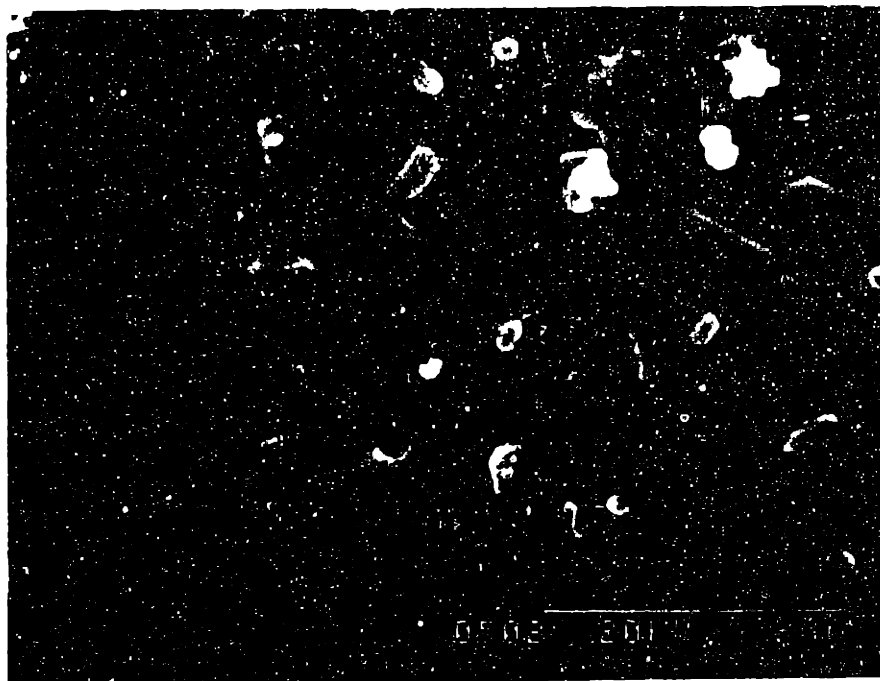


Figure 3.7 Continued.

grains are clearly apparent in the film annealed in a 1000 ppm oxygen atmosphere (Fig. 3.8b).

Superconducting transport measurements of MOD-derived films of varying thickness indicated the J_c ($H_{app}=0$, $T=77$ K) decreased as the film thickness increased. Results obtained from specimens annealed at temperatures from 780 to 830°C and $P(O_2)$'s from 250 to 1000 ppm are summarized in Figure 3.9. Data for the three sets of processing conditions represented in Figure 3.9 all appear to obey the same J_c versus thickness relationship. Changing the film thickness had a significant effect on the morphology of the BYC films as shown in the plan view SEM images in Figure 3.10. The samples in this figure were annealed at 830°C in 250 ppm oxygen. Films of 70-80 nm thickness (Fig. 3.10a) had the roughest morphology of the three thicknesses represented in the figure. The thin samples contain faceted pin holes (~40 per 100 μm^2 areal density), a few c_1 BYC outgrowths (~2-3 per 100 μm^2), and second phase the surface particles discussed above. Contrast variations in the c-axis normal BYC in Figure 3.10a suggest the film surface has a terraced structure. The roughness of films annealed under these conditions tended to decrease as the film thickness was increased. A significant reduction in the density of pin holes was probably the most obvious effect of increasing the film thickness. The areal density of pin holes was reduced to ~4 per 100 μm^2 in the sample in Figure 3.10c. However, the thicker films contain some deep depressions (marked by arrows in Fig. 3.10c) that appeared to result from densification of the pin holes. The areal density of c_1 outgrowths was approximately constant for all three film thicknesses shown in Figure 3.10; however, the c-axis in-plane grains were typically larger in the thicker films. The small hemispherical surface particles present on the surface of thinner films (see Figs. 3.10a and 3.10b) were absent from the 500 nm thick specimen and appeared to have coalesced into larger particles, many of which are in contact with c_1 outgrowths.

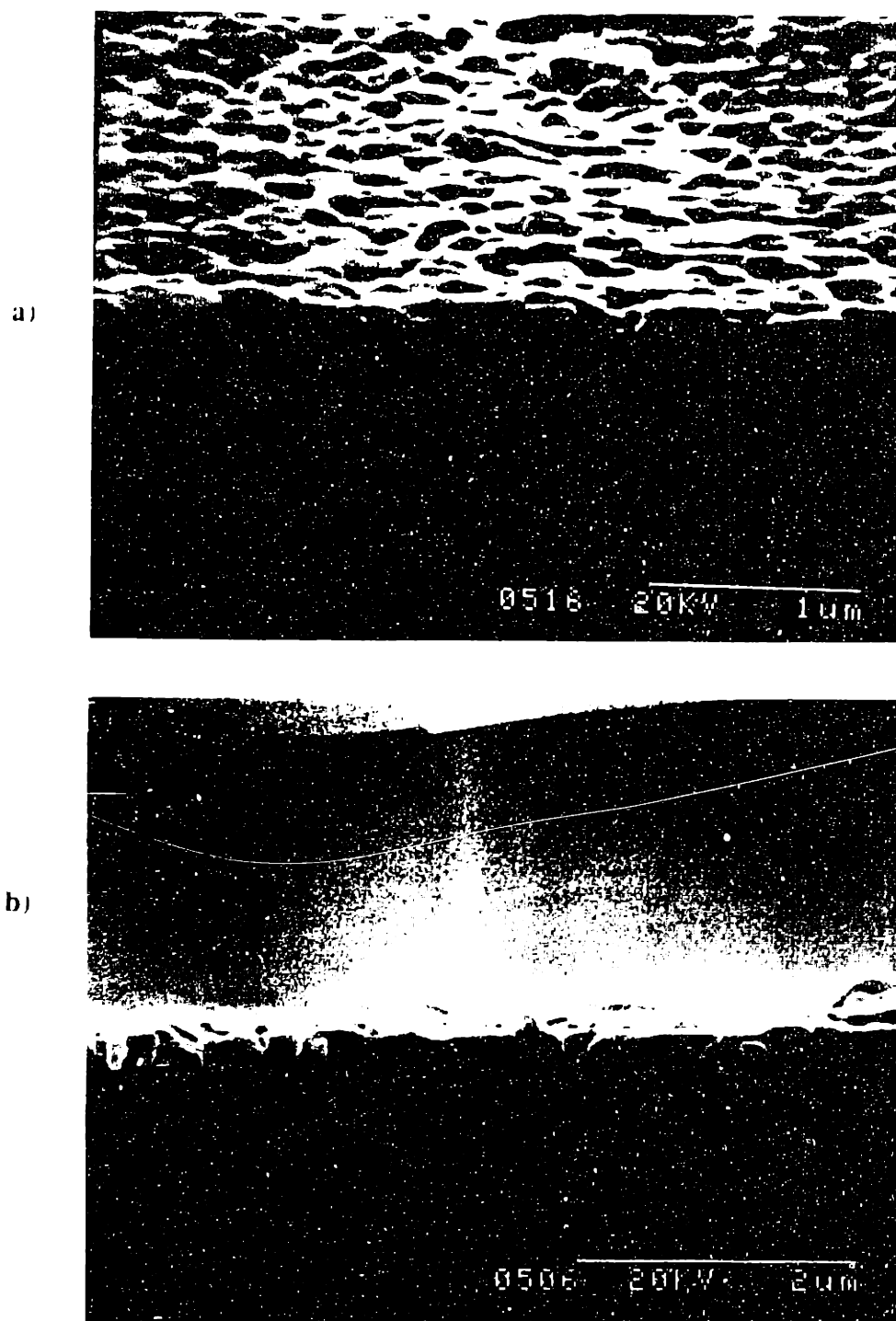


Figure 3.8 Fractured cross-section SEM images of the films shown in Fig. 3.7 annealed in a) 0.032 atm and b) 500 ppm oxygen atmospheres.

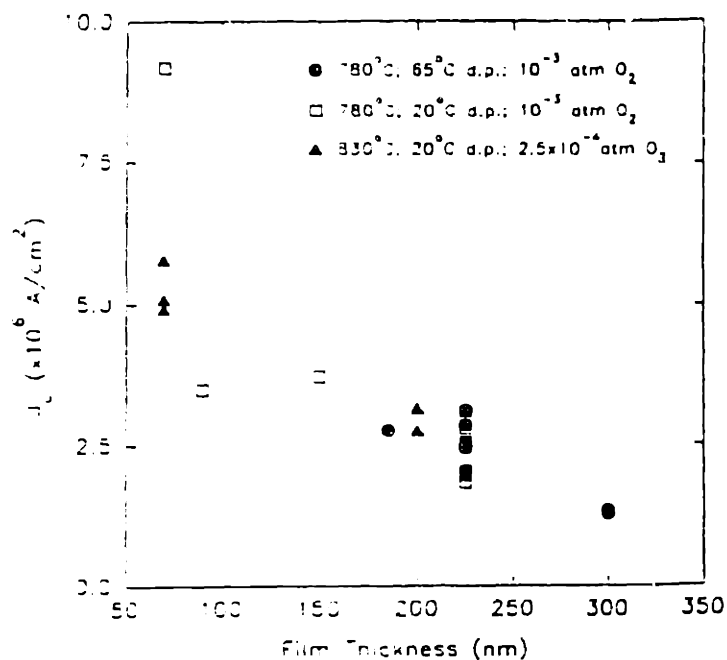


Figure 3.9 Variation in J_c ($H_{app}=0$, $T=77$ K) with film thickness for several sets of annealing conditions.

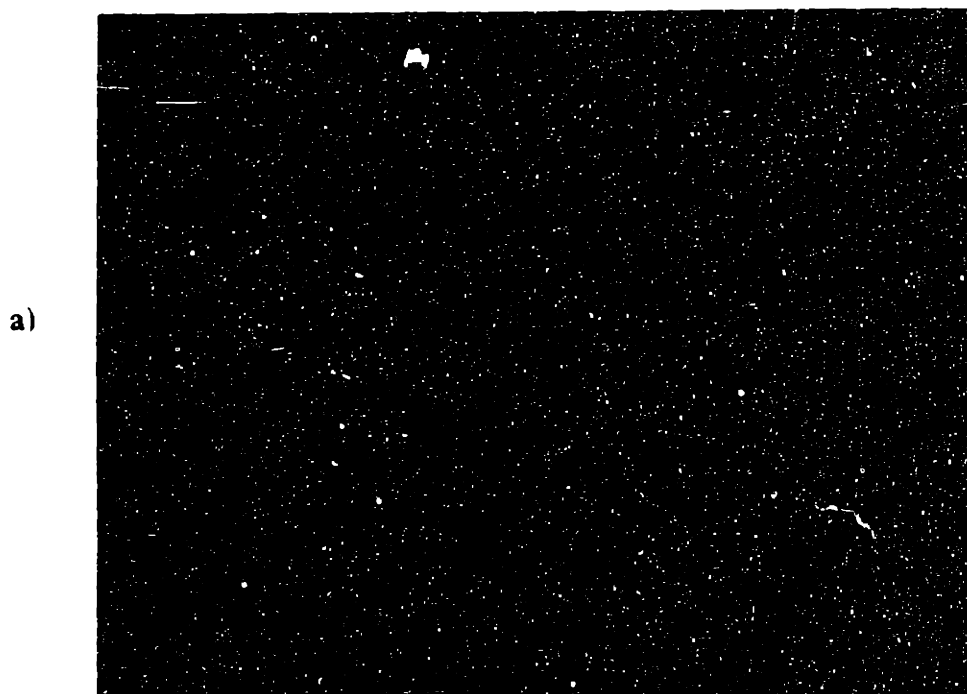
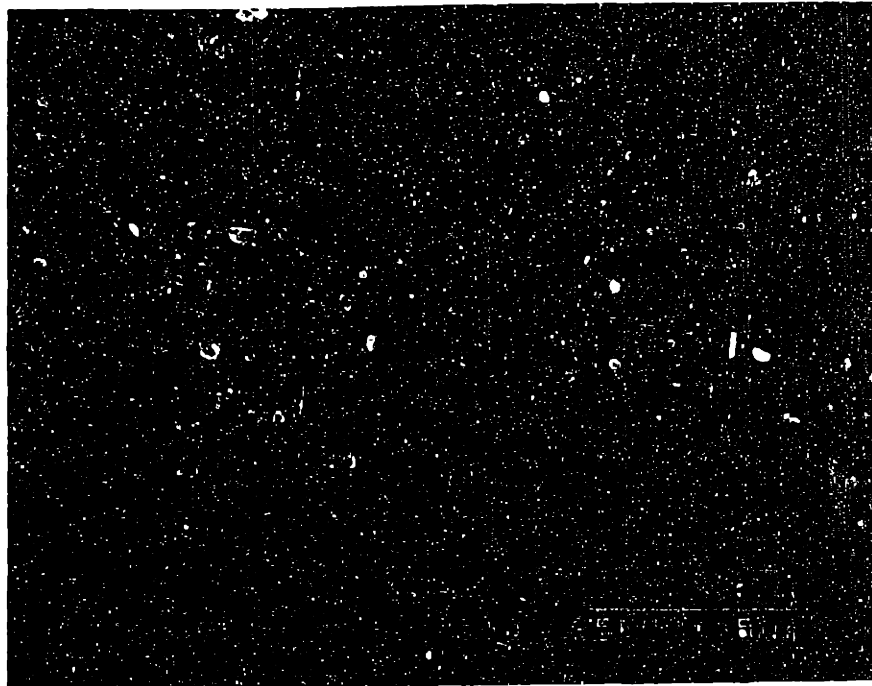


Figure 3.10a Plan view SEM micrographs of TFA-derived films of a) 70-80 nm thickness, b) 200-250 nm thickness, and c) ~ 500 nm thickness annealed at 830°C in a 250 ppm oxygen atmosphere.

b)



c)

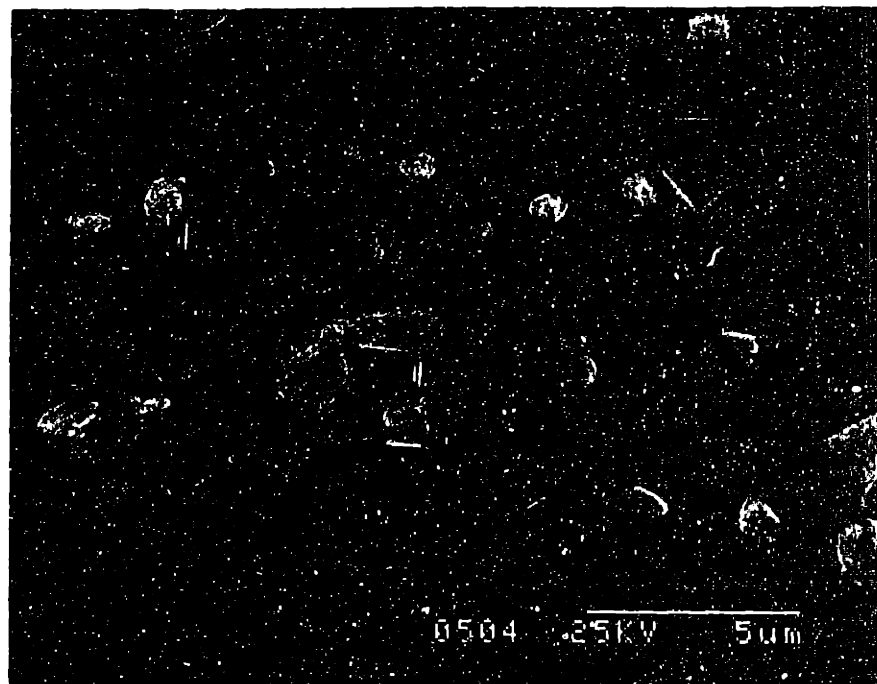


Figure 3.10 Continued.

The effect of the annealing temperature on film microstructure is evident in Figure 3.11 for BYC films of 350 nm nominal thickness annealed in a oxygen/nitrogen gas mixture containing 250 ppm oxygen. The c-axis normal BYC in the film annealed at 780°C (Fig. 3.11a) is much more porous than the samples annealed at 830°C (Fig. 3.11b, for example), and a rough island-like morphology is clearly evident. The areal density of 90°-misoriented outgrowths is also somewhat higher in the film annealed at the lower temperature (~5 per 100 μm^2). The superconducting properties (Table 3.1) were not greatly affected, however, by varying the annealing temperature between 780 and 830°C in 250 ppm oxygen furnace atmosphere. The $T_c(R=0)$ was greater than 93 K for the specimen in Figure 3.11a and the J_c ($H_{app}=0$, $T=77$ K) of 10^6 A/cm² was within the range of critical current densities typically observed in films of similar thickness annealed at 830°C. A plan view SEM micrograph of a TFA-derived film of 70-80 nm thickness annealed at 720°C in a 250 ppm oxygen atmosphere is presented in Figure 3.12a. Comparison with Figures 3.12b or 3.10a, micrographs from films of 70-80 nm thickness processed identically except for an annealing temperature of 830°C, indicates that reducing the annealing temperature to 720°C gave rise to a strong c-axis in-plane mosaic structure and increased porosity in the film. The size of the 90°-misoriented crystallites visible in Figure 3.12a is less than that of the outgrowths in the films annealed at higher temperature; however, they are substantially more numerous in the 720°C specimen (>500 per 100 μm^2). More of the finer-scale surface roughness observed on the 350 nm-thick film heat treated at 780°C (Fig. 3.11a) is also evident on the c-axis normal material in Figure 3.12a. At this low growth temperature (720°C), the superconducting properties of the film were somewhat degraded relative to those of the best specimens (see Table 3.1). The value of the critical current density at 77 K, $\sim 3 \times 10^6$ A/cm², was, however, still quite high.

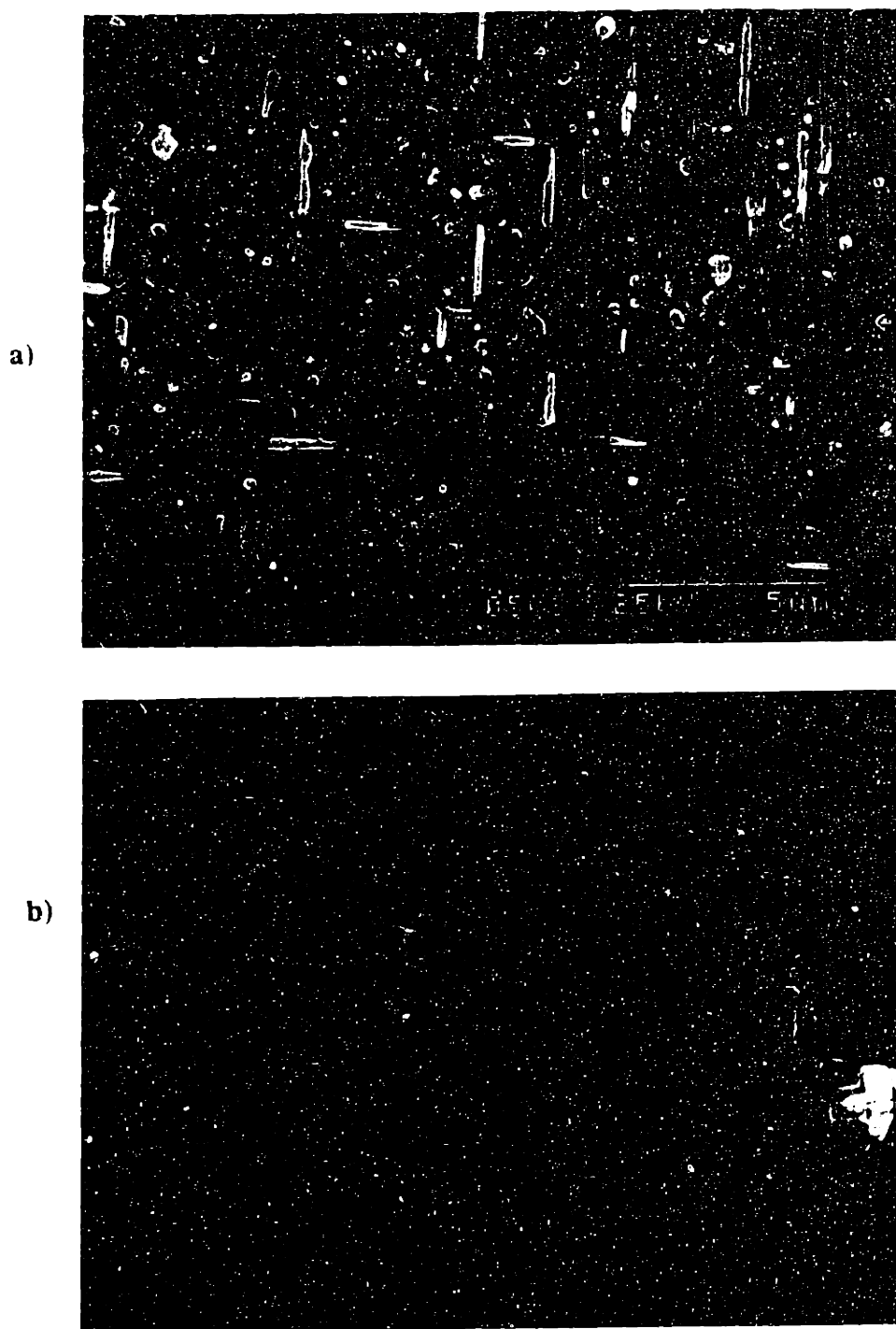
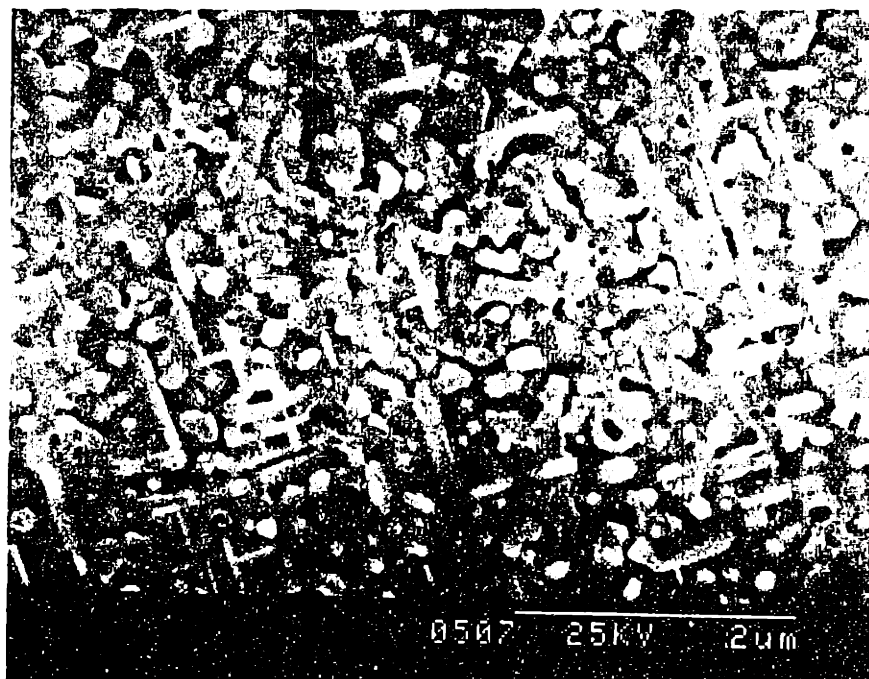


Figure 3.11 Scanning electron micrographs of films of ~ 350 nm thickness annealed in 250 ppm oxygen atmosphere at a) 780°C and b) 830°C .

a)



b)

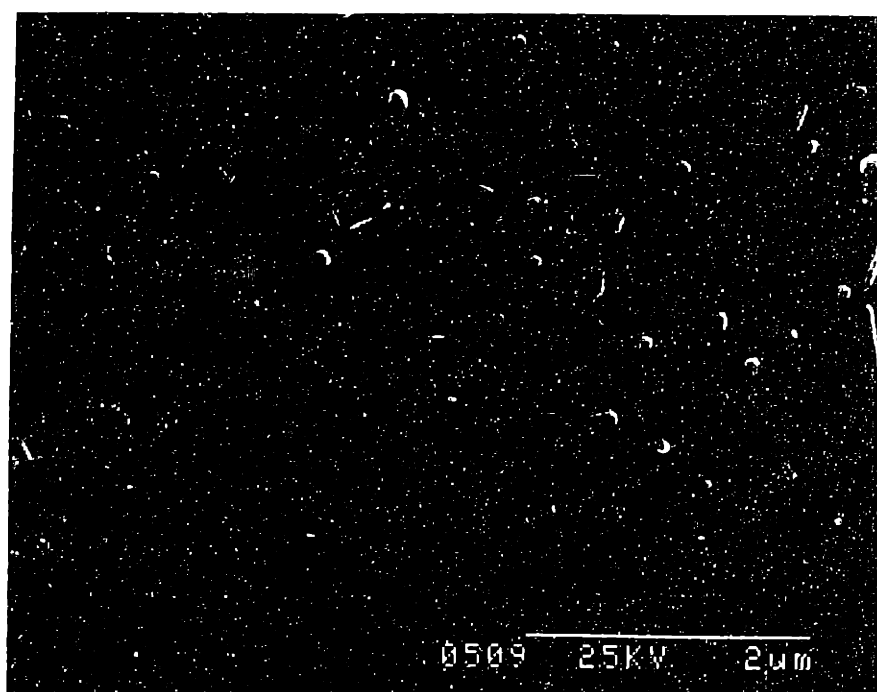


Figure 3.12 Chemically derived films of 70-80 nm thickness annealed in 250 ppm oxygen atmosphere at a) 720°C and b) 830°C.

3.4 DISCUSSION

3.4.1 Sample Preparation

The solution preparation technique outlined in the Section 3.2 is significantly different from the method developed initially⁹ which involved refluxing of metal carbonate powders in methanol and trifluoroacetic acid. It was found that the homogeneous reaction of the aqueous acetate solutions with TFA acid went to completion reproducibly, while small particles of unreacted powder often remained in the refluxed solutions made from carbonate starting materials. In addition to the difficulty of achieving complete reaction, there were several other factors which contributed to reproducibility problems when using the carbonate procedure. The availability of copper basic carbonate of reliable composition was problematic. It was difficult to obtain high purity $\text{Cu}_2(\text{OH})_2\text{CO}_3$ powder from commercial sources. It could not be readily synthesized in our laboratory due to the formation of poorly-defined mixed hydroxycarbonate species. Reaction of the metal carbonates with trifluoroacetic acid was heterogeneous and relatively slow, and required extended periods of reflux. Esterification of the methanol may have introduced a competing reaction for the TFA acid in this system, as esterification reactions are acid-catalysed and proceed most rapidly for unhindered alcohols.⁸³ The new precursor preparation avoids these problems by using well-characterized starting materials that are commercially available in high purity, and a stoichiometric acid exchange reaction that occurs quickly at room temperature in water. Methanol and trifluoroacetic acid are not present at the same time during the preparation; therefore, there are no competing reactions to form methyltrifluoroacetate. The metal TFA solutions prepared from acetate starting materials did not change in appearance and no systematic degradation in the properties of $\text{Ba}_2\text{YCu}_3\text{O}_{7-x}$ films prepared from the same batch of precursor was observed over the lifetime of the precursor solutions (greater than one year).

The low temperature heat treatment was developed to minimize damage to the film during thermal decomposition of the TFA precursor and to maintain the correct metal

stoichiometry in the films. Thermogravimetric analyses (TGA) of a dried TFA precursor powder indicate the as-deposited films lose more than 60% of their starting weight during heating to 400°C through evolution of solvent, water, and gaseous decomposition products.⁸⁴ The TGA trace from a powder sample heated in air (shown in Fig. 3.13) indicates most of the weight loss occurs between 240 and 280°C, during the decomposition of the metal TFA species. Heating in pure oxygen instead of air is known to reduce the decomposition temperatures of the metal TFA's.⁵⁸ Rapid evolution of gaseous products and the accompanying stress on the film material during precursor decomposition produces a variety of large-scale defects in the resulting intermediate films. These include ruptures, blisters, and complete delamination.⁴² The heating profile shown in Figure 3.1, as developed by Smith⁸⁵, includes a very slow ramp segment between 205 and 240°C. This slow ramp appears to allow gaseous species to diffuse out of the films slowly, instead of nucleating blisters and other defects. The heat treatment in Figure 3.1 has been found to reproducibly yield nearly blister-free intermediate films. A humidified atmosphere was used during the low temperature heat treatment to prevent volatilization of $\text{Cu}(\text{TFA})_2$, which was detected by infra-red spectrometry during heating of the precursor solution in dry atmospheres.⁹ Heating the as-deposited films in a humid atmosphere is believed to cause hydrolysis of $\text{Cu}(\text{TFA})_2$ to nonvolatile $\text{Cu}(\text{TFA})_2 \cdot n\text{H}_2\text{O}$.

3.4.2 Transport Properties and Morphology

The experimental results described in Section 3.3 agree qualitatively with those reported for *ex situ* films deposited by electron beam coevaporation of BaF_2 , Y, and Cu⁷⁹,^{87, 88}, in that the superconducting properties and microstructure of the films tended to improve as the annealing temperature/ $P(\text{O}_2)$ conditions approached those at which $\text{Ba}_2\text{YCu}_3\text{O}_{7-x}$ becomes unstable. Figure 3.14 summarizes the temperature and $P(\text{O}_2)$ conditions investigated in this study. The $\text{Ba}_2\text{YCu}_3\text{O}_{7-x}$ decomposition line proposed by Feenstra et al.⁷⁹ and consistent with the results of Ahn and coworkers⁸⁹ is included as the dashed line in the figure. The tetragonal form of BYC is stable at temperature/ $P(\text{O}_2)$ conditions above the line. Below the line, it decomposes to form BaY_2CuO_5 ,

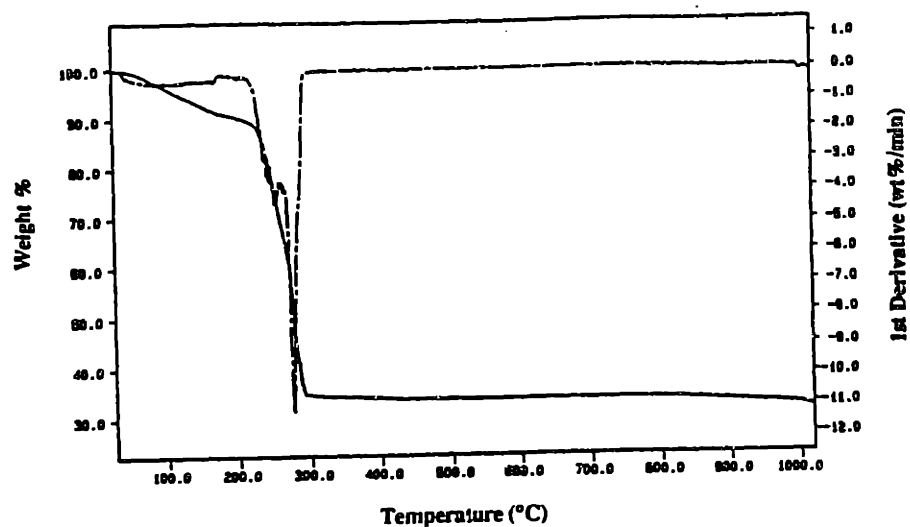


Figure 3.13 Thermogravimetric analysis (TGA) trace including 1st derivative for a dried powder sample of the mixed metal TFA precursor.

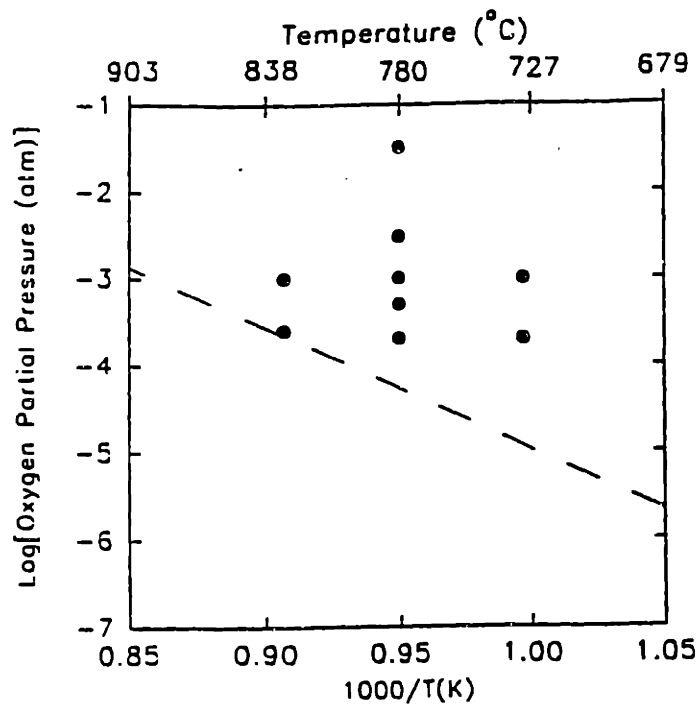


Figure 3.14 Van't Hoff plot of the annealing temperature and $P(O_2)$ conditions investigated in this chapter.

$\text{Ba}_3\text{YCu}_2\text{O}_{6+y}$, BaCu_2O_2 and molecular oxygen.⁹⁰ High- T_c and J_c TFA-derived films were produced in these studies by annealing under $P(\text{O}_2)$ and temperature conditions near the proposed decomposition line (1000 ppm/780°C and 250 ppm/830°C). A marked degradation in T_c and J_c was observed when annealing conditions further above the decomposition line in Figure 3.14 were used, as in the 0.032 atm/780°C samples.

The ion channeling results in Figure 3.6 correlate well with the electrical property data. The χ_{min} of 10% for the sample in Figure 3.6b (500 ppm/780°C) is relatively low and similar in magnitude to that of a sample annealed under similar conditions by Feenstra and coworkers.⁷⁹ The increase in χ_{min} to 28% in Figure 3.6a (0.032 atm/780°C) indicates a greater degree of crystallographic disorder in the sample annealed in a higher $P(\text{O}_2)$. Monte Carlo simulations predict a χ_{min} of 1.5-2.0% for single-crystal BYC,²¹ and values less than 3.0% have been observed experimentally in epitaxial thin films produced by post-deposition annealing at 900°C in oxygen.⁹¹

A similar relationship was observed between the smoothness of the BYC films and the post-deposition annealing conditions. The tendency toward a denser and more platelike morphology with decreasing oxygen pressure that was noted by Feenstra and coworkers⁷⁹ for coevaporated *ex situ* films is also seen in the SEM micrographs of TFA-derived films presented in Section 3.2. Further improvement in the smoothness of the films was obtained by annealing at higher temperatures in reduced $P(\text{O}_2)$ atmospheres, as is evident in Figures 3.11 and 3.12. The micrographs in Figures 3.12a and 3.12b, which compare films annealed in a 250 ppm oxygen atmosphere at 720 and 830°C, respectively, suggest the nucleation rate decreases and the BYC growth rate increases as annealing conditions approach the BYC decomposition line.

Feenstra et al.⁷⁹ hypothesized that this effect of annealing $P(\text{O}_2)$ and temperature on microstructural evolution in BYC thin films was a result of lattice instabilities in highly oxygen deficient $\text{Ba}_2\text{YCu}_3\text{O}_{7-x}$. The annealing conditions used to synthesize the BYC films with the best superconducting properties in this study correspond to an oxygen

nonstoichiometry of $x > 0.90$ based on thermogravimetric analyses of bulk $\text{Ba}_2\text{YCu}_3\text{O}_{7-x}$.⁹² The CuO layers in the tetragonal BYC structure are nearly free of oxygen ions at these compositions. Feenstra et al. argued that the presence of large numbers of vacancies on the oxygen sublattice may induce transformations of lattice units within the crystal structure, resulting in the migration of cations and faster growth kinetics. Siegal and coworkers⁸⁸ noted, however, that the morphologies of their coevaporated *ex situ* BYC films, which were annealed above 800°C under similar low $P(\text{O}_2)$ conditions, suggested they may form from a melt.

Growth of BYC in the presence of a copper-containing liquid could also explain the variation in film roughness and crystalline quality with annealing $P(\text{O}_2)$. The surface tension of copper-containing oxide melts is sensitive to the local oxygen ambient.⁹³ Decreasing the oxygen partial pressure at a given temperature above a partial melting point is expected to sharply decrease the surface tension of the liquid phase, perhaps promoting more rapid growth and densification of the BYC films. Increasing the ratio of growth rate to nucleation rate in the films will increase the size of the BYC grains and, therefore, improve the crystalline quality and smoothness of the films. Experiments undertaken to determine whether a transient liquid phase forms in the temperature/ $P(\text{O}_2)$ regime used to grow the TFA-derived BYC films are described in Chapter 4.

The pin holes present in these MOD-derived BYC thin films may be a consequence of porosity present in the intermediate films prior to crystallization. As discussed in Section 2.3, enclosed porosity has been observed in many oxide films prepared through deposition and decomposition of metalorganic solution precursors. Micropores in sol-gel derived LiNbO_3 thin films, for example, were found to coarsen into larger pin holes after annealing at 700°C.⁷⁵ A similar process may account for the formation of the faceted pin holes in TFA-derived BYC thin films. The SEM results presented in Figure 3.10, which indicate the relative density of the TFA-derived films increased with increasing film thickness, are interesting and perhaps counter-intuitive. Elimination of pores through diffusion to the free surface will become easier as the film

thickness decreases, resulting in higher film density. The anisotropic growth kinetics of BYC imply that growth in the plane of the c-axis normal epitaxial films should occur more quickly than upward growth into the intermediate film.¹³ Thicker intermediate films may require significantly longer times than films of 70-80 nm thickness to completely transform to the final oxide. If this situation prevails, there will be additional time for redistribution of material across the thicker films through surface diffusional processes. Deep depressions, which appear to be pin holes that have been partially "filled in", are frequently observed in the thicker TFA-derived films, as shown in Figure 3.10c. The presence of a wetting liquid phase during growth of the BYC film could aid in this process of pore elimination.

Presence of 90°-misoriented grains in the TFA-derived BYC films is expected based on observations of epitaxial thin films prepared by other *ex situ* techniques.^{79, 88, 94} The observation of an approximately constant density of c-axis in-plane crystallites as a function of film thickness suggests that almost all of the 90°-misoriented nuclei form early on in the transformation process, probably on the substrate surface simultaneously with nucleation of the c-axis normal material. Similar behavior was noted by Nieh and coworkers⁹⁵ in sputter depth profiling of *ex situ* BYC films deposited by e-beam coevaporation on (100) LaGaO₃ substrates. In that case, however, the top portion of films of greater than 400 nm thickness was found to be dominated by the c-axis in-plane orientation. Nieh et al. argued that the anisotropic growth kinetics of BYC caused the c-axis normal crystallites to cover almost all of the substrate's surface following nucleation. The crystallites of the c-axis in-plane material that nucleated on the substrate grew more rapidly upward into the unconverted precursor film and thus came to dominate the upper portions of relatively thick films. The orientation of the thickest films described in Section 3.3 was almost entirely c-axis normal based on SEM characterization reported in that section and TEM results discussed in Chapter 5. Comparison of the observations reported in this thesis with those described in reference 95 suggests that the annealing conditions used by Nieh and coworkers (850°C/humid O₂) resulted in a higher initial density of c-axis in-plane nuclei than present in the TFA-derived films shown in

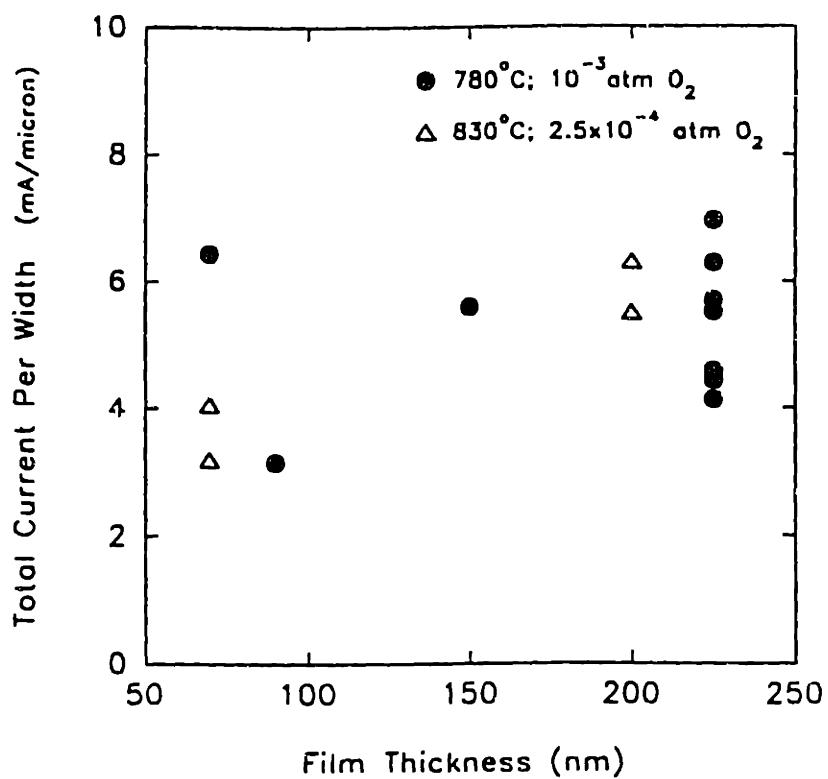


Figure 3.15 Plot, calculated from data in Fig. 3.9, of current that could potentially be carried in a one micron-wide line of TFA-derived BYC film as a function of film thickness.

Figure 3.10 (annealed at 830°C in a humid, 250 ppm oxygen gas mixture). This conclusion agrees with the findings of Feenstra et al.⁷⁹, Siegal et al.⁸⁸, and the J_c and RBS data in Figures 3.3 and 3.6, respectively. The amount of c_1 orientation present in the films tends to decrease as the annealing temperature is increased above 750°C and the annealing $P(O_2)$ is reduced below 1 atm, subject to maintaining stability of BYC against decomposition at low $P(O_2)$'s.

The relationship between the thickness of the TFA-derived BYC films and their critical current density (Fig. 3.9) suggests that the bulk of the supercurrent is carried in a relatively thin layer near the film/substrate interface. Taking account of the width of the scribed bridge for each sample tested, Figure 3.9 was transformed to a plot of current carried per micron width of line versus film thickness. This is shown in Figure 3.15, which indicates a roughly constant value of 4-6 mA/ μ m across the range of film thicknesses investigated. It is expected that very thin films (perhaps ~50 nm thick) will possess some asymptotic value of J_c that may be limited by the mechanism of flux vortex pinning in the films. Such behavior would reduce the value of current carried per micron line width for the very thin films. A possible correlation between the J_c versus film thickness relationship and inhomogeneities in extended microstructural defects in the TFA-derived films is discussed in Chapter 5.

3.5 SUMMARY

Superconducting $Ba_2YCu_3O_{7-x}$ thin films with $T_c(R=0)$ greater than 92 K and J_c (zero field) in excess of 5×10^6 A/cm² at 77 K were prepared reproducibly by a metalorganic deposition process. The highest critical current densities and crystalline quality were observed in films of 70-80 nm thickness annealed at temperatures in the range 780 to 830°C in oxygen partial pressures of 250 ppm to 1000 ppm. Degradation of electrical transport properties was observed at lower annealing temperatures and higher oxygen pressures. Annealing at relatively high temperatures and low $P(O_2)$'s promoted the evolution of the smoothest c-axis normal BYC films and appeared to suppress the

nucleation of 90°-misoriented grains. The smoothness and density of the films were further enhanced by increasing the film thickness, although this was found to decrease the critical current density. This effect of film thickness on J_c suggests the majority of the current in the superconducting films is carried near the BYC/LaAlO₃ interface.

CHAPTER 4

NUCLEATION AND GROWTH OF TFA-DERIVED EPITAXIAL BYC FILMS

4.1 BACKGROUND

Only a relatively small number of studies have focused on nucleation and growth phenomena in BYC thin films. These have generally addressed the early stages of growth in films produced by *in situ* deposition. In *in situ* pulsed laser deposition, for example, it is possible to stop the deposition process after only a few laser pulses and then examine the BYC nuclei directly by TEM. Studies of this kind have been reported by Norton and Carter⁹⁶ for deposition on electron transparent (100) MgO substrates. The substrates were prethinned by mechanical polishing, dimpling, and ion milling to perforation. Plan view TEM samples that required no further ion milling were, therefore, prepared directly by deposition onto these substrates. The thinned substrates were not flat, but instead were terminated by vicinal surfaces following dimpling and ion milling. The MgO substrates were annealed at 1350°C in air just prior to deposition in order to induce the formation of terraced steps through faceting of the substrate surfaces. Norton and Carter observed preferential nucleation of both c-axis normal and c-axis in-plane crystallites at the steps. The films formed by nucleation and growth of isolated islands that did not coalesce until relatively thick films (>35 nm) had been deposited. Growth of BYC on (100) MgO appeared to occur, therefore, in the Volmer-Weber growth mode. Nucleation of the islands on substrate steps was found to control the orientation of the nuclei so that the final film obtained after coalescence of the islands was single crystal-like and had only slight misorientations between adjacent subgrains.²⁶ The epitaxial registry of the BYC

was lost in films deposited on non-prethinned (100) MgO substrates that were not annealed prior to deposition.²⁵ These results suggest that growth of BYC films on (100) MgO is an example of graphoepitaxy.⁹⁷

The importance of substrate surface preparation has also been recognized for the perovskite-like substrates. Meyer et al.²¹ found a significant RBS dechanneling yield due to surface disorder on (100) SrTiO₃ substrates received from a commercial vendor. Ion etching with 400 V argon ions followed by annealing at 950°C in oxygen produced a (100) SrTiO₃ surface yield that was similar in magnitude to that predicted for the "perfect" surface, based on Monte Carlo calculations. Feenstra et al.⁷⁹ reported that predeposition annealing of (100) SrTiO₃ substrates at 900-950°C in oxygen reduced the density of c-axis in-plane grains in their *ex situ* derived BYC thin films. Chan and coworkers¹³ observed preferential nucleation of BYC grains near the edges of SrTiO₃ substrates in *ex situ* films and hypothesized that these nucleated due to defects induced by saw cutting of the single crystal wafers. This hypothesis was confirmed recently by atomic force microscopy (AFM) studies of the (100) surface of acid-etched SrTiO₃ substrates.⁹⁸ Substrates were exposed to an aqueous dislocation etchant solution of nitric acid and hydrofluoric acid at room temperature and then imaged at high magnification by AFM. Etch pits of 80 nm to 1 µm diameter were revealed after 40 s in the solution. The geometry of the etch pits indicated they signified the presence of dislocations with mixed screw and edge nature, with the former type dominating. Eissler et al.⁹⁸ estimated the average density of dislocations across the substrate as $2-3 \times 10^9 \text{ cm}^{-2}$. The pit density near the centers of the substrates had decreased to $3 \times 10^4 \text{ cm}^{-2}$ after three min of etching. The dislocation density near the edges of the saw cut substrates remained significantly higher than this, however. These results imply that a high density of dislocations having a predominantly screw nature are produced during cutting of the SrTiO₃ boules into wafers and dicing of the wafers into individual substrates. Dislocations are expected to act as preferred sites for nucleation of the BYC film⁹⁹, in keeping with the observations of Chan et al.¹³

A screw dislocation growth mechanism has been observed by AFM and scanning tunneling microscopy (STM) of *in situ* derived (001)-oriented BYC thin films produced on a variety of single crystal substrates.¹⁰⁰⁻¹⁰² This growth mechanism occurs by attachment of atoms to the spiral step emanating from a screw dislocation that intersects a crystal's surface.¹⁰³ Screw dislocation growth is commonly observed in crystal growth at low supersaturations¹⁰⁴, as in growth from the vapor or dilute solution, where screw dislocations are the only effective step sources. The mechanism becomes less significant at higher supersaturations (or driving forces) where steps can be formed by two dimensional nucleation on the crystal surface.¹⁰⁵ Gerber and coworkers¹⁰⁰ observed a screw dislocation spiral density of $1-3 \times 10^9 \text{ cm}^{-2}$ in films deposited on (100) SrTiO₃ by *in situ* magnetron sputtering. This is similar to the density of etch pits detected by Eissler et al.⁹⁸ on the surfaces of as-received (100) SrTiO₃ substrates, suggesting the growth spirals in the films nucleate at substrate dislocations. It should be noted, however, that not all *in situ* derived BYC films appear to grow by the screw dislocation mechanism. Screw dislocation growth occurs in BYC films under specific growth conditions determined by substrate type, oxygen partial pressure, growth temperature, and (in *in situ* processes) deposition rate. A terraced island film morphology is also commonly observed on heteroepitaxial BYC films.¹⁰⁶ Studies using STM and AFM on *in situ* films deposited under various conditions suggest that the growth morphology changes from terraced islands to screw dislocation spirals to a smooth layered structure as the deposition rate decreases.^{107, 108}

The understanding of the epitaxial nucleation and growth process in *ex situ* derived BYC thin films is considerably less well-developed than that of the *in situ* films. Direct observation of heterogeneous nucleation by TEM is complicated in partially transformed *ex situ* films because an overlayer of unconverted intermediate material obscures the nuclei when imaged in plan view. Published studies of BYC films prepared by e-beam coevaporation and post-deposition annealing have sometimes attempted to infer an understanding of the nucleation and growth process from the final microstructure of the

films.⁸⁸ As discussed in Chapter 3, Nieh et al.⁹⁵ used ion sputtering depth profiling to characterize changes in film microstructure with thickness. The observations of switching in BYC orientation from c-axis in-plane (c_{\parallel}) to c-axis normal (c_{\perp}) with increasing depth into the film were used to develop a numerical simulation for the film growth process. The simulation assumed the c_{\perp} and c_{\parallel} crystallites nucleated together at the substrate surface. Knowledge of the nucleus density and the relative growth rates of BYC parallel to the c-axis and in the (001) plane (growth rates along the a- and b-axes were assumed to be equal) were required. A random distribution of c_{\perp} and c_{\parallel} nuclei was selected as an initial condition and these were allowed to grow by stepwise advancement of the c-axis (slow) and (001) (fast) growth fronts, with predetermined probability of advancement at each step (interval). The difference in growth rates normal and parallel to the c-axis was reflected in the probability ratio for advancement at each step in the simulation. Growth of individual crystallites was assumed to cease after impingement with neighboring grains. Nieh et al.⁹⁵ chose nuclei densities of 10^9 cm^{-2} for c_{\perp} and $2 \times 10^8 \text{ cm}^{-2}$ for c_{\parallel} crystallites and assumed a growth rate ratio of 10:1 for (001) plane growth versus c-axis growth, based on their TEM observations. The simulated microstructure accurately represented the occurrence of $45^\circ c_{\perp} / c_{\parallel}$ grain boundaries and the variation of crystallographic texture with film thickness as observed in their BYC films deposited on (100) LaGaO₃ and annealed at 850°C in humid oxygen. In cross-sectional views of the simulated microstructure, c_{\parallel} crystallites were only rarely seen to intersect the substrate surface, also in keeping with cross-sectional TEM results.

The results of this simple simulation are impressive in that they accurately represent some important microstructural features of the *ex situ* derived BYC films. However, the model is of little use as a tool for engineering particular microstructures in the films because it does not attempt to simulate the actual nucleation and growth mechanisms. The literature surveyed in this section and the results in Chapter 3 suggest that the microstructural evolution in the films is controlled by fairly complex interactions among factors such as the density of various substrate defects and the annealing temperature and oxygen partial pressure. Furthermore, certain important assumptions

were made in constructing the model that were not supported by experimental evidence. It was assumed, for example, that heterogeneous nucleation sites were distributed at random across the substrate surface, when experimental data suggested this was not the case. Nieh et al.⁹⁵ noted the presence of clusters of 90°-misoriented grains in *ex situ* BYC films on (100) LaGaO₃ and suggested that these formed due to inhomogeneities in the distribution of surface defects on the substrates. They also reported that the c_{\parallel} grain density on LaAlO₃ was similar to that on LaGaO₃, but was an order of magnitude lower on (100) SrTiO₃.

Experimental studies of the mechanisms of heteroepitaxial nucleation and growth in TFA-derived *ex situ* BYC films are described in the remaining sections of this chapter. Studies described in Section 4.2 attempted to determine the role played by substrate defects in heterogeneous nucleation of both c_{\perp} and c_{\parallel} crystallites on single crystal LaAlO₃ surfaces. In some of these experiments, TFA-derived films were prepared on artificially stepped LaAlO₃ substrates that have been demonstrated to result in c_{\parallel} nucleation in *in situ* derived BYC films.¹⁰⁹ The objective of the work in Section 4.3 was to identify, in qualitative terms, the mechanism by which the BYC nuclei grow and the microstructure of the films evolves. These experiments involved quenching partially transformed TFA-derived films from different points in the growth heat treatment. A similar approach was recently used by Parker et al.¹¹⁰ to study nucleation and growth of *ex situ*-derived BaFe₁₂O₁₉ on single crystal sapphire. The main experimental tool used in both the nucleation and the growth studies was cross-sectional high resolution TEM.

4.2 EFFECT OF SUBSTRATE TOPOGRAPHY ON NUCLEATION

4.2.1 Introduction

The discussion in Section 4.1 presented a great deal of direct and indirect experimental evidence indicating the importance of the single crystal substrate surface in

nucleation of BYC films prepared by both the *in situ* and *ex situ* techniques. One approach to understanding the effects of the LaAlO_3 surface structure on the resulting BYC microstructure is to artificially produce specific defects at predetermined locations on the substrates. Photolithography and ion beam etching techniques have been developed by several groups to produce artificially stepped (001) LaAlO_3 and (001) SrTiO_3 surfaces. It has been demonstrated¹¹¹ that steep steps of ~ 100 nm height parallel to the [100] or [010] of the substrates can create well-defined, isolated 90° tilt boundaries in overlying BYC films produced by *in situ* pulsed laser deposition. These step induced boundaries are of interest because they have been observed to behave as intrinsic Josephson tunnel junctions¹¹² (see Chapter 5).

Three [100] 90° grain boundary structures are commonly observed in epitaxial BYC thin films: symmetrical (S) and basal-plane-faced (BPF) tilt boundaries, and twist boundaries (T) with a (100) boundary plane.¹¹³⁻¹¹⁷ These boundary structures are shown schematically in Figure 4.1. Marshall and Eom¹¹⁸ have recently reported that truly symmetric 90° [100] tilt boundaries do not occur in BYC films. Approximately symmetric (AS) tilt boundaries are observed instead, in which microfaceting occurs due to interfacial strain associated with lattice mismatching across 90° [100] tilt boundaries in this orthorhombic material. Marshall and Eom identified several microfacet structures in AS boundaries: BPF facets, mixed T and BPF facets, and lattice-mismatched-symmetrical (LMS) tilt boundaries. These structures are shown in Figure 4.2. Symmetric tilt and twist segments of 90° [100] boundaries are not expected to contribute to weak link behavior in films on artificially stepped substrates because continuity of the CuO_2 layers of the BYC is maintained across these boundary structures.⁵ The continuity of the CuO_2 layers is interrupted at BPF facets and LMS boundary segments. Eom et al.¹¹⁷ found the reduction in J_c due to transport across 90° tilt boundaries in *in situ* deposited (103)-oriented BYC films scaled with the fraction of the boundaries that contained BPF facets. Weak link behavior was not, however, exhibited by these film, perhaps due to the prevalence of twist facets on the boundaries.

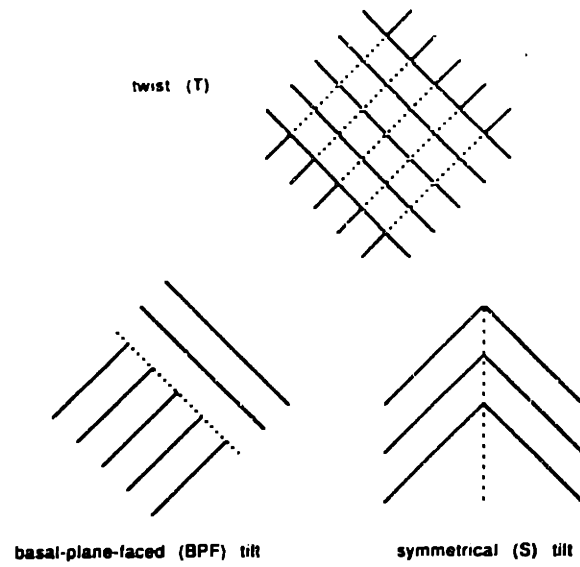


Figure 4.1 Idealized structures of [100] 90° grain boundaries in $\text{Ba}_2\text{YCu}_3\text{O}_{7-x}$.

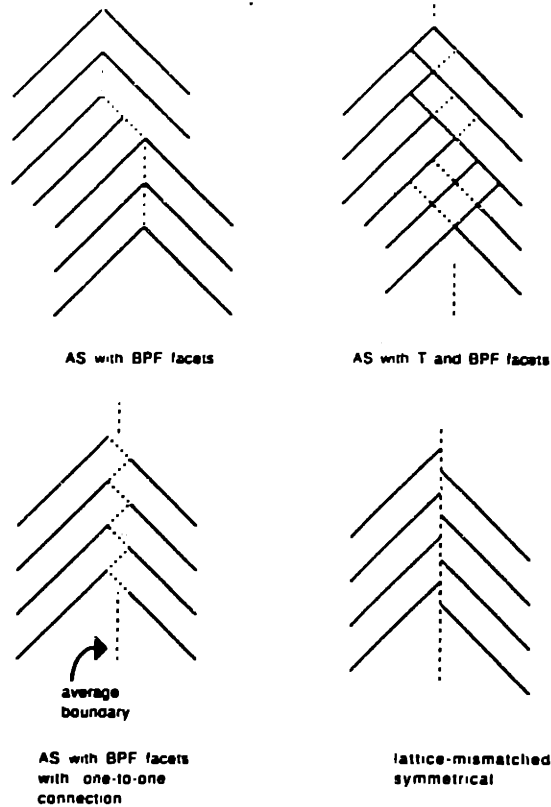


Figure 4.2 Grain boundary microfacet structures in approximately symmetric (AS) 90° [100] tilt boundaries in BYC (from reference 118).

In Section 4.2, studies of BYC nucleation on artificially stepped substrates are combined with recent findings concerning native steps on the (001) LaAlO_3 surface. Heterogenous nucleation of BYC in both *in situ* deposited and *ex situ* TFA-derived films is characterized and compared. The effects of substrate defects produced unintentionally through wafer cutting and substrate dicing on orientation of the heteroepitaxial films are also described.

4.2.2 Experimental Procedure

Artificially stepped LaAlO_3 substrates were prepared by J.Z. Sun of International Business Machines Corp. by photolithography and ion beam etching of nominally flat (001) LaAlO_3 . A photoresist spinner was used to coat square (001) LaAlO_3 substrates (12.5 mm side length) with photoresist. A spinning rate of 4500 rpm resulted in a resist thickness of $\sim 1\ \mu\text{m}$. The photoresist layer was exposed to UV light through a chromium-plated glass contact mask with $2\ \mu\text{m}$ line width and $2\ \mu\text{m}$ line separation. The masked-off resist was removed and a diamond-like carbon film was deposited through the lines in the resist that had been exposed to UV. The diamond-like film was found to be essentially impervious to low energy ion bombardment and, therefore, was used as a physical mask for ion beam etching of the LaAlO_3 . The specimens were mounted in a dedicated ion etching chamber on a liquid nitrogen-cooled cold stage. A 5 in Kauffman ion source was used to generate a beam of Ar^+ ions with 500 eV energy and $300\ \mu\text{A}/\text{cm}^2$ ion fluence at normal incidence to the masked substrate. The etch rate for the (001) LaAlO_3 surface under these conditions was $\sim 6.7\ \text{nm}/\text{min}$.¹¹⁹ Channels with 180-260 nm depth and steeply sloped step edges were etched into the substrate through the physical mask. The carbon mask was subsequently stripped off the substrate by reactive ion etching.

Films of BYC were deposited on the stepped substrates by both spin-on deposition and annealing of metal TFA precursors in our laboratory and by *in situ* pulsed laser deposition at IBM. The PLD-derived films of 100-150 nm thickness were deposited at a nominal substrate heater temperature of 790°C in a chamber backfilled with 300 mTorr

oxygen. This oxygen pressure is equivalent to ~395 ppm at 1 atm total pressure. Laser parameters were controlled to produce a deposition rate of ~0.1 nm/s. The TFA-derived BYC films were synthesized using the procedure outlined in Chapter 3. The precursor concentration and spin coating speed used to deposit films on the artificially stepped substrates were adjusted to yield films that would have 200-250 nm thickness on flat LaAlO_3 substrates. All the chemically derived films described in this nucleation study were annealed for 1 h at 830°C in a humidified oxygen/nitrogen gas mixture with 250 ppm oxygen content.

Thinned cross-sections of the films were prepared for TEM imaging by mechanical thinning and ion milling. The mechanical grinding and polishing of the specimens was performed using a modification of the tripod polishing technique developed by Benedict et al.¹²⁰ Film/substrate samples were fractured and glued film-side-down to 0.002 in thick pieces of single crystal sapphire. A thermosetting epoxy¹²¹ that required a 2 h bake at 140°C was used as the adhesive. A plane of polish that was normal to the [100] or [010] zone axis of the LaAlO_3 substrates was selected through observation of the twin patterns in the LaAlO_3 using an optical microscope. The glued samples were ground and polished from one side to give a flat cross-section plane with a smooth finish produced by polishing with 1 μm diamond paste on photographic paper. The polished cross-section sides of the specimens were then glued with the same thermosetting epoxy to nickel aperture disks with a 600 μm diameter circular aperture. The substrate/film/sapphire sandwiches were placed on the disks so that the glue line separating the BYC film from the sapphire bisected the aperture. The specimens on the disks were baked to cure the epoxy and then glued disk-side-down to the tripod polishing mount using acetone-soluble Crystalbond.¹²² The tripod polisher was used to gradually feed the unpolished side of each specimen into the rotating grinding and polishing wheels, while maintaining the desired plane-of-polish (normal to the [100] or [010] zone axis of the substrate). Final polishing was performed using 9 μm diamond paste on photographic paper to obtain a cross-section thickness of ~50 μm . The polished cross-sections specimens (on the nickel grids) were removed from the polisher by brief (~1 h) immersion in acetone. The ~50

μm -thick specimens were then dimpled¹²³ to $<5\ \mu\text{m}$ thickness using a texmet cloth-padded dimpling tool and $3\ \mu\text{m}$ diamond slurry. Low dimpling forces (5-10 g) and low tool speeds (20 rpm) were found to give the best results in preparing these and other brittle oxide specimens. The dimpled cross-sections were ion milled to perforation with 4 kV Ar^+ ions. Initial milling was performed without active cooling of the samples at a thinning angle of $\sim 15^\circ$. Final milling was performed at a thinning angle of $\sim 11^\circ$ in a Gatan Duomill equipped with a liquid nitrogen cold stage.

The microstructures of the thinned cross-sections were characterized by high resolution TEM using an Akashi EM002B operating at 200 kV. Gold-coated plan view specimens of both the PLD- and TFA-derived BYC films were examined by SEM at 25 kV.

4.2.3 Observations

The SEM micrographs in Figure 4.3 of a PLD-derived film of $\sim 110\ \text{nm}$ thickness on a stepped single crystal substrate indicate the smoothness and density of these films. No pin holes, surface particles, or c_1 outgrowths are evident in the plan view image in Figure 4.3a. The quality of the lithography varied across the stepped substrates. The region in Figure 4.3a has substrate patterning defects in the lower portion of the image and more regular surface relief near the top of the image. The cross-sectional image (Fig. 4.3b) shows the stepped geometry of the sample at fairly low magnification. Higher magnification imaging of the thinned cross-sections in the TEM (Fig. 4.4) indicates the c-axis orientation changes that occur in the BYC film across the step slopes. The trenches in the (001) LaAlO_3 substrate shown in Figure 4.4 are $\sim 260\ \text{nm}$ deep. The average BYC film thickness is about $150\ \text{nm}$, although the thickness of the film on the step slopes and near the bottom corners of the steps is clearly substantially less. The step on the right side of the figure makes an angle of $\sim 80^\circ$ with the bottom of the trench and an angle of $\sim 60^\circ$ with the top of the substrate plateau in the image. The angle between the plateau surface and the step slope on the left of the image is only 54° . This

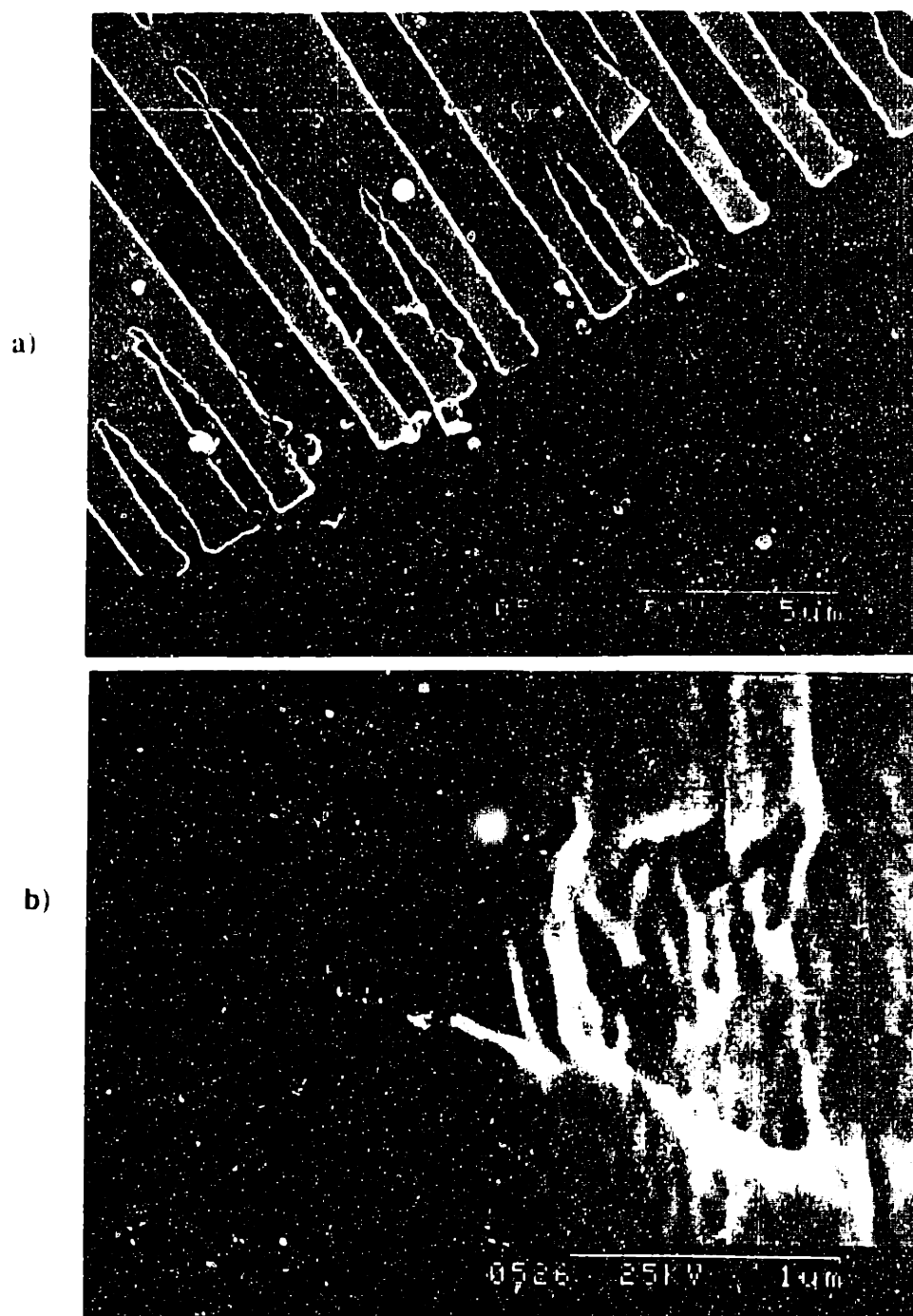


Figure 4.3 Scanning electron photomicrographs in a) plan view and b) cross-section of a BYC film deposited *in situ* by pulsed laser deposition on an artificially stepped single crystal substrate.



Figure 4.4 Cross-sectional TEM image near the [001] zone axis of a PLD-derived BYC film on stepped (001) LaAlO_3 .

discrepancy in step angles on the left and right sides of the plateaus was observed to occur across the specimen. Even at the relatively low (for TEM) magnification in Figure 4.4, the 1.17 nm c-axis lattice spacing of the BYC is evident in the image. The orientation of the PLD-derived film was found to be c-axis normal in all of the "flat" trench regions that were examined. Multiple orientations are apparent in the film on the step slope, with a small c_1 crystallite visible in the film above the top corner of the step in the right of the image. The multiple BYC orientations are also evident in the selected area electron diffraction pattern for the region. The intense spots making a square net in the diffraction pattern are due to the LaAlO_3 substrate (a-axis spacing = 0.379 nm) aligned near its [100] zone axis. The weaker spots occurring with spacings of approximately 1/3 the length (in reciprocal space) of the LaAlO_3 reflections are due to the BYC film (c-axis spacing = 1.168 nm). The presence of two orthogonal sets of spots resulting from diffraction from the (00 l) planes indicates the 90° misorientation present in the film in the selected area.

A higher magnification TEM micrograph taken at the bottom corner of the step on the right of Figure 4.4 is shown in Figure 4.5. A meandering 90° [100] tilt boundary separates the c-axis normal BYC film on the trench from the predominantly c-axis in-plane film on foot of the step. Examination of the step slopes indicate they are not extremely smooth. The step foot region in Figure 4.5 is, in fact, the steepest portion of the step. The BYC film in this region has the largest c_1 domain on the step, located on the left side of the grain boundary in Figure 4.3. The 90° grain boundary contains microfacets of several kinds and some lattice mismatched regions. Areas of the boundary in Figure 4.5 containing these microfacet structures are labeled as follows: a) basal-plane-fronted (BPF) facets, b) twist (T) facets, and c) a lattice-mismatched-symmetrical structure (LMS). Low angle grain boundaries separating the large c_1 domain from an approximately c_1 domain above are also present in this region and are indicated by the dashed lines in the figure. Stacking faults along the [001] direction of the BYC are present in the film on both sides of the 90° grain boundary in the figure. These stacking faults have been frequently reported in *in situ*-derived BYC films and are



Figure 4.5 Higher magnification image of the lower step corner region on the right side of the image in Fig. 4.3.



Figure 4.6 Cross-sectional image of the PLD-derived film above the lower step corner in Fig. 4.3

crystallographically related to other Ba-Y-Cu-O compounds.^{94, 124} Stacking faults formed by insertion of an additional CuO plane along the c-axis (structurally related to the $\text{Ba}_2\text{YCu}_4\text{O}_x$ phase) are indicated in Figure 4.5 by open arrows. Polytypoidal stacking faults in BYC thin films will be discussed in greater detail in Chapter 5.

The TEM image in Figure 4.6 was taken from an area "higher up" along the same step. In this area, the c_{\parallel} domain shown in Figure 4.5 gives way to a region with both c_{\parallel} and c_{\perp} orientation. The small c-axis normal domains are concentrated near the LaAlO_3 step surface and often appear to be associated with bumps or microsteps in the step slope (see arrowed region in Fig. 4.6). Many of the boundaries separating the 90° -misoriented domains in Figure 4.6 have a twist character (labeled T). The effectiveness of microsteps on the LaAlO_3 in nucleating small 90° -misoriented BYC domains is indicated in Figure 4.7, an image from a different step in another area of the same PLD-derived cross-section specimen. The BYC film in contact with this rough, faceted region of the substrate surface is decomposed into a series of 90° twist boundaries, apparently due to the intersection of small domains of the two orientations. Microsteps in the LaAlO_3 surface are indicated in the image by filled arrows. Larger domains of either c_{\parallel} or c_{\perp} orientation formed farther from the interfacial region. The boundaries between the interfacial BYC and the larger domains have a basal-plane-fronted character.

The microstructure of the TFA-derived films deposited on the same stepped LaAlO_3 substrates was found to be significantly different from that of the *in situ* films. The plan view SEM images in Figure 4.8a and 4.8b show the surface of two chemically derived films of similar average thickness (200-250 nm), heat treated identically, on stepped (Fig. 4.8a) and nominally flat (Fig. 4.8b) (001) LaAlO_3 . The sharply defined plateau and trench structure of the substrate, that was evident through the overlying PLD-derived film in Figure 4.3, cannot be seen clearly in Figure 4.8a. The corrugations in the substrate surface instead produce a rippled appearance in the TFA-derived films. The density of c_{\parallel} outgrowths is much higher on the stepped substrate film than on the film in Figure 4.8b. These c-axis in-plane crystallites are concentrated on the steps and the



Figure 4.7 High magnification image of LaAlO₃ micro steps and 90°-misoriented BYC domains in a PLD derived film on a step slope

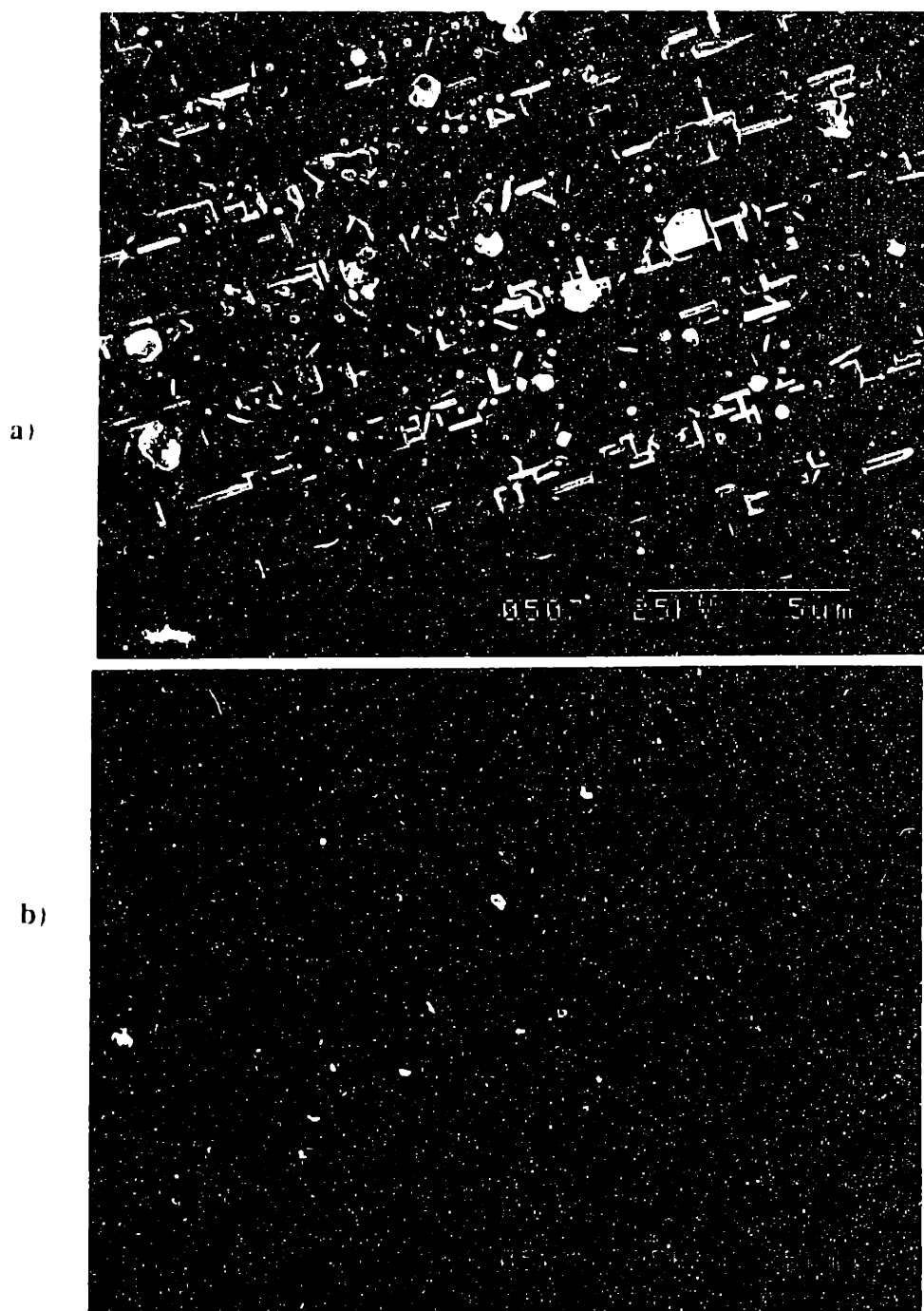


Figure 4.8 Plan view SEM micrographs of TFA-derived films of 200-250 nm nominal thickness deposited on a) artificially stepped (~ 200 nm step height) and b) nominally flat (001) LaAlO_3 .

plateau tops. In several areas, long c_1 grains run parallel to the step edges, along the [100] direction of the substrate. Grains having c -axis in the plane of the film, but lacking the usual registration with respect to the substrate are also visible in Figure 4.8a. Several of these outgrowths (indicated by filled arrows) appear to run parallel to the [110] direction of the LaAlO_3 ; however, other grains, which appear to be c_1 BYC, seem to have their c -axes oriented randomly in the (001) plane of the substrate. These c_1 grains with variable registration in the (001) substrate plane have not been observed previously in SEM images of the TFA-derived films on nominal flat substrates. The chemically derived BYC film on the stepped substrate also appears to be somewhat more porous than the film on the flat substrate. Pin holes visible in Figure 4.8a appear to have formed preferentially near the edges of the steps on the substrate.

The effect of the stepped substrate topography on the TFA-derived films' orientation is indicated in the cross-sectional TEM image in Figure 4.9. The film in the trench and on most of the plateau surface is c -axis normal. However, a relatively large c_1 crystallite that evidently runs parallel to the [100] axis of the substrate is present on the top corner of the step region in the center of the image. The c -axis in-plane grains were typically observed to make contact with the substrate surface, as in Figure 4.9. They were most frequently found to have formed at the edges of the plateaus (the top corners of the steps). This was true even in cases, such as that shown in the figure, where the LaAlO_3 steps had a sharp inflection due to an error in the lithography process. In Figure 4.9, the bottom half of the step is nearly vertical, almost paralleling the substrate [001] direction. The BYC film near the foot of this step is much thinner than the surrounding film and was apparently amorphized by ion milling. It is believed a pin hole or surface depression in the film existed in this region and resulted in increased local ion damage to the film.

The higher magnification image in Figure 4.10, taken from the top corner of a different step than the one shown in Figure 4.9, indicates an absence of the mixed orientation observed in Figures 4.6 - 4.7 in the PLD-derived films on the step slopes. A

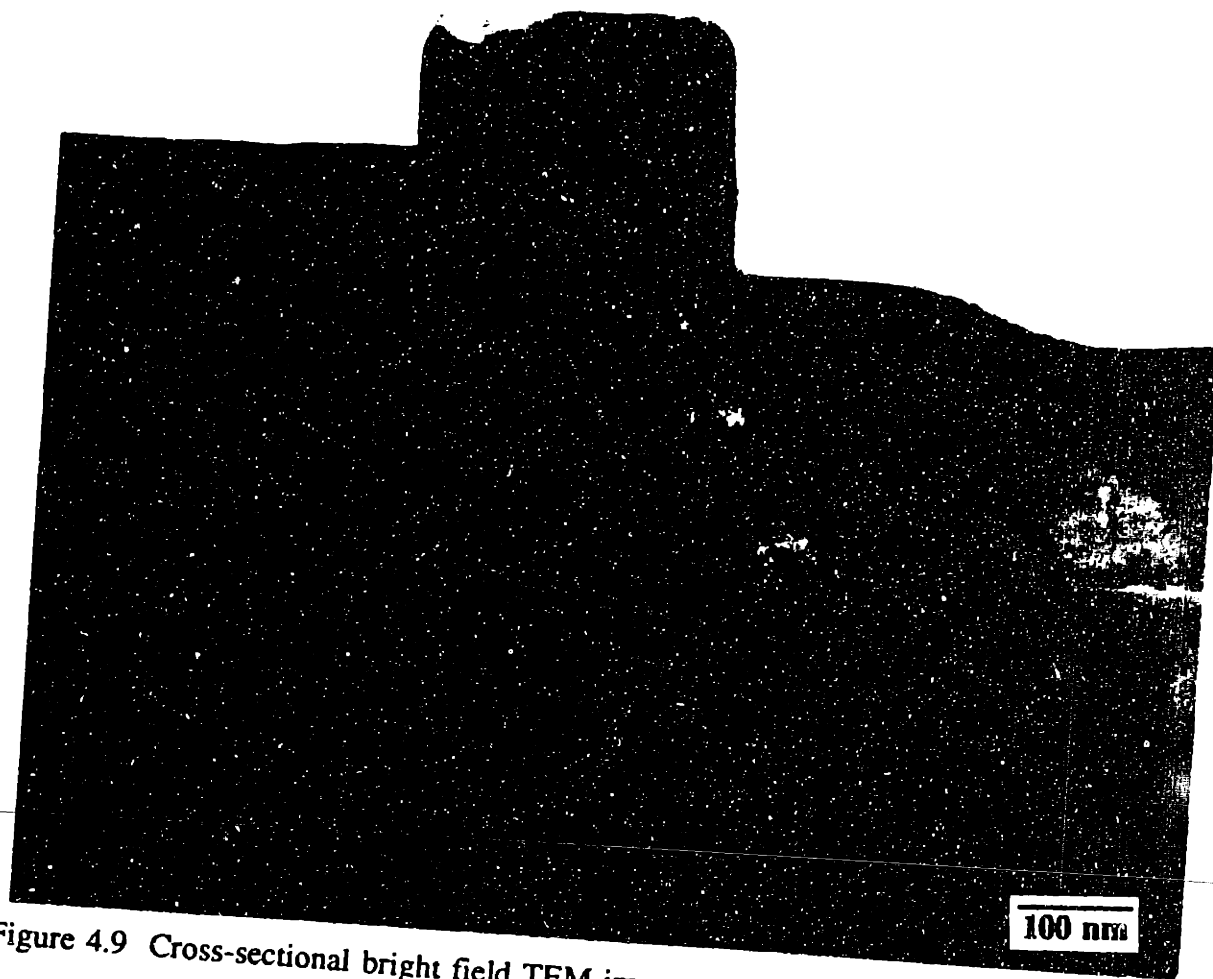


Figure 4.9 Cross-sectional bright field TEM image near the [100] zone axis of a TFA-derived BYC film on stepped (001) LaAlO_3 .

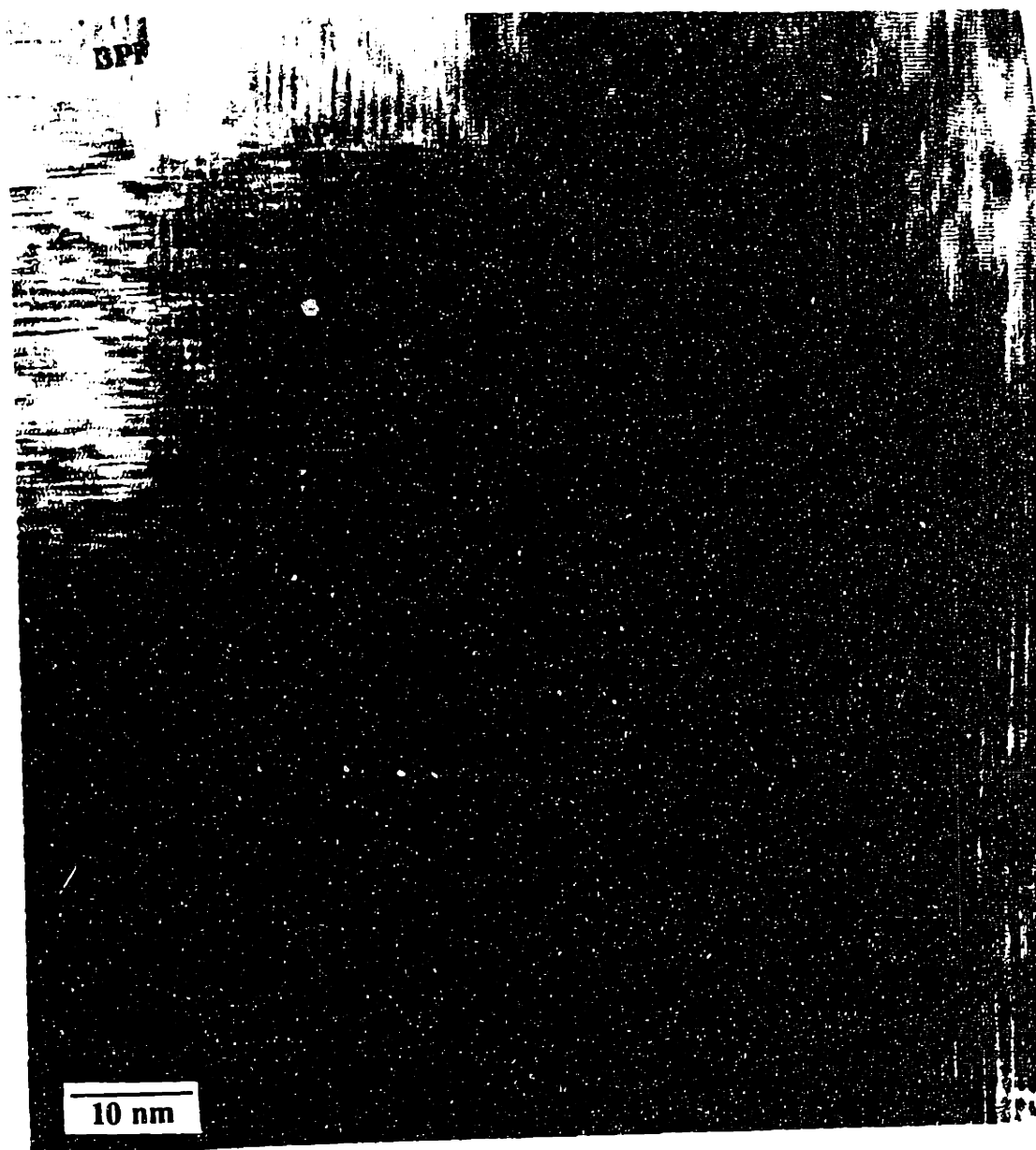


Figure 4.10 Higher magnification cross-sectional image of the TFA-derived BYC film at the top corner of an artificial substrate step.

large c_{\parallel} crystallite is present near the top of the step, while the film on the plateau is dominated by the c_{\perp} orientation. The grain boundary separating the two well-defined, 90°-misoriented domains in this region has basal-plane-fronted (BPF) and twist (T) components, as indicated in the figure. The portion of the boundary near the right side of the image is obscured due to the thickness of the TEM specimen. Polytypoidal stacking faults are also present in the chemically derived films and several faults in this region are marked by open arrows.

The possible contribution of substrate dicing defects to the formation of c_{\parallel} grains was investigated by plan view optical microscopy of TFA-derived BYC films of ~350 nm thickness. As discussed in Chapter 3, the size of the 90°-misoriented outgrowths was found to increase as the BYC film thickness increased in these *ex situ* films. It was found that optical microscopy was a quick and fairly accurate (as determined by supporting SEM work) technique for observing qualitative changes in the areal density of c_{\parallel} outgrowths across the samples in these thicker films, where the outgrowths were long enough to be observed easily at relatively low (~400 x) magnification. Optical micrographs and a schematic "map" of the film showing the areas from which the micrographs were taken are shown in Figure 4.11. The orientation of the LaAlO_3 substrate is also indicated. The film in this figure was annealed using the standard high temperature heat treatment described in Section 4.2.2. The c-axis in-plane outgrowths are visible in the optical micrographs as 1-2 μm long, dark needles parallel to the [100] or [010] substrate directions. The areal density of observable c_{\parallel} outgrowths was typically lowest near the center of the films (Fig. 4.11a). The outgrowth density in the film near the substrate edges was often much higher, as shown in Figure 4.11b. In this image, impingement of adjacent c_{\parallel} grains can be seen. This was very rarely observed in imaging of the centers of films prepared under the same conditions used to synthesize the film in Figure 4.11, as evidenced by the SEM micrographs in Chapter 3. Significant variations in areal density of observable c_{\parallel} grains were also found from one substrate edge to another, as shown in Figure 4.11c and 4.11d. The density near the edges, however, always appeared greater than that near the center of the film.

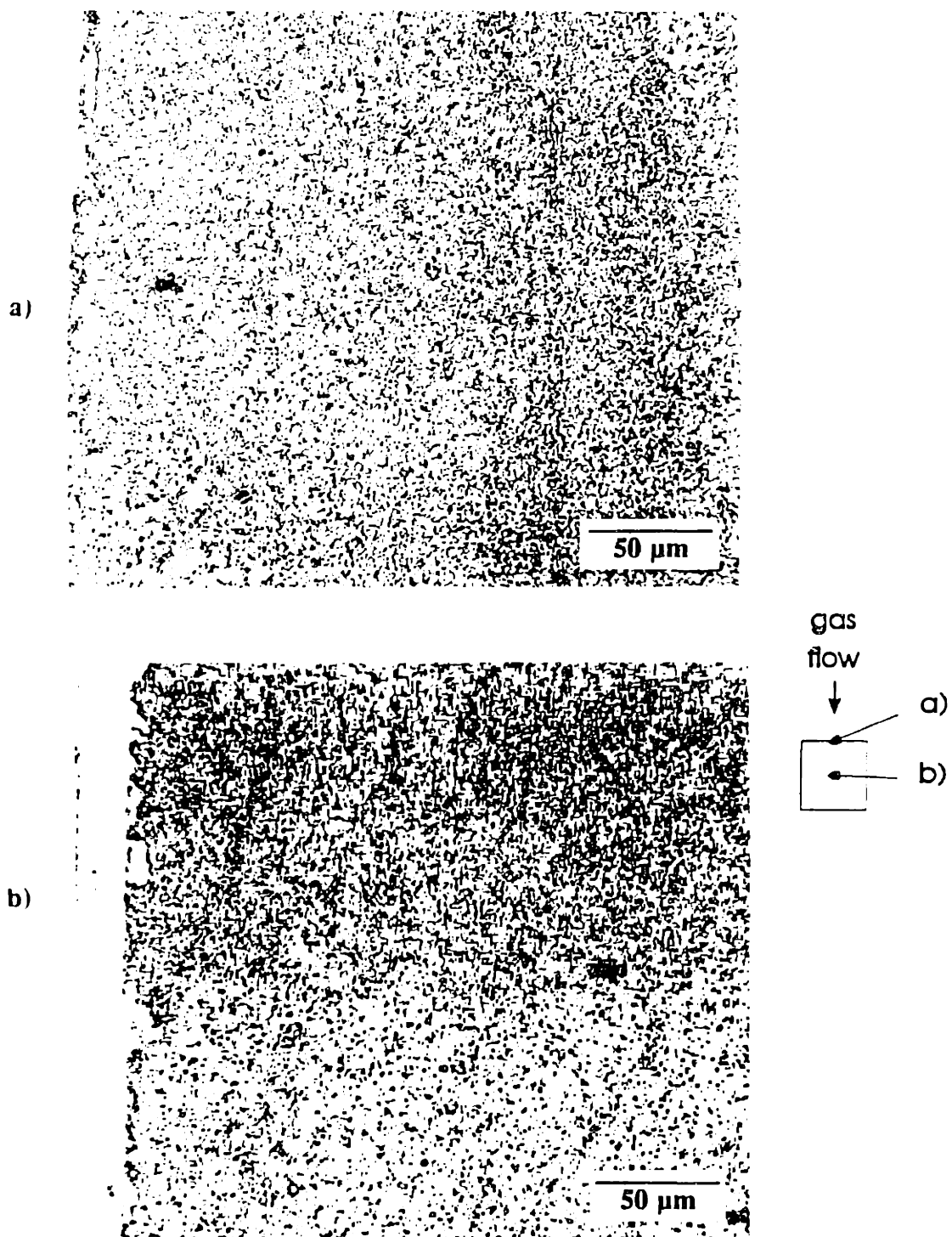


Figure 4.11 Optical photomicrographs taken from different positions on the surface of a TFA-derived BYC film of ~ 350 nm thickness and a "map" showing the regions of the film from which the images were taken.

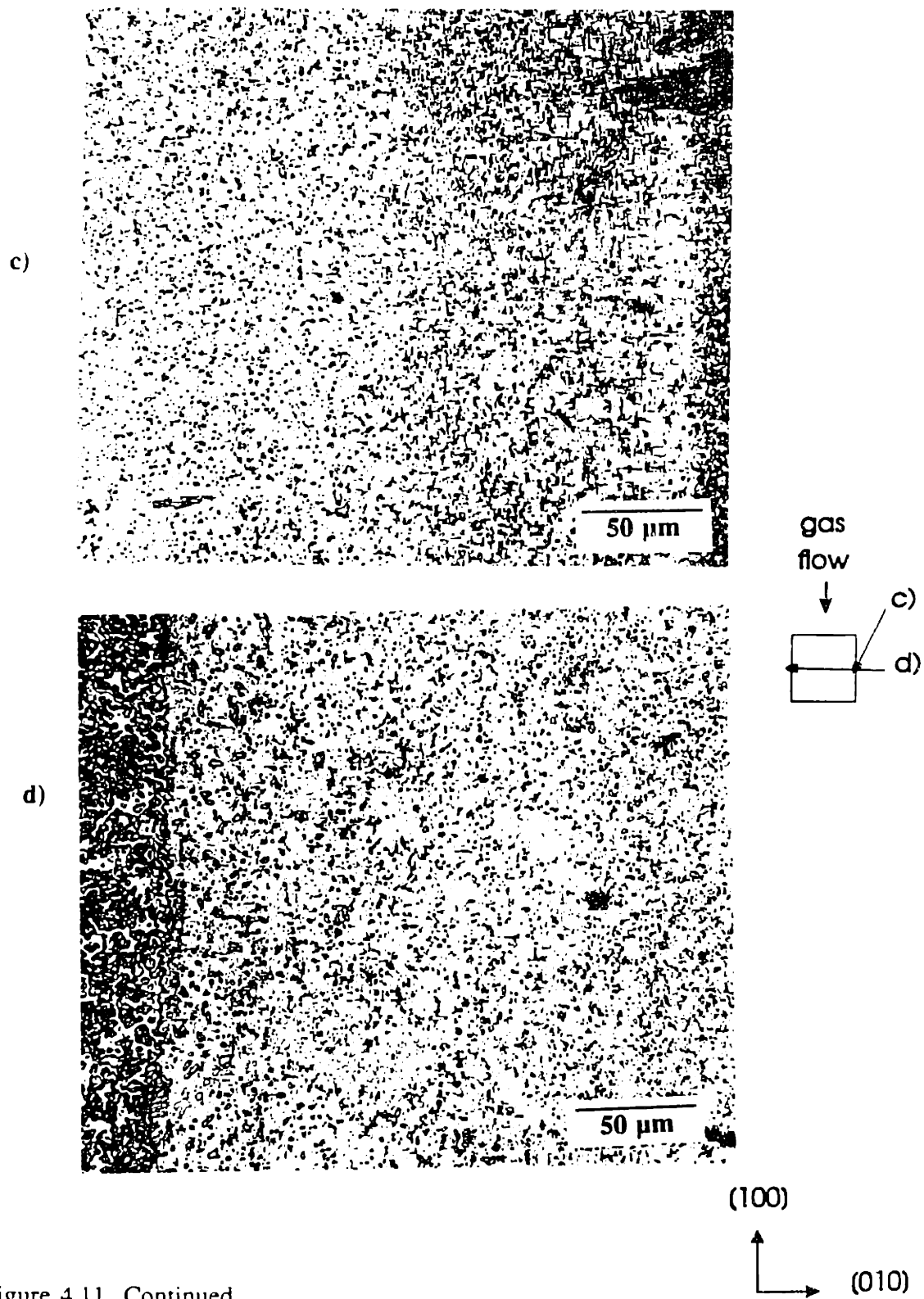


Figure 4.11 Continued.

4.2.4 Discussion

The observed ability of substrate steps to affect the orientation of BYC thin films has important implications for controlling the presence of c_{\parallel} grains and associated grain boundaries in the films. Use of BYC thin films in applications requiring reproducibly good transport properties across long patterned lines requires the elimination of these defects, or, at a minimum, a very low density of small ($< 1 \mu\text{m}$ length) misoriented grains. Devices based on the observed Josephson tunneling characteristics of some BYC grain boundaries¹²⁵, require controlled formation of 90° boundaries of known size and structure at particular sites on a substrate. The observations described in Section 4.2.3 also shed light on the nature of nucleation in BYC films and contrast the nucleation and growth processes that occur using *in situ* and *ex situ* techniques.

It is clear from the images in Figures 4.3-4.10 that the density of nuclei that formed on the surface of the stepped LaAlO_3 substrates is significantly lower in the TFA-derived BYC films than in films produced by pulsed laser deposition. The difference in appearance of the film in the interfacial region on the step slopes is particularly dramatic. Microsteps on the LaAlO_3 surface in these areas appear to act as preferred sites for heterogeneous nucleation of the *in situ* deposited film. Their presence results in the formation of the small BYC domains with orthogonal orientation shown in Figure 4.7. A similar two-fold orientation was reported by Jia and coworkers¹¹¹ in PLD-derived BYC films deposited on artificially stepped (100) SrTiO_3 substrates in which the steps had intermediate steepness (step angles between 40° and 52°). At step angles greater than $\sim 52^\circ$, only c_{\parallel} orientation was observed on the steps with two well-defined 90° [100] tilt boundaries separating the c_{\parallel} film from the c_{\perp} film on the neighboring trench and plateau regions. In films grown on SrTiO_3 substrates with step angles less than 40° , the c -axis normal BYC was found to overgrow the steps, thus avoiding formation of 90° grain boundaries. Jia et al.¹⁰⁹ used similar ion etching techniques to pattern steps with an $\sim 80^\circ$ step angle into (001) LaAlO_3 single crystal substrates. Pulsed laser deposited BYC films on these substrates did not possess the two-fold orientation on the steps. Instead, a single

c_{\parallel} domain was observed on each step. The step surfaces on their LaAlO_3 substrates were somewhat smoother than those prepared at IBM and studied in the present work. This reduced step roughness may have resulted from a pre-deposition anneal at 1000°C in flowing oxygen that Jia et al. used to reduce surface damage to the substrates caused by ion milling. The observed nucleation of c_{\perp} domains in the steep step region imaged in Figure 4.7 was probably caused by the high surface roughness of the LaAlO_3 substrate that was not pre-annealed. Damage to the surface of the stepped substrates may also have been responsible for nucleation of the c_{\parallel} outgrowths in the TFA-derived films that had principal axes that were rotated relative to those in the LaAlO_3 (see Fig. 4.8a).

The microstructure of the TFA-derived films grown on the stepped substrates is significantly different from that of the PLD-derived films. The former contain much larger, well-defined c_{\parallel} grains that grow out beyond the surface of the surrounding c_{\perp} material. Regions of two-fold orientation composed of small orthogonal domains are not observed on the step slopes. Instead, single c_{\parallel} crystallites are observed on the steps in cross-section, typically having nucleated at the top corners of the steps. The remaining portions of the steps are generally overgrown by c -axis normal film. This is true even in extremely steep-sided step geometries where c_{\parallel} domains are always present in the PLD-derived films.

The difference in the microstructure of films produced by the two techniques suggests that the ratio of growth rate to nucleation rate (G/I) in the TFA-derived films studied is significantly higher than that in the PLD-derived films. The stepped regions of the LaAlO_3 substrates are clearly preferred sites for nucleation of BYC, in keeping with the observations of Norton and Carter⁹⁶ for BYC growth on vicinal MgO . The tendency of the c -axis normal BYC of the TFA-derived films to overgrow even the steepest portions of the steps suggests that nucleation occurs more rarely in these films than in the PLD-derived films. Rapid advancement of the c_{\perp} growth front in the TFA-derived films may saturate potential nucleation sites on the LaAlO_3 surface before nucleation can occur at them. When a c_{\parallel} nuclei does form on a step in these films, it appears to grow rapidly

upward from the BYC/LaAlO₃ interface and is not overgrown by c_⊥ material. The fact that the c_{||} grains in Figures 4.9 and 4.10 also grew to be significantly wider (longer in the BYC [001], slow-growth direction) than the c_{||} domains in the PLD-derived films is another indication that the nucleation rate is smaller in the *ex situ* films studied.

The cross-sectional TEM micrographs of the PLD-derived films and the plan view SEM micrographs of the TFA-derived films indicate the ion-etched steps in the LaAlO₃ substrates act as preferred sites for the nucleation of c_{||} grains. This suggests misoriented BYC grains may form preferentially at large native steps in the LaAlO₃. There are, in fact, several reports of preferential nucleation of c_{||} BYC grains on native substrate steps. Basu et al.⁹⁴ observed nucleation of c_{||} domains at large surface steps on (100) SrTiO₃ in *ex situ*-derived BYC films deposited by e-beam coevaporation. Figure 7 in a recent paper by Traeholt and coworkers¹²⁶ shows a c_{||} grain in an *in situ* PLD-derived film that grew up from the substrate surface after apparently nucleating at one of two adjacent surface steps in (100) MgO. A similar situation is presented in Figure 4.12, a cross-sectional TEM micrograph showing the BYC/LaAlO₃ interfacial region in a TFA-derived film of ~350 nm thickness deposited on a nominally flat LaAlO₃ substrate. A large misoriented BYC grain appears to have nucleated at the interfacial step near the center of the image. This crystallite is not precisely 90°-misoriented relative to the single crystal substrate and appears to be somewhat damaged from the ion thinning process; however, this image suggests the c_{||} grains in these chemically derived films nucleate on the LaAlO₃ surface due to the presence of large native steps. Nucleation of c_{||} grains at the substrate surface is in keeping with the observations of approximately constant areal density of c-axis in-plane grains as a function of film thickness in Chapter 3.

Steps may form in the LaAlO₃ surface due to the presence of twins in the crystal. As described in Chapter 2, LaAlO₃ is a twinned rhombohedral crystal at room temperature that contains a nearly cubic perovskite-like pseudocell. It undergoes a structural phase transformation to cubic at ~450°C, far below the growth temperatures employed in either the *in situ* or *ex situ* BYC synthesis techniques. Lanthanum aluminate wafers that contain

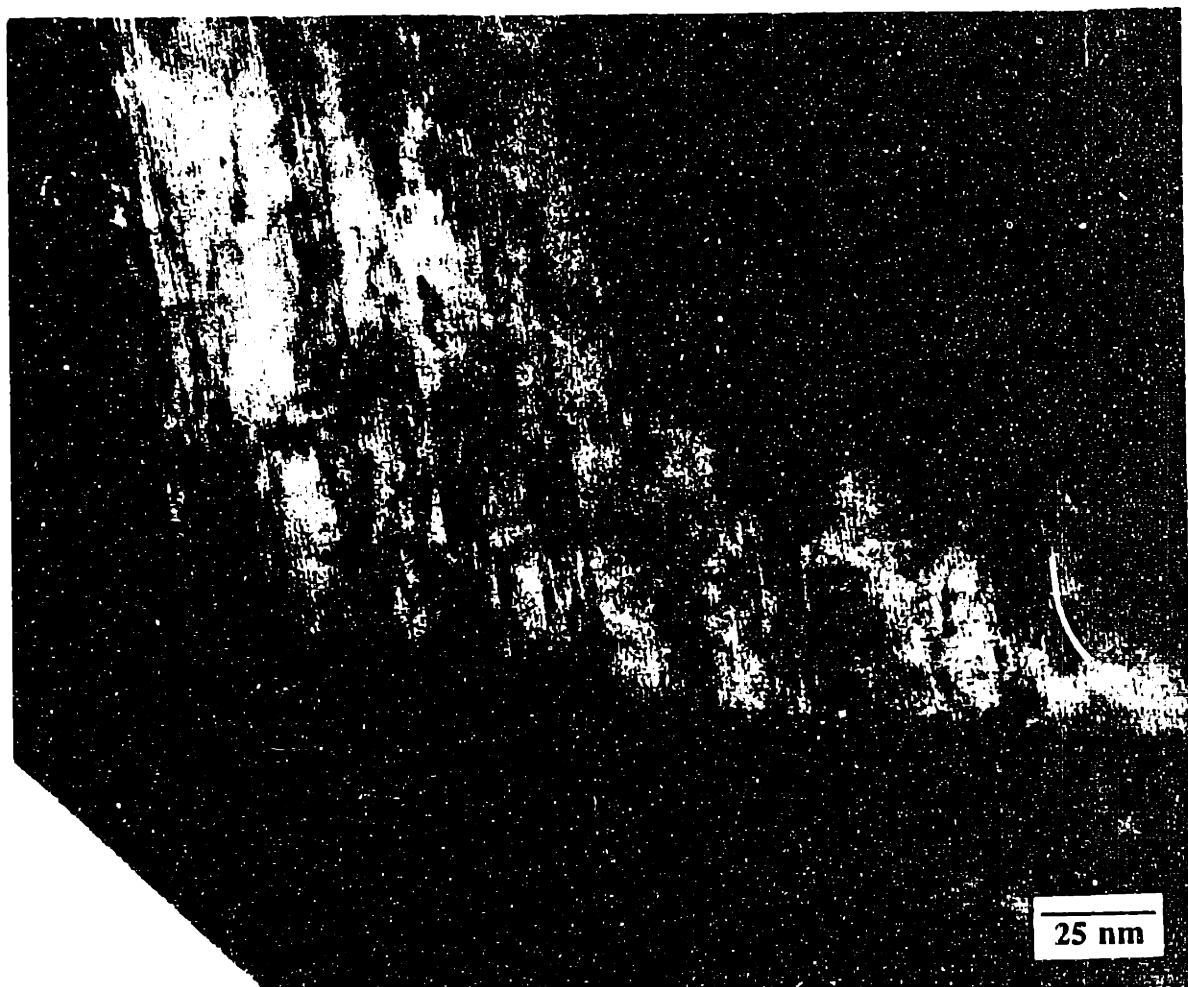


Figure 4.12 Cross-sectional bright field TEM image near the $[100]$ zone axis of a TFA-derived BYC film of ~ 350 nm thickness showing a nearly- c_1 grain on a LaAlO_3 region containing a large surface step (near the right side of the image).

numerous twins with (100) and (010) twin boundaries (and less numerous twins on the {110}-type planes) are polished relatively flat by the vendor prior to film deposition. Twinned regions may develop surface steps above 450°C due to shear strain associated with the *r-c* transformation. This has recently been observed by Chang¹²⁷ in AFM images of polished (001) LaAlO₃ substrates heated above the transformation temperature and slow cooled to room temperature. Most of the steps in the AFM images of the LaAlO₃ surface were only one unit cell in height (0.379 nm), although several larger steps (2-3 unit cell step height) were found. Native surface steps running along the [100] and [010] directions would have the same orientation as the artificial steps created in the LaAlO₃ substrates described in Section 4. The results of that section indicate that, if sufficiently large, they would be effective nucleation sites for c₁ grains.

This effect was recently observed in a chemically derived BYC film of 400-500 nm nominal thickness. The optical micrograph in Figure 4.13a shows the presence of bands of very high areal density of c₁ outgrowths separated by regions of lower density. The bands in the figure run parallel to the [100] direction of the substrate. The lower magnification image of the same film in Figure 4.13b indicates the pattern of high c₁ density is similar to the twin structure that is typically observed in the as-received LaAlO₃ substrates. High c₁ density bands can be seen to run parallel to both the <100>- and <110>-type directions of the substrate. An unusually high density of c-axis in-plane grains are visible in this sample. Even the regions of relatively low density in Figure 4.13a have a higher density of c₁ crystallites than is normally observed in specimens prepared using the standard (830°C/250 ppm O₂) heat treatment (cf. Fig. 4.11). However, the pattern of concentrated c-axis in-plane crystallites suggests that steps present in the substrates due to detwinning at elevated temperatures act as preferred sites for nucleation of the c₁ crystallites. This hypothesis is consistent with reports of Nieh et al.⁹⁵ of much higher c₁ grain areal density in BYC films deposited on LaAlO₃ and LaGaO₃ than was observed in films on SrTiO₃. Lanthanum gallate, like LaAlO₃, is twinned at room temperature due to a structural phase transformation at ~150°C³⁰, whereas SrTiO₃ substrates can be synthesized without twins. Furthermore, additional twinning in LaAlO₃

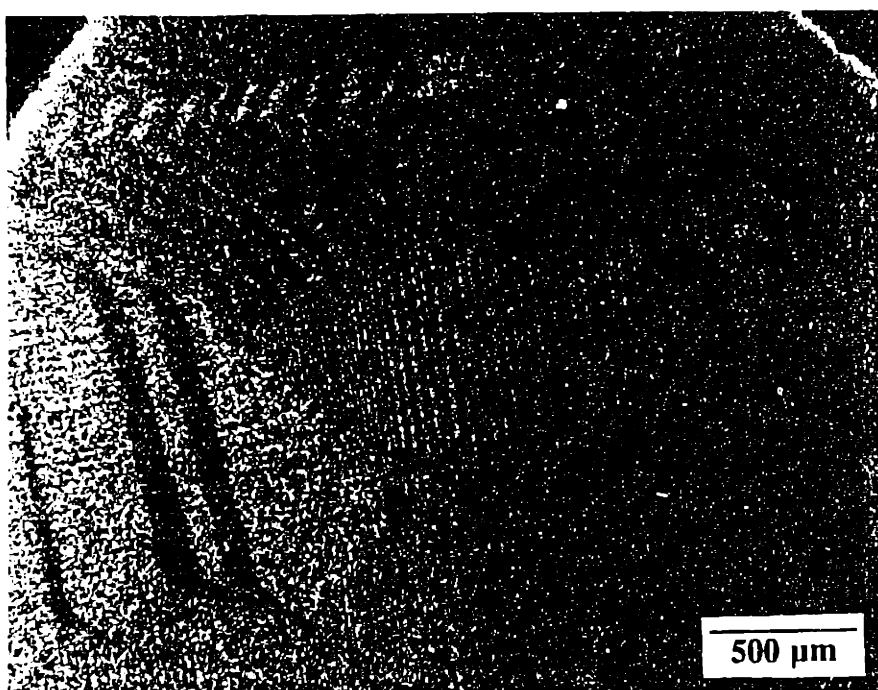
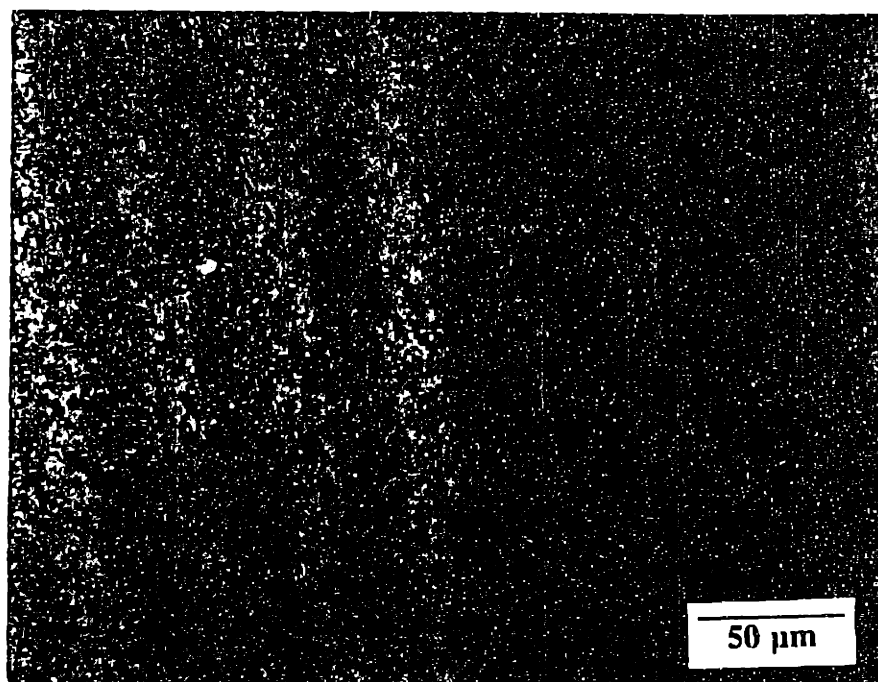


Figure 4.13 Optical photomicrographs of a film of 400-500 nm thickness on nominally flat (001) LaAlO_3 showing an unusually high areal density of c_{\parallel} grains and variations in c_{\parallel} density that appear similar to the twin structure of the substrates.

has been observed to occur at the substrate edges after dicing the single crystal wafers in our laboratory. This may lead to formation of a higher step density near the edges of the substrates and enhanced c_1 nucleation there, as suggested by the micrographs in Figure 4.11.

4.3 TRANSFORMATION OF THE TFA-DERIVED INTERMEDIATE TO BYC

4.3.1 Introduction

Published reports of epitaxial growth of several different oxides were reviewed in Section 2.3.3. Those reports described two mechanisms which were believed to be responsible for the observed evolution of the microstructures. Miller et al.^{73, 128} observed epitaxial grain growth in homoepitaxy of yttria-stabilized ZrO_2 . In this process, grains in a polycrystalline film that have a low interfacial energy due to lattice matching with the substrate grow at the expense of grains that lack the favorable orientation.⁷¹ Epitaxial grain growth typically requires long duration anneals at high temperatures to produce single crystal-like films. Nashimoto and coworkers⁷⁵ found evidence of a more rapid growth mechanism in the crystallization of sol-gel derived $LiNbO_3$ on (0001) sapphire at 400°C. This transformation involved heterogeneous nucleation on a single crystal substrate and solid state growth into a weakly crystalline intermediate. A similar solid phase heteroepitaxial (SPHE) growth mechanism was recently described for *ex situ* growth of $BaFe_{12}O_{19}$ on single crystal sapphire from an amorphous e-beam coevaporated precursor.¹¹⁰ Braunstein and coworkers⁷⁰ reported that either an EGG mechanism or an SPE-like mechanism operated in homoepitaxial growth of chemically derived $SrTiO_3$, depending upon the preparation of the substrate surface. They reported that competition from heterogeneous nucleation sites within the film (such as crystallites of intermediate phases) lead to formation of a polycrystalline $SrTiO_3$ film which only became epitaxial through EGG at very high temperatures.

In this thesis, quenching experiments were used to follow the early stages of

epitaxial growth from the TFA-derived intermediate film. The results presented below indicate that neither the EGG or SPE-like mechanisms are responsible for heteroepitaxial growth of these chemically derived BYC thin films. An alternative mechanism based on partial melting of the intermediate material is described, and experimental results that indicate a liquid phase is stable under the conditions used in the growth heat treatment are presented.

4.3.2 Experimental Procedure

Metalorganic precursor films were deposited onto (001) LaAlO_3 by spin coating the mixed metal TFA solutions, as described in Chapter 3. The solution concentration and spin coating conditions were adjusted to yield final BYC films with 70-80 nm thickness. The green films were converted to the oxygen- and fluorine-containing intermediate films through thermal decomposition in the low temperature heat treatment shown in Figure 3.1. Transformation of the intermediate material to BYC in its tetragonal modification was accomplished in a subsequent high temperature heat treatment in a horizontal tube furnace. The heating profile used in these experiments was based on the standard high temperature heat treatment shown in Figure 3.2, which includes a rapid ($25^\circ\text{C}/\text{min}$) heating (or ramp) from room temperature to the annealing temperature of 830°C . Specimens described in this section were quenched from the growth heat treatment during the later stages of the ramp segment, as the furnace temperature approached 830°C . The furnace atmosphere used during these quenching experiments was an ultrahigh purity oxygen/nitrogen gas mixture containing 250 ppm oxygen and was humidified to a dew point of 20°C , as discussed in Chapter 3. The $P(\text{O}_2)$ of the furnace atmosphere was confirmed by measurements with a ZrO_2 oxygen sensor operating at 800°C . Specimens were quenched from approximately 720°C , 770°C , and 795°C in the ramp portion of the high temperature anneal by removing them from the hot zone and allowing them to cool at the end of the furnace. Temperature measurements made with a type K thermocouple fixed in contact with the quartz furniture that supported the specimens indicated the films were cooled below 500°C within 60 s after removal from

the hot zone.

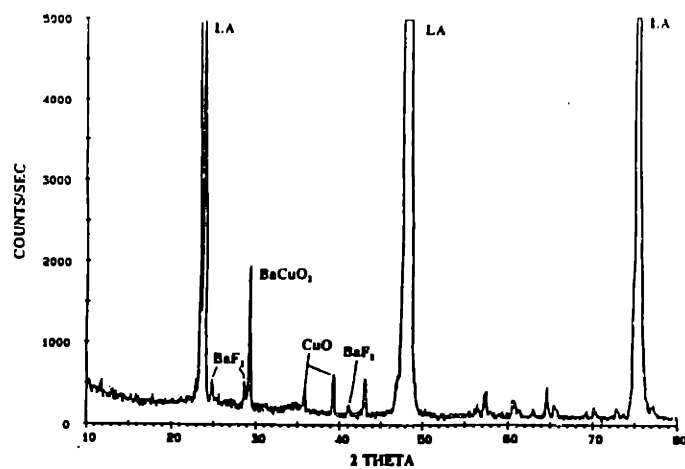
Phase and orientation development in the quenched films were characterized by X-ray diffraction (Rigaku RU300 diffractometer) in the theta/two theta configuration with $\text{Cu(K}\alpha\text{)}$ radiation. Thinned cross-sections of the samples were prepared for TEM examination by the techniques of mechanical thinning and ion milling described in Section 4.2. Cross-sections were imaged at high resolution by TEM (Akashi EM002B) and STEM (Vacuum Generators HB5); chemical microanalysis was performed by EDS during STEM.

Differential thermal analysis (Netzsch STA 429) was used to study partial melting in the Ba-Y-Cu-F-O system. The DTA measurements were made using high purity alumina crucibles and high purity alumina as a reference material. Simultaneous thermogravimetric analyses (TGA's) were acquired during the DTA experiments. This system had previously been used to study peritectic melting behavior in the Ba-Y-Cu-O system.⁸⁶ Powder samples of the oxygen- and fluorine-containing intermediate material were prepared by thermally decomposing a dried powder sample of the metal TFA precursor solution. Alternative powder samples were prepared by accurately weighing out gram quantities of high purity BaF_2 , Y_2O_3 , and CuO powders using an analytical balance that is accurate to less than 1 mg, and mixing the powders to produce the 2:1:3 barium:yttrium:copper metal ratio. Samples of both types of 45-85 mg mass were used in the DTA runs. The sensitivity of the TGA balance was less than 0.1 mg.

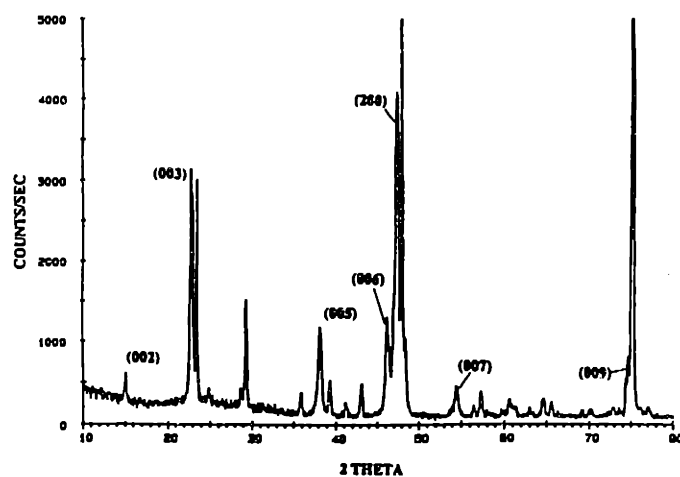
4.3.3 Observations

X-ray diffraction patterns for three quenched specimens are presented in Figure 4.14. No reflections corresponding to BYC were detected in the sample quenched from $\sim 720^\circ\text{C}$ (Fig. 4.14a). Besides the (00 l) LaAlO_3 reflections (labeled LA), peaks assigned to BaF_2 , BaCuO_2 , and CuO were detected. Very sharp peaks associated with both the

a)



b)



c)

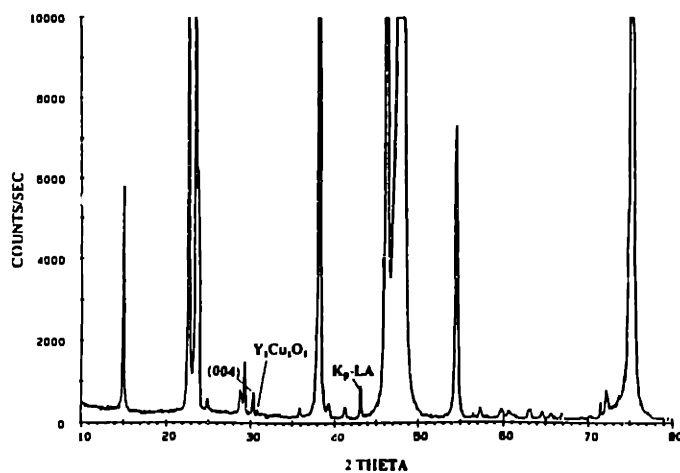


Figure 4.14 X-ray diffraction θ - 2θ scans of films quenched from a) 720°C, b) 770°C, and c) 795°C in the ramp portion of the high temperature heat treatment.

(*h*00) and (00*l*) planes of tetragonal BYC were detected from the specimen quenched from $\sim 770^{\circ}\text{C}$, as shown in Figure 4.14b. The presence of tetragonal BYC indicates the quenching conditions and furnace $P(\text{O}_2)$ did not allow the oxygen uptake and oxygen vacancy ordering required for transformation to the superconducting orthorhombic phase. A slight misorientation of the sample in the diffractometer was probably responsible for the relatively weak signal from the single crystal substrate observed in Figure 4.14b. The (200) BYC reflection was, therefore, not obscured by the (002) LaAlO_3 peak. The same crystalline intermediate phases observed in the sample quenched from $\sim 720^{\circ}\text{C}$ were also detected, although the intensities of their X-ray reflections were reduced by about 20%. The film removed from the hot zone of the furnace at a temperature of $\sim 795^{\circ}\text{C}$ (Fig. 4.14c) had (00*l*) BYC reflections of significantly greater intensity. Barium fluoride, BaCuO_2 , and CuO peaks having similar intensities to those in Figure 4.14b were also detected as was a weak reflection that has been tentatively assigned to $\text{Y}_2\text{Cu}_2\text{O}_5$.

Cross-sectional TEM examination of the quenched thin films yielded results that were in qualitative agreement with those obtained by X-ray diffraction. The film quenched from $\sim 720^{\circ}\text{C}$ in the ramp segment of the heat treatment (Fig. 4.15) was found to be polycrystalline with no evidence of preferred orientation. Electron diffraction analysis at several points along the film cross-section did not indicate the presence of BYC, in keeping with the XRD results in Figure 4.14a. The TEM image in Figure 4.15 indicates the presence of pores 10-20 nm in diameter located near the substrate surface. Pores of this kind were found at several locations along the film/substrate interface in this specimen.

A film that was quenched from approximately 770°C is shown in the TEM cross-section images in Figure 4.16 and 4.17. In this specimen, the surface of the (001) LaAlO_3 substrate was found to be covered by a thin layer of c-axis normal BYC which, in some areas, was only a few unit cells thick. Several c_1 grains were observed in this sample (as shown in Fig. 4.17), but those imaged were not found to be in contact with the substrate surface. The BYC/ LaAlO_3 interface was atomically abrupt, indicating the film



Figure 4.15 Cross-sectional TEM image of the TFA-derived intermediate film quenched from 720°C.



Figure 4.16 Cross sectional image near the $[100]$ zone axis of a TFA-derived BYC film quenched from 770°C .

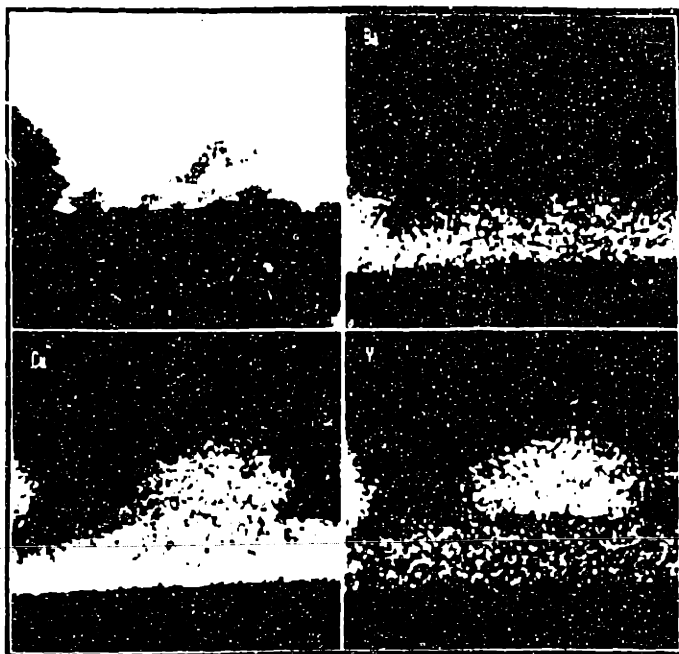


Figure 4.17 Image from another region of the specimen shown in Fig. 4.16.

growth mechanism did not result in significant reaction with the substrate. A layer of rounded 20-60 nm diameter crystalline particles in a matrix of nano-crystalline material covered the top surfaces of the quenched BYC films. This is shown clearly in Figure 4.17. The EDS elemental map in Figure 4.18a was acquired during STEM examination of the region shown in the TEM micrograph in Figure 4.16. Barium is absent from the particle on the surface of the c-axis normal BYC near the center of Figure 4.16; however, strong yttrium and copper signals were detected. The particle has been tentatively identified as $\text{Y}_2\text{Cu}_2\text{O}_5$. The particle in the right of the TEM micrograph is also rich in yttrium and copper but has a stronger barium signal, suggesting it may be BaY_2CuO_5 . The EDS map in Figure 4.18b was acquired from the region in Figure 4.17 and indicates the two crystalline particles that are in contact with the c_1 grains in the TEM image are yttrium- and copper-rich. The nanocrystalline material surrounding the particles is barium-rich. A weak fluorine signal was detected from the nanocrystalline material near the c_1 grain in the right of Figure 4.17. Although fluorine was not found throughout the nanocrystalline regions in the quenched cross-section specimen, it was detected in several locations. This overlying layer of yttrium- and copper-rich particles in a barium-rich nanocrystalline matrix was commonly observed across the surface of the film quenched from 770°C.

An area of a sample quenched from 795°C in the ramp segment of the growth heat treatment is shown in Figure 4.19. The thickness of the BYC film in this region is approximately 40 nm. An untransformed overlayer that had similar chemistry to that observed on the film quenched from 770°C was observed in this specimen. The crystalline particle in contact with the top surface of the film was identified as $\text{Y}_2\text{Cu}_2\text{O}_5$ by EDS. The particle is bounded at the both the right and left sides of the image by the barium-rich nanocrystalline material. Stacking faults in the BYC film that are structurally related to the $\text{Ba}_2\text{YCu}_4\text{O}_8$ phase¹²⁴ are indicated by arrows.

a)



b)

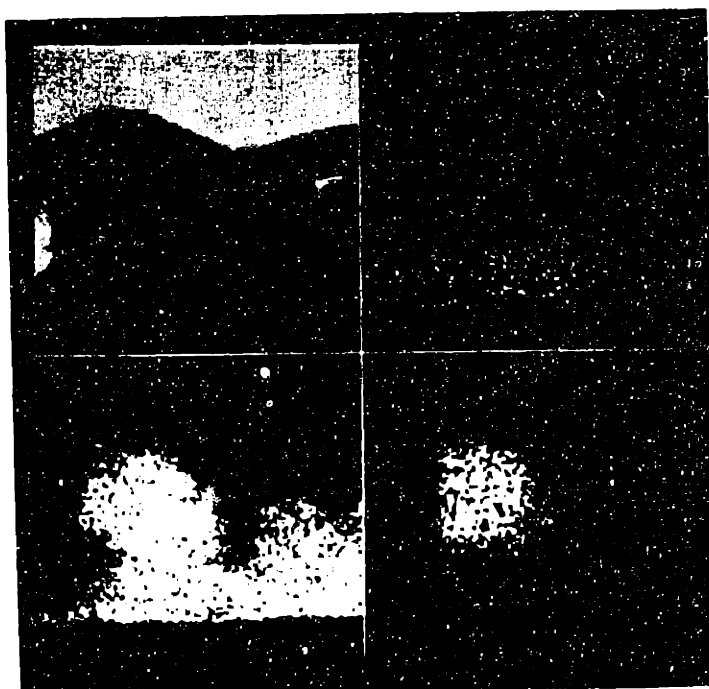


Figure 4.18 Energy dispersive x-ray spectroscopy maps for barium, yttrium, and copper acquired during STEM imaging of the regions in a) Fig. 4.16 and b) Fig. 4.17.



Figure 4.19 Cross-sectional TEM image of a TFA-derived BYC film quenched from 795°C.

4.3.4 Discussion

The X-ray diffraction results in Figure 4.14 indicate epitaxial BYC grows into a polycrystalline intermediate film. Neither the XRD experiments nor the TEM studies detected any evidence of nucleation of BYC that was not lattice matched to (001) LaAlO_3 surface. These results suggest that competition between heterogeneous nucleation sites within the intermediate film and on the substrate surface was not an issue in this system, as it appears to be in several other MOD-derived oxide films.^{63, 70} Cross-sectional TEM observations indicate nucleation of the BYC occurs heterogeneously at the substrate surface between 720 and 770°C in the ramp segment of the heat treatment with 250 ppm oxygen atmosphere. The XRD results suggest that tetragonal BYC having both c-axis and a-axis normal orientation nucleate together on the substrate surface, although the small number of c_1 grains located in the TEM cross-section specimens were not found to make contact with the LaAlO_3 . This is not unexpected, however, based on the predictions of the Nieh simulation⁹⁵ discussed in Section 4.1. If the anisotropic growth kinetics of BYC results in a predominantly c-axis normal orientation near the substrate surface, then sectioning an a-axis normal grain through the original nucleus would be unlikely. The rapid heating rate employed in the ramp segment appeared to delay the nucleation of BYC to higher temperatures than would be observed in an isothermal experiment. Indeed, as discussed in Chapter 3, a BYC thin film with relatively high T_c and J_c was prepared by annealing for 1 h at 720°C in a humid N_2/O_2 atmosphere containing 250 ppm oxygen.

The intermediate film is relatively dense prior to onset of the transformation to the final oxide, particularly in comparison to sol-gel derived films of LiNbO_3 ^{46, 75}. Prior to nucleation and growth of the BYC, the intermediate film contains some enclosed pores of 10-20 nm diameter located near the interface with the LaAlO_3 substrate, as shown Figure 4.15. It is unlikely, however, that these small pores are responsible for much of the porosity observed in the final films. Pin holes with 100-200 nm diameter occur frequently in fully annealed films of 70-80 nm thickness, as shown in Figures 3.10a and 3.12b. The apparent increase in porosity of the films with transformation from polyphase

intermediate to epitaxial BYC is probably a consequence of the volume change during the transformation. Many of the crystalline phases present in the film prior to the transformation have lower densities than BYC (see Table 4.1). As mentioned in Chapter 2, voids may be created in MOD-derived films due to the nucleation and growth process itself if the final crystalline phase has a lower molar volume than the intermediate phase(s). That the TFA-derived intermediate film has a lower molar volume than the final BYC film is evident from the nature of the c_1 outgrowths, which grow upward from nucleation sites at the substrate surface and stop after reaching the top surface of the intermediate film. The fact that these misoriented crystallites extend outward above the top surface of the c -axis normal BYC in the fully-transformed films suggests there is a significant volume change on transformation. This volume change can be estimated by assuming the intermediate film consists of BaF_2 , CuO , and Y_2O_3 (prior to decomposition of the BaF_2 , and formation of BaCuO_2 and $\text{Y}_2\text{Cu}_2\text{O}_5$). The estimated percentage volume change, based on the data in Table 4.1, is ~21%.

The TEM micrographs of the film quenched from ~770°C indicate coalescence of the film on the (001) LaAlO_3 surface occurs early in the transformation process, with essentially complete surface coverage occurring before the 770°C point in the ramp. Growth of the c -axis normal material upward into the polyphase intermediate apparently occurs much more slowly than lateral growth along the film/substrate interface. It is clear, however, that the 70 min anneal at 830°C used in the standard heat treatment described in Chapter 3 is longer than necessary to achieve transformation of the intermediate film to BYC. Conversion of the intermediate film to a BYC film of 70-80 nm thickness is approximately 50% complete after quenching from 795°C in the ramp segment of the heat treatment, based on the observed thickness of the film in Figure 4.19.

The presence of polytypoidal stacking faults in the quenched films, which was also noted in the fully-annealed specimens described in Section 4.2 may indicate rapid growth in the (001) plane of the c -axis normal material. These defects are commonly observed

in cross-sectional TEM micrographs of *in situ* derived BYC films^{124, 129} and are metastable⁹⁰ under the $P(O_2)$ /temperature conditions used in both *in situ* deposition and the low- $P(O_2)$ post-deposition annealing described in this thesis. Studies of their formation in *in situ* BYC thin films suggest that the stacking faults along the c-axis occur because of the rapid advancement of the crystallization front in the (001) plane.¹³⁰ Metastable intergrowths of structurally-related phases will form in a $Ba_2YCu_3O_{7-x}$ matrix if the BYC growth front advances too quickly for diffusional processes or surface chemical reactions to provide the "correct" stoichiometry at the front. Stacking faults related to the 214 and 427 compounds will increase the local copper content of the films, while the 224-type defects identified by Ramesh et al.¹²⁴ will make the films locally yttrium-rich and copper-deficient relative to 213.

It is clear from the preceding discussion and the observations in Section 4.3.3 that neither the epitaxial grain growth or solid phase epitaxial nucleation and growth models accurately describes the mechanism of heteroepitaxial growth in these chemically derived BYC thin films. The BYC nucleation process is epitaxial; the substrate orientation allows only two orientations of tetragonal BYC to form: c-axis and a-axis normal. This situation is not consistent with EGG. Furthermore, recent experiments by Peterson¹³¹ indicate that appreciable grain growth does not occur in polycrystalline BYC thin films at temperatures below their melting point. A purely solid phase epitaxial nucleation and growth mechanism involving reaction and interdiffusion of the various crystalline intermediates is also unlikely, given the observed microstructures of the films. The rapid coalescence of the epitaxial grains into a film with complete surface coverage of the substrate, the observation of polytypoidal stacking faults in the films, and the results in Section 4.2 indicating a higher G/I ratio in the TFA-derived films than in vapor deposited films suggest the lateral growth rate of the c_{\perp} film may be enhanced by the transient presence of a liquid phase. This hypothesis is also consistent with the high relative densities of the fully-annealed films, as discussed in Chapter 3.

Table 4.1: Densities and Molecular Weights of Intermediate Phases and Ba₂YCu₃O_{7-x}

| Phase | MW (g/mol) | ρ (g/cm ³) |
|--|------------|-----------------------------|
| BaF ₂ ¹⁵⁶ | 175.33 | 4.89 |
| BaCuO ₂ ¹⁵⁷ | 232.87 | 5.82 |
| Y ₂ O ₃ ¹⁵⁸ | 225.81 | 5.03 |
| Y ₂ Cu ₂ O ₃ ¹⁵⁹ | 384.90 | 5.44 |
| CuO ¹⁶⁰ | 79.55 | 6.51 |
| BaY ₂ CuO ₅ ¹⁶¹ | 458.68 | 6.20 |
| Ba ₂ YCu ₃ O ₇ ¹⁶² | 666.19 | 6.38 |

Table 4.2: Invariant Reactions near Ba₂YCu₃O_{7-x} at 850°C (from reference 89).

| | P(O ₂) (atm) | Invariant Reaction |
|---|--------------------------|---|
| 1 | 5.5x10 ⁻³ | Ba ₂ YCu ₃ O _{7-x} + BaCuO ₂ + CuO = L + O ₂ |
| 2 | 4.0x10 ⁻³ | 2 CuO = Cu ₂ O + 1/2 O ₂ |
| 3 | 3.0x10 ⁻³ | BaCuO ₂ + L = BaCu ₂ O ₂ + 1/2 O ₂ |
| 4 | 3.0x10 ⁻³ | BaCuO ₂ + L = Ba ₂ YCu ₃ O _{7-x} + BaCu ₂ O ₂ + O ₂ |
| 5 | 2.7x10 ⁻³ | BaY ₂ CuO ₅ + 4 BaCuO ₂ = Ba ₂ YCu ₃ O _{7-x} + Ba ₃ YCu ₂ O _{6+y} + (x-y)/2 O ₂ |
| 6 | 1.5x10 ⁻³ | L = BaCu ₂ O ₂ + Cu ₂ O + Ba ₂ YCu ₃ O _{7-x} + O ₂ |
| 7 | 1.0x10 ⁻³ | 4 Ba ₂ YCu ₃ O _{7-x} + Cu ₂ O = 2 BaY ₂ CuO ₅ + 6 BaCu ₂ O ₂ + (7-4x)/2 O ₂ |
| 8 | 7.0x10 ⁻⁴ | Ba ₂ YCu ₃ O _{7-x} + 3 BaCuO ₂ = Ba ₃ YCu ₂ O _{6+y} + 2 BaCu ₂ O ₂ + (3-x-y)/2 O ₂ |
| 9 | 4.0x10 ⁻⁴ | 7 Ba ₂ YCu ₃ O ₆ = 3 BaY ₂ CuO ₅ + Ba ₃ YCu ₂ O _{6+y} + 8 BaCu ₂ O ₂ + (5-y)/2 O ₂ |

Several investigations have proposed that growth of the layered copper oxides may be assisted by the transient presence of small amounts of liquid phases. Precipitation of platelets of the layered copper oxide $\text{Bi}_2\text{Sr}_2\text{Ca}_2\text{Cu}_3\text{O}_x$ (BSCCO-2223) from small amounts of liquid phase has been observed by Morgan et al.¹³² in bulk samples synthesized from metal oxide powders. They found evidence that small droplets of a Bi-rich liquid, that formed during heating in air above the partial melting temperature of 825°C, dissolved the precursor oxides and deposited thin platelets of "2223" in their wake. Evidence of partial melting of the TFA-derived BYC films heat treated in nitrogen at 920°C was observed in an earlier stage of this project.⁸⁶ Chu et al.⁵³ recently reported the synthesis of epitaxial BYC thin films with J_c ($H_{app}=0$, $T=77$ K) $\sim 10^5$ A/cm² by annealing films derived from metal trimethylacetate precursors in pure nitrogen at elevated temperatures. They hypothesized, based on SEM characterization, that the films grew from a partial melt that enhanced the densification and growth kinetics over those observed at higher oxygen partial pressures.

Beyers and Ahn⁹⁰, in an extensive investigation of the thermodynamics of the Ba-Y-Cu-O system, used coulombmetric titration and X-ray diffraction to study invariant reactions near $\text{Ba}_2\text{YCu}_3\text{O}_{7-x}$ as a function of temperature and $P(\text{O}_2)$. The temperature/ $P(\text{O}_2)$ dependence of the invariant reactions (listed in Table 4.2) is indicated in the van't Hoff plot in Figure 4.20. The oxygen partial pressure used in the quenching studies reported herein (250 ppm) is indicated by the solid horizontal line in the figure. Reaction 1 is the eutectic melting reaction. At conditions above and to the right of the associated line in Figure 4.20, liquid is not stable in contact with 213. The liquid formed by reaction 1 again becomes unstable at lower $P(\text{O}_2)$'s and temperatures, and solidifies through reaction 6. The eutectic liquid is stable, therefore, to temperatures no lower than ~810°C and $P(\text{O}_2)$'s no less than ~2000 ppm. This indicates that the heat treatment conditions used in the quenching experiments, as well as those used to synthesize the highest J_c films described in Chapter 3, were not consistent with the presence of the eutectic liquid in the Ba-Y-Cu-O system. The presence of BaF_2 in the film, prior to its decomposition through reaction with water vapor, may, however, act to depress the range

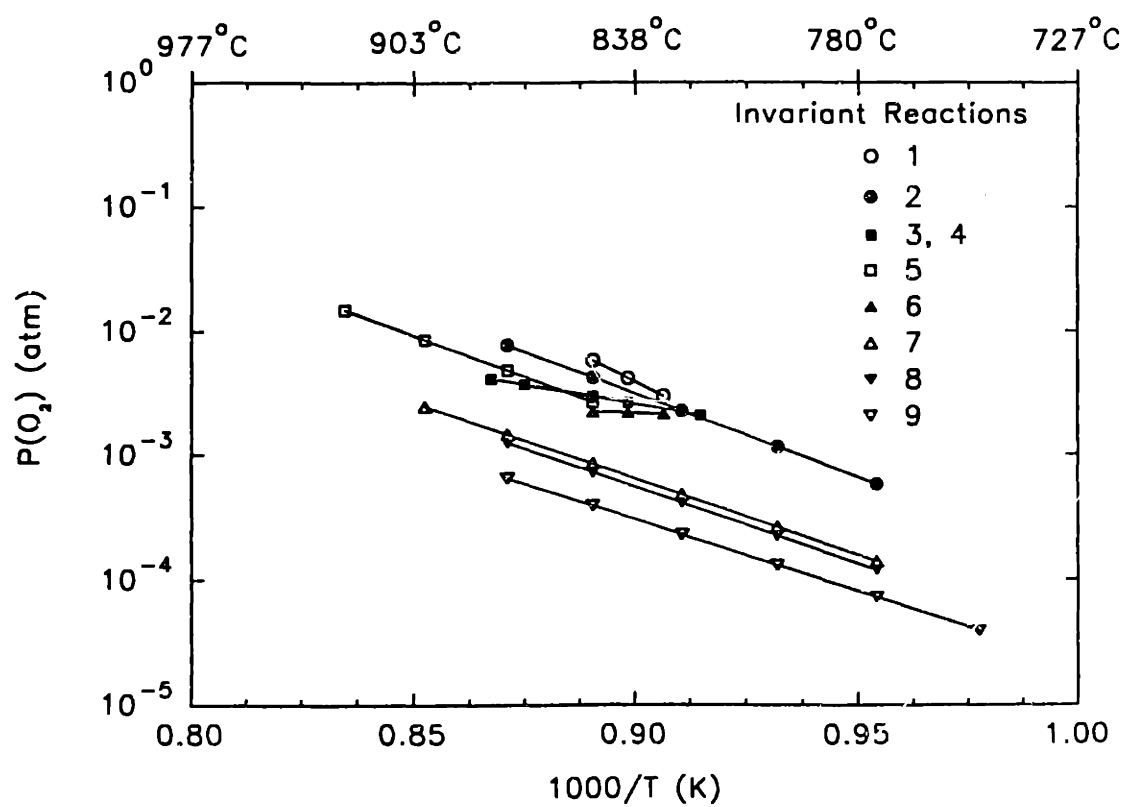


Figure 4.20 Van't Hoff plot showing the temperature/ $P(\text{O}_2)$ dependence of the invariant reactions near $\text{Ba}_2\text{YCu}_3\text{O}_{7-x}$ at subatmospheric oxygen partial pressures (see Table 4.2).

of temperatures and $P(O_2)$'s over which the melt is stable.

Differential thermal analysis experiments were undertaken to test for the possible existence of a liquid phase in the TFA-derived films under the annealing conditions used to synthesize the best BYC thin films. An analyzed ultrahigh purity nitrogen/oxygen gas mixture with 270 ppm oxygen was humidified by bubbling through distilled water and was injected into the DTA chamber. The $P(O_2)$ was confirmed with a ZrO_2 oxygen sensor. The DTA furnace was heated at $20^\circ\text{C}/\text{min}$ from room temperature to $\sim 400^\circ\text{C}$ and from $\sim 400^\circ\text{C}$ to 1000°C at $2^\circ\text{C}/\text{min}$. Differential thermal analysis of both the oxygen- and fluorine-containing intermediate powder sample and the mixed $BaF_2/Y_2O_3/CuO$ crystalline powder sample detected an endothermic event at $\sim 715^\circ\text{C}$. In most of the DTA runs this event was a downward inflection in the DT baseline, although in one run with a sample of the mixed crystalline powder a shallow endothermic peak in the baseline was detected. The simultaneous TGA traces did not indicate a weight loss associated with the endothermic event. Weight loss from the samples was not observed until approximately 750°C , and this was consistent with reduction of CuO to Cu_2O at the $P(O_2)$ used in the experiments.

The behavior of the samples in the DTA/TGA experiments is consistent with the occurrence of partial melting near 715°C in a N_2/O_2 atmosphere containing ~ 250 ppm oxygen. A liquid assisted growth mechanism similar to the one described by Morgan et al.¹³² for growth of the BSCCO-2223 compound may also occur in these *ex situ*-derived BYC thin films. If this is the case, increasing the temperature and reducing the oxygen pressure used in the growth anneal would reduce the surface tension of the copper-containing liquid and improve the density and uniformity of the microstructure, as was noted in Chapter 3. The temperature of the endothermic event detected in the DTA experiments is slightly less than the lowest annealing temperature investigated in the study of heat treatment variables described in Chapter 3. The sample annealed in the $720^\circ\text{C}/250$ ppm O_2 condition had a relatively porous and granular microstructure (Fig. 3.12a) and its superconducting properties were somewhat degraded from those of the

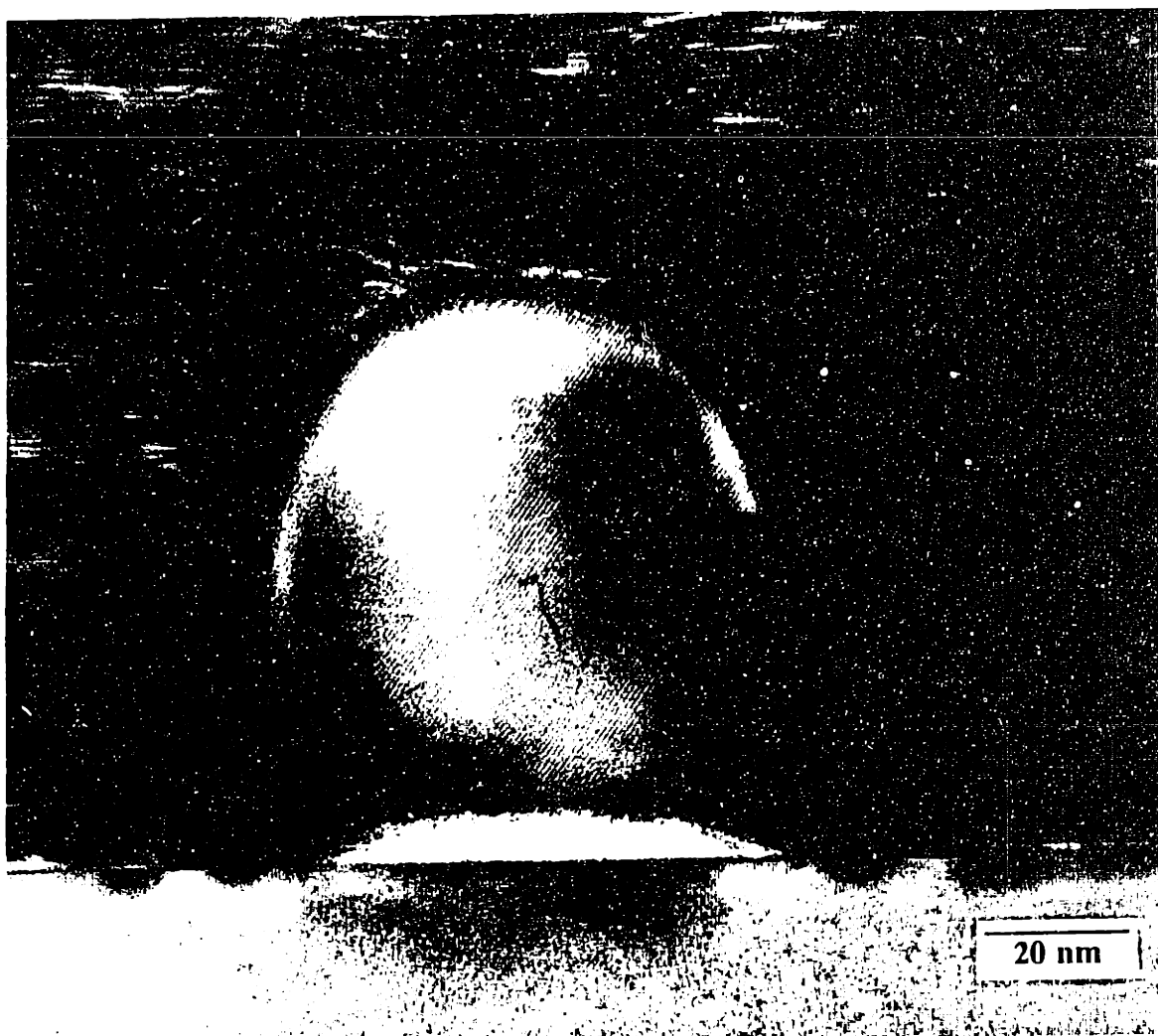


Figure 4.21 Cross-sectional TEM micrograph of a crystalline inclusion, tentatively identified as $\text{Y}_2\text{Cu}_2\text{O}_5$, and fluorine-containing amorphous region at the substrate surface.

films annealed at higher temperatures. The degradation in properties may be related to the reduced connectivity of the film due to increased surface tension of the liquid.

Evidence for the existence of a fluorine-containing liquid during the high temperature anneal was recently discovered during cross-sectional TEM and STEM characterization of a TFA-derived BYC film of approximately 350 nm thickness. The bright field image in Figure 4.21 shows c-axis normal BYC surrounding a crystalline second-phase particle located near the LaAlO_3 surface. X-ray elemental analysis of the particle by EDS in STEM detected only yttrium, copper, and oxygen. The particle, therefore, is believed to be $\text{Y}_2\text{Cu}_2\text{O}_5$. Analysis of the amorphous material that separates the particle from the substrate surface (marked by an arrow in Fig. 4.21) detected yttrium, copper, and oxygen as well as much weaker barium and fluorine signals. The yttrium to copper ratio was higher in the amorphous material than in the particle, based on the measured X-ray intensities, suggesting that detection of these elements was not due to proximity to the particle. This is the only region in a fully-annealed BYC film in which fluorine has been detected by EDS. The appearance of the amorphous region suggests that a small amount of a wetting liquid phase was trapped between the particle and substrate when the advancing growth front of the BYC impinged on the particle. This would have capped-off the liquid, preventing contact with the humidified furnace atmosphere and removal of the fluorine through reaction with water vapor. The small pocket of liquid appears to have remained stationary throughout the hold at 830°C and solidified as an amorphous region during cooling to room temperature. The presence of this region in the fully-annealed film in Figure 4.21 is consistent with BYC growth assisted by partial melting of the TFA-derived films due to the presence of fluorine.

A TFA-derived BYC film of 70-80 nm thickness on (001) LaAlO_3 was synthesized by annealing at 700°C in 250 ppm oxygen, below the temperature at which the endothermic event was observed in the DTA experiments. It was found necessary to anneal the sample for 2 h in the humidified furnace atmosphere in order to decompose BaF_2 at this lower heat treatment temperature. X-ray diffraction scans of the film

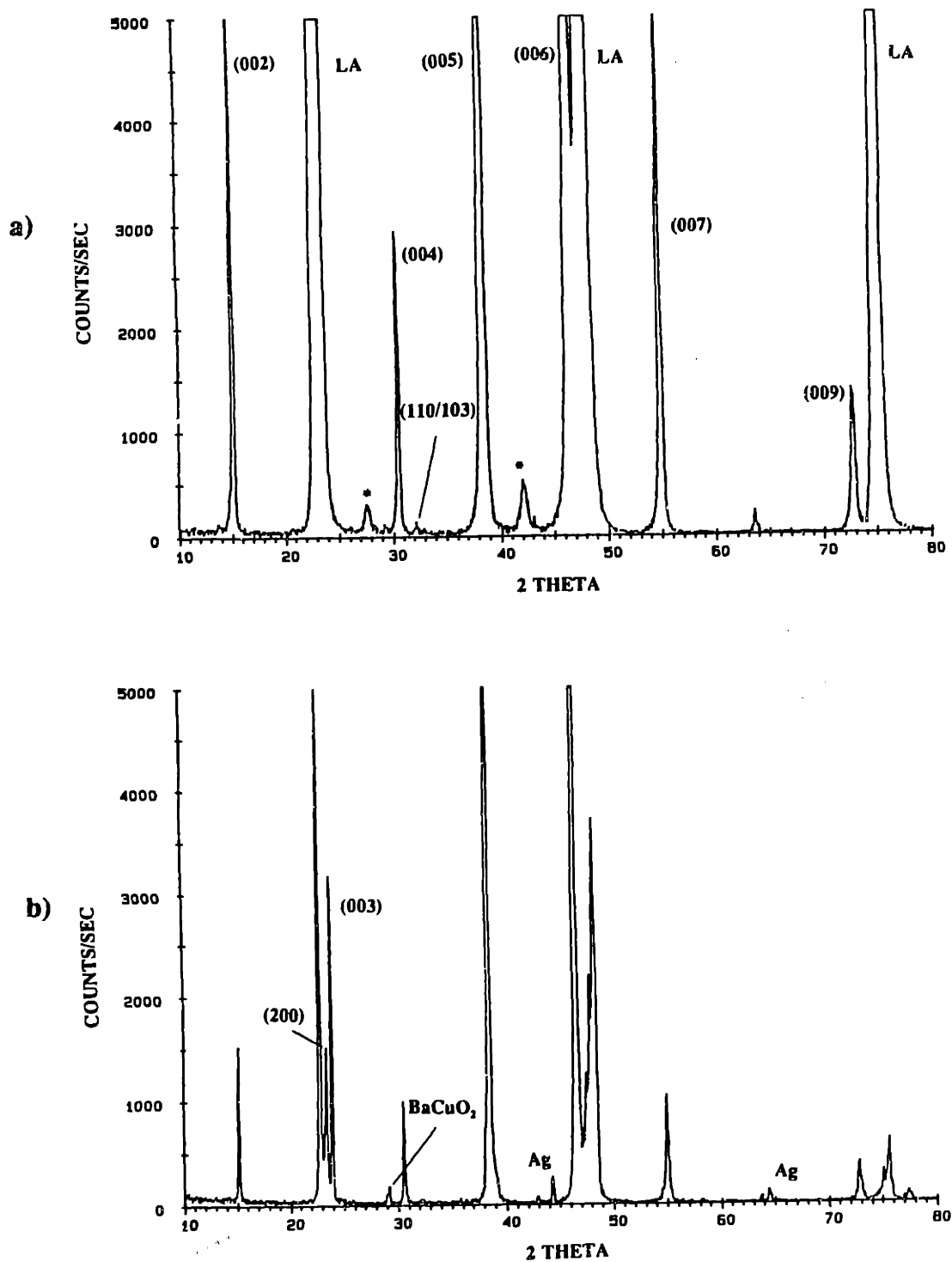


Figure 4.22 X-ray diffraction scans of TFA-derived films annealed in a humidified O_2/N_2 gas mixture containing 250 ppm oxygen at a) 700°C for 2 h and b) 830°C for 1 h.

annealed at 700°C and of a sample annealed at 830°C for 70 min in 250 ppm oxygen are presented in Figures 4.22a and 4.22b, respectively. Both specimens have sharp (00 l) BYC reflections and weak reflections near $2\theta=29^\circ$ which have been tentatively assigned to BaCuO₂. The intensities of the (00 l) BYC reflections and of reflections from the LaAlO₃ substrate were weak in the 830°C sample due to a slight misorientation of the specimen in the diffractometer. The weak (001) LaAlO₃ peak makes the normally obscured (200) BYC reflection visible in Figure 4.22b (see Section 3.3). Peaks due to silver electrodes are also present in the scan from the sample annealed at 830°C, which was tested for T_c and J_c prior to XRD characterization. The film annealed at 700°C contained an unknown phase that was apparently responsible for the fairly broad peaks detected near the 2θ angles 27.7° and 42.2°. This specimen also contained a measureable quantity of BYC with (110) and/or (103) orientation, the strongest X-ray reflections in randomly-oriented polycrystalline BYC samples. The (005) BYC reflection of the 700°C film had, however, a relatively narrow theta rocking curve with FWHM of $\sim 0.6^\circ$ (compared to $\sim 0.4^\circ$ for the 830°C sample).

The microstructure of the TFA-derived film annealed at 700°C was extremely rough (see Fig. 4.23). Flat, plate-like c-axis normal grains are not present in the film, which appears to be discontinuous in some areas. Numerous, small (~ 100 nm diameter) rounded grains and a high density of small c_1 crystallites are present in the film. The transport critical current density of the 700°C film was considerably lower than that of samples annealed at higher temperatures in the same furnace atmosphere. The J_c at 77 K in the absence of an applied magnetic field was 1.3×10^6 A/cm². The room temperature resistivity of the film was 1000 μ A-cm and the ratio of the resistivity at 300 K to that at 100 K was 2.65, compared to values of < 300 μ A-cm and > 3.5 typically measured in TFA-derived films of similar thickness annealed at 830°C. The zero-resistance T_c was, however, measured at 93 K. These results indicate that superconducting BYC with relatively good crystalline quality can be prepared from TFA precursors by annealing at the low temperature of 700°C. However, the poor connectivity and roughness of the resulting film degraded its transport properties and would limit its usefulness in

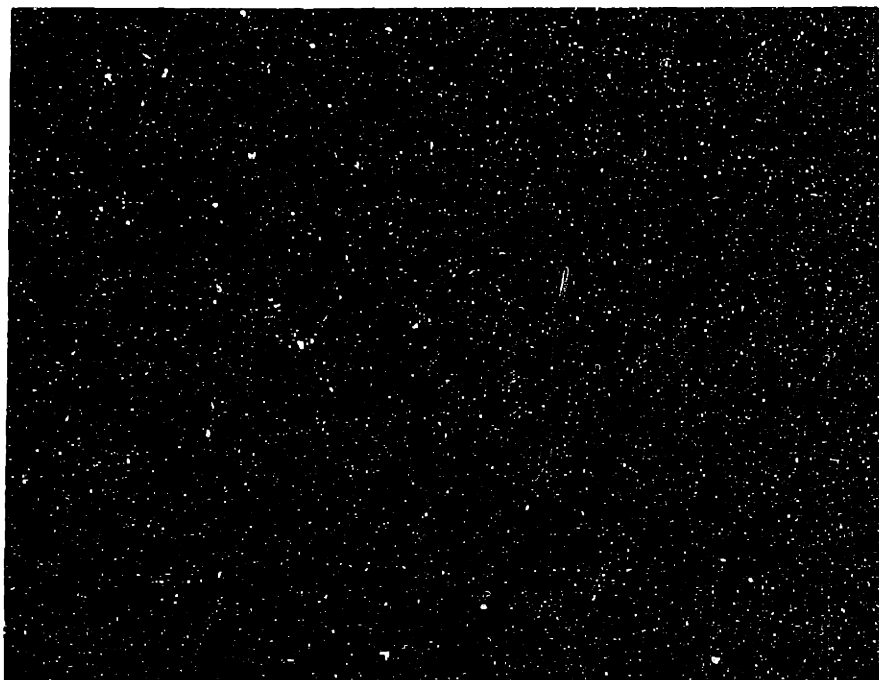


Figure 4.23 Scanning electron photomicrograph of the film annealed at 700°C.

applications requiring smooth surfaces for preparation of multilayer devices. The low density and very small grain size apparent from the micrograph in Figure 4.23 is consistent with the absence of a liquid phase that is present above 715°C and enhances the transformation and densification kinetics at higher temperatures.

4.4 SUMMARY

Nucleation in both *ex situ* chemically derived and *in situ* pulsed laser deposited $\text{Ba}_2\text{YCu}_3\text{O}_{7-x}$ thin films on (001) LaAlO_3 was investigated by studying the microstructures of films deposited on topographically complex substrate surfaces. High resolution cross-sectional TEM indicated that large steps in the LaAlO_3 substrates act as preferred sites for nucleation of BYC crystallites with c-axis in-plane orientation. The size of these c_1 domains was dramatically different in films synthesized by the two techniques. The TFA-derived typically formed relatively large, well-defined c_1 outgrowths at substrate steps, whereas PLD-derived films contained smaller c_1 domains that formed regions of two-fold c-axis orientation on the artificially stepped substrates. The difference in nuclei density on the slopes of the stepped substrates implies that the ratio of growth rate to nucleate rate (G/I) is significantly larger in the TFA-derived studied than in the PLD-derived films. It should be noted, however, that both G and I are strong functions of temperature, oxygen pressure, and (in PLD) deposition rate. Thus the G/I ratios for the two BYC film synthesis techniques will vary depending upon the processing conditions. The results in Section 4.2 also suggest large native steps may form on portions of the (001) LaAlO_3 surface due to detwinning of the substrates above room temperature. These native steps are believed to be effective sites for nucleation of c_1 grains in the TFA-derived BYC films.

The epitaxial growth process in the TFA-derived films was studied by characterizing the chemistry and microstructure of films quenched from the growth heat treatment. X-ray diffraction and TEM results indicated the BYC nucleates heterogeneously at the substrate surface at a temperature between 720 and 770°C in the

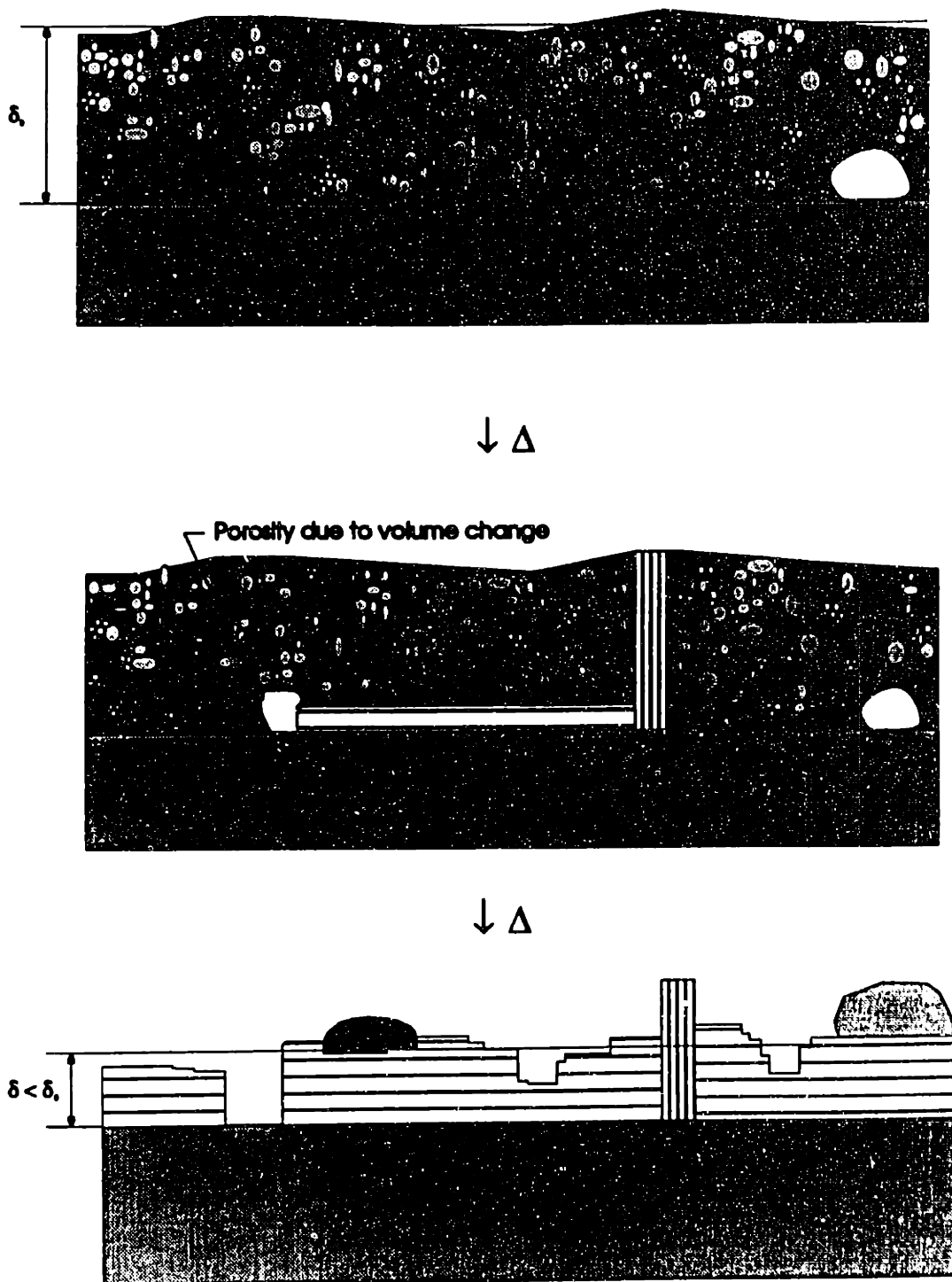


Figure 4.24 Schematic representation of intermediate film-BYC transformation process.

ramp portion of the growth heat treatment. The high heating rate used in this segment of the heat treatment causes BYC nucleation to be delayed to higher temperatures than would be observed in an isothermal experiment. Prior to nucleation of the BYC, the film is relatively dense and polycrystalline, with BaCuO_2 , BaF_2 , and CuO detected by X-ray diffraction. The small, enclosed pores observed near the film/substrate interface of the sample quenched from 720°C are insufficient to account for the porosity observed in the final films. The BYC forms from intermediate phases of lower density; therefore, the volume change on transformation is likely responsible for most of the porosity in the fully-transformed films. Following nucleation, coalescence of c-axis normal BYC crystallites into a continuous film occurs rapidly, with full coverage of the substrate surface achieved at a temperatures below 770°C in the ramp segment of the heat treatment. Upward growth of the c_\perp BYC occurs much more slowly into a polyphase overlayer that, after quenching, contains yttrium- and copper-rich particles in a Ba-rich nanocrystalline matrix. The process of microstructural evolution in the TFA-derived films is summarized in the schematic illustration in Figure 4.24. Results of DTA/TGA experiments suggest the rate of lateral growth of the TFA-derived films may be enhanced by the transient presence of a liquid phase that dissolves the intermediate compounds and precipitates BYC. The presence of a wetting, copper containing liquid would also account for the effects of annealing temperature and $\text{P}(\text{O}_2)$ on film density, as discussed in Chapter 3. X-ray elemental analysis of an amorphous region in a fully-annealed BYC film indicates that the melt may be stabilized by the presence of fluorine in the intermediate films, prior to its removal through reaction with water vapor in the humidified furnace atmosphere.

CHAPTER 5

MICROSTRUCTURAL DEFECTS IN CHEMICALLY DERIVED BYC FILMS

5.1 INTRODUCTION

Numerous studies of BYC epitaxial films, single crystals, bicrystals, and bulk polycrystalline samples have clarified several aspects of current transport in this material. The layered cuprate compounds are anisotropic superconductors. The anisotropic intrinsic superconducting properties of BYC, such as the magnetic penetration depth (λ), superconducting coherence length (ξ), zero field J_c at 77 K, and H_{c2} , are presented in Table 5.1. High current densities can be carried only in the a-b plane of the orthorhombic structure; thus, control of the c-axis orientation in BYC superconducting devices is essential. Moreover, the short coherence lengths can cause the superconducting electrons to uncouple across grain boundaries in BYC. Dimos et al.¹²⁵ examined intergranular current transport in heteroepitaxial BYC thin films on SrTiO₃ bicrystals fabricated with [001] tilt boundaries, [100] tilt boundaries, and [100] twist boundaries. They concluded that all grain boundaries with misorientation greater than approximately 5° act as intrinsic Josephson junctions. The discovery of certain special high angle grain boundaries in BYC that do not exhibit weak link behavior¹³³ has modified this picture somewhat. It is generally recognized, however, that achieving high critical current densities in BYC devices requires both preferred c-axis orientation, and the avoidance of high angle grain boundaries that act as weak links.

The fact that significantly higher current densities can be carried by epitaxial BYC

thin films than in single crystals is generally attributed to the presence of structural defects in the films that act as flux pinning sites. These defects are believed to arise because of the particular growth conditions used in preparing the films. It has been possible to enhance the critical current densities of BYC single crystals through neutron and proton irradiation^{134, 135}; however, the resulting J_c 's are still somewhat less than those of the best epitaxial thin films. Irradiation of BYC films has been shown to have little effect on their transport J_c ¹³⁶, suggesting that a pinning limit may have been achieved in the films.

Clearly, characterization of the microstructural defects present in the TFA-derived films is of interest because of their potential effects on superconducting transport properties. In addition, extraneous defects such as second-phase surface particles are significant from the point of view of applications because they may introduce defects into multilayer devices fabricated using the films. Experiments that provide a more detailed picture of the various microstructural defects present in the TFA-derived BYC films are described in this chapter. Section 5.3 focusses on morphological defects in the films. These include pin holes and high angle grain boundaries which may disrupt the continuity of the superconducting properties of the films. The origin of the second phase surface particles that were reported in Chapter 3 is also described in this section. Extended crystallographic defects within the c-axis normal films, such as stacking faults and antiphase boundaries, are discussed in Section 5.4. These defects may enhance flux vortex pinning in the superconducting films, and thus improve the critical current density. The spatial distribution of these defects within the TFA-derived films and *in situ* PLD-derived is discussed.

5.2 EXPERIMENTAL PROCEDURE

Chemically derived BYC films on nominally flat (001) LaAlO_3 were prepared using the methods described in Section 3.2 of this thesis. The "standard" high temperature heat treatment, which includes a 1 h anneal at 830°C in a humidified N_2/O_2

atmosphere containing 250 ppm oxygen, was used to grow the films. The *in situ* pulsed laser deposited film characterized in Section 5.4 was synthesized by J.Z. Sun at International Business Machines Corp. using the deposition conditions described in Section 4.2.2 of this thesis. Thin film microstructure was characterized by plan-view field emission scanning electron microscopy (Jeol 840 SEM) and by cross-sectional and plan-view TEM (Akashi EM002B and Jeol 200CX) at 200 kV. Electron transparent specimens of the chemically derived BYC thin films were prepared through the multi-step process of sectioning, mechanical polishing, dimpling, and ion milling that was outlined in Section 4.2.2. The micro-chemistry of the surface particles on these *ex situ* films was characterized by EDS in STEM (Vacuum Generators, VG HB5). Scanning tunneling microscopy was performed using by A. Roshko of NIST using a bias of 700 mV and a maximum tunneling current of 490 pA on TFA-derived films of 70-80 nm thickness.

5.3 MORPHOLOGICAL DEFECTS

Several different types of morphological defects are commonly observed in the TFA-derived BYC thin films. These defects are indicated in the field emission SEM image in Figure 5.1. This plan-view micrograph of a TFA-derived film of 70-80 nm nominal thickness contains several second phase particles, a c_1 outgrowth, and a faceted pinhole. With the exception of the latter feature, these defects are frequently observed on BYC thin films produced by a variety of different *in situ* and *ex situ* techniques. Nucleation of the c_1 grains in the TFA-derived films has been discussed in detail in Chapter 4, and appears to be facilitated by the presence of steps on the (001) LaAlO_3 surface. The second phase particles may form because of incorrect overall stoichiometry in the film, contamination in the deposition or post-deposition environment, or due to the nature of the film growth process itself. Faceted pin holes with diameters of 100-200 nm, similar to the one shown in Figure 5.1, are present in the BYC films of 70-80 nm thickness derived from the MOD process. Based on the orientation of the nearby c_1 grain, the pin hole in Figure 5.1 can be seen to be faceted on the (100), (010), and {110}-type planes. Faceting on the non-equilibrium {110}-type BYC planes was commonly

Table 5.1: Superconducting properties and anisotropy of $\text{Ba}_2\text{YCu}_3\text{O}_{7-x}$

| | Parallel to c | In a - b plane |
|---------------------------------|-----------------|--------------------|
| ξ (nm) | 0.3^{35} | 1.5^{35} |
| λ (nm) | 150 | 750 |
| J_c (A/cm ²) 77 K | 10^4 | 10^6 |
| H_{c2} (T) | 150 | 50 |

Data from reference 143 unless otherwise indicated.

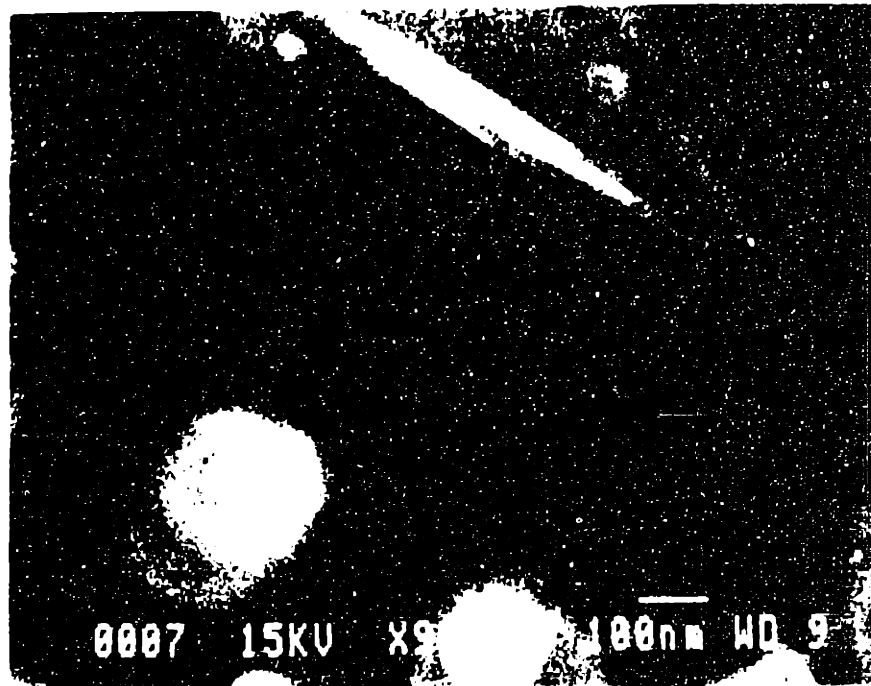


Figure 5.1 Field emission SEM image taken at 15 kV of a TFA-derived BYC film of 70-80 nm thickness annealed at 830°C in 250 ppm oxygen.

observed in the defects. The pin holes are believed to result, in large part, from the density change that occurs on transformation of the polyphase intermediate film to BYC, as discussed in Section 4.3. Pin holes have been observed in BYC films produced by other *ex-situ* processes in which BaF_2 is an intermediate material.^{79, 91}

The plan-view TEM micrograph of an MOD-derived thin film in Figure 5.2 indicates the larger lattice spacing of a c_1 grain relative to the surrounding c-axis normal film (~ 1.17 nm vs. ~ 0.38 nm). The $\{110\}$ -type twinning in the BYC film is also evident. The higher magnification lattice image in Figure 5.3 shows a film region in which two c_1 crystallites 90° -misoriented with respect to one-another have impinged. Stacking faults and anti-phase boundaries are present in the c_1 grains, as was indicated in the cross-section micrographs in Section 4.2.3. An antiphase boundary (APB) in the longer of the two c_1 crystallites in Figure 5.3 is marked by an open arrow. Filled arrows indicate the locations of polytypoidal stacking faults in this grain. The grain boundary separating the two crystallites has both 90° twist and basal-plane-fronted facets.¹¹⁸ The interface between the c_1 grains and the surrounding c-axis normal film is apparently free of any second phases. Several reports have suggested that the weak link characteristics of many high angle grain boundaries in BYC may be related to the presence of impurity segregation or variations in stoichiometry near the boundaries.¹³⁷⁻¹³⁹ Chisholm and Pennycock¹⁴⁰, however, found no evidence of chemical segregation by using Z-contrast STEM to form chemically sensitive high resolution images of several high angle boundaries. These results suggest that weak link behavior of BYC grain boundaries may instead be caused by the strain field associated with grain boundary dislocations. The same authors presented a simple model based on this hypothesis that agreed quite well with the experimental data of Dimos et al.¹²⁵ for J_c versus grain boundary misorientation angle in BYC bicrystals.

Surface particles have been observed on BYC thin films prepared by both *in situ* and *ex situ* growth techniques. Deviations in overall film stoichiometry from the 2:1:3 cation ratio have been shown to produce second phase particles on the films.^{141, 142} A

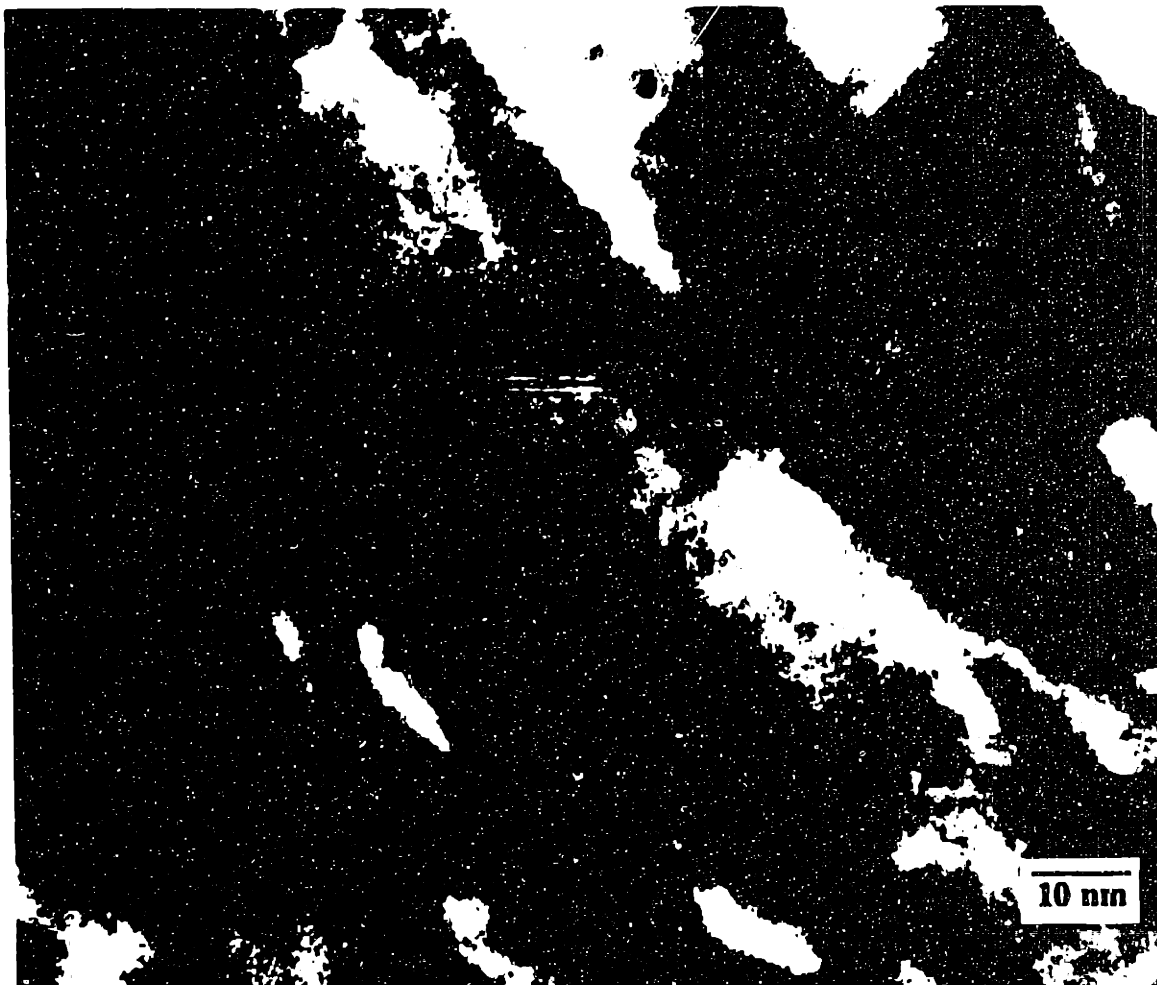


Figure 5.2 Plan view bright field TEM micrograph of a BYC film in a region containing a c_1 grain.



Figure 5.3 Higher magnification TEM bright field image near the [001] zone axis of the c_2 material surrounding two c_1 grains.

deviation in overall cation stoichiometry is probably not responsible for the particles that decorate the surfaces of the TFA-derived BYC films. The reagent grade metal acetate powders used to prepare the TFA precursor solution were characterized by TGA and chemical analysis for metals, carbon, and hydrogen prior to use. Gram quantities of the powders were weighed out using an analytical balance that is accurate to 0.1 mg. The metal TFA solution was stable to precipitation and there was no evidence of volatilization of any of the components from the films during the heat treatments. Therefore, the overall Ba:Y:Cu ratio in the films is believed to be very close to 2:1:3.

The surface particles have been observed to cover a larger fraction of the film surface as the high temperature annealing time and temperature are increased, suggesting that they may be produced by a reaction with contaminants in the furnace environment at elevated temperatures. This was also suggested by the results of several experiments in which identically-prepared intermediate films were placed in-line in the high temperature furnace - one upstream of the other. In all cases, the upstream films were found to have a much higher density of the 0.5-1.0 μm surface particles that are visible by optical microscopy.

Micro-chemical analyses of the second phase particles on chemically derived BYC films were performed by EDS in STEM on both cross-section and plan-view specimens. A cross-sectional TEM image of one of the small (~ 100 nm diameter) particles present in Figure 5.1 is shown in Figure 5.4. The crystalline particle is an approximately spherical caplet that is supported by a relatively smooth island of BYC film. The associated EDS spectra for the BYC film interior and the surface particle indicated the particle had very high yttrium and copper signals, and essentially background levels of barium. Similar spectra were obtained for numerous other rounded surface features of similar size. The particles were tentatively identified as $\text{Y}_2\text{Cu}_2\text{O}_5$.

Analyses of the larger second phase particles were performed using plan-view specimens because these features did not typically survive the cross-section TEM

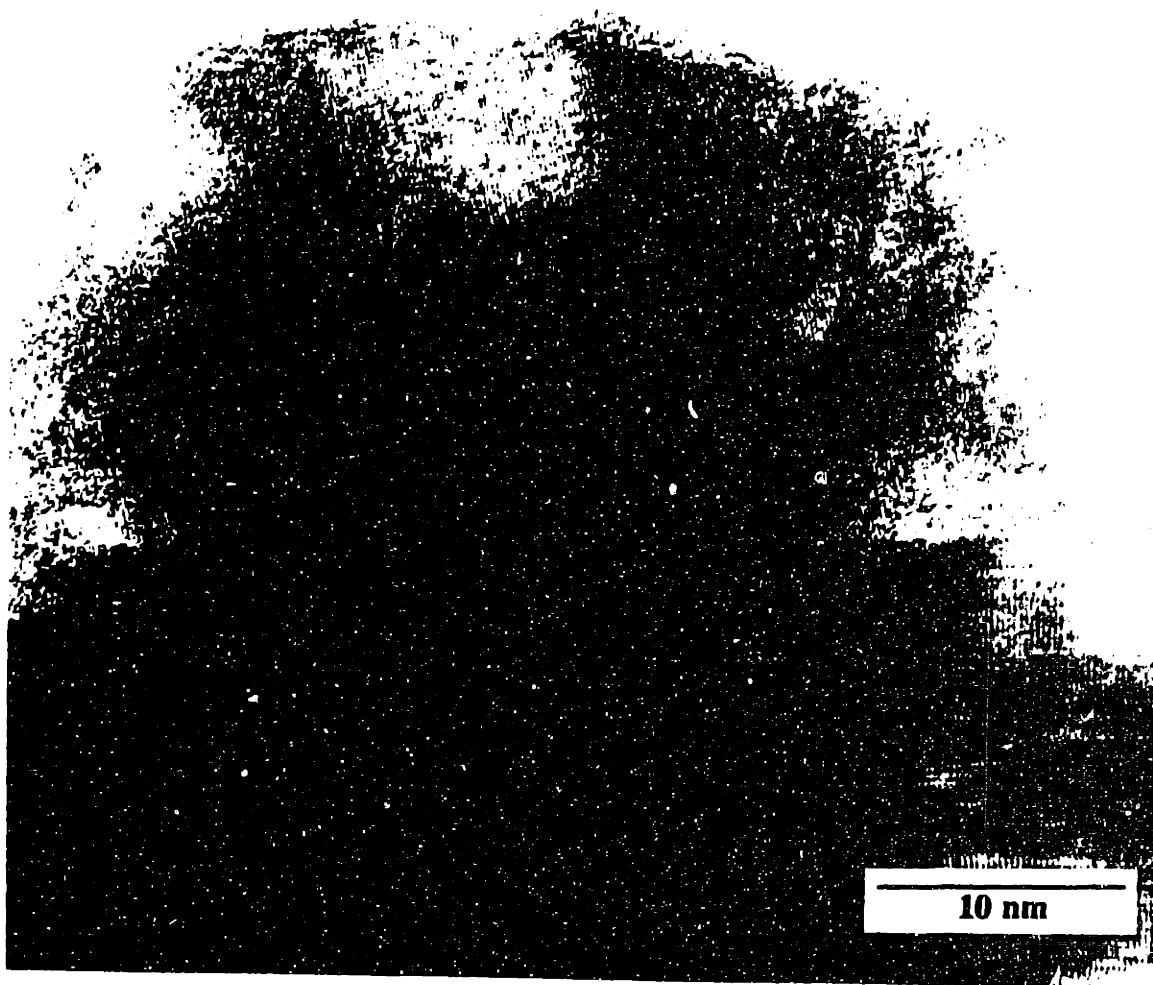


Figure 5.4 Cross-sectional TEM image showing a roughly hemispherical second phase particle that was identified as $\text{Y}_2\text{Cu}_2\text{O}_5$ by EDS.

specimen preparation. A dark field STEM image of plan-view specimen showing both the large ($\sim 1\ \mu\text{m}$ diameter) particles and the smaller rounded particles is shown in Figure 5.5, along with EDS spectra for the BYC film surface, and two different types of particles. The high Ni signals in these spectra are due to sputtering contamination of the nickel aperture disk during ion thinning of the sample. Once again, similar spectra were obtained for a number of the large second phase particles. Two chemically distinct species of particles were observed; one that gave very strong copper and oxygen signals and little or no yttrium and barium signals, and another that gave strong barium, oxygen, and sulphur signals and was apparently denuded of copper and yttrium. They were tentatively identified as CuO and BaSO_4 , respectively. The Ba-rich particles were present in larger numbers than the Cu-rich and were highly faceted, and often grew in the shape of triangular pyramids or prisms on the film surface. The Cu-rich particles tended to be needle-shaped.

Formation of these three particulate defect species ($\text{Y}_2\text{Cu}_2\text{O}_3$, CuO , and BaSO_4) can be ascribed to sulfur contamination during some part of the film fabrication process. The reactivity of barium in these films with chemical species in the growth/deposition environment is a general problem and has been noted in *in situ* sputtered films.⁸ The upstream/downstream experiments indicate that the furnace gas stream is probably supplying the contaminant to the films during the high temperature heat treatment. Mass spectrometry and gas chromatography of the ultrahigh purity gas sources failed to provide any definitive evidence of sulfur-containing gaseous species. Removal of potential sources of sulfur contamination from the high temperature furnace (rubber fittings, hoses, etc.) appeared to reduce the areal density of the particulate defects somewhat. Microchemical characterization of the surface particles that remained on the films after these modifications to the furnace were made, however, indicated that the same three defect species were still present. Short of identifying other, less obvious, sources of sulfur contamination, it is possible the remaining defects may be eliminated by gettering the vapor phase contaminant on a reactive surface upstream of the films in the furnace.

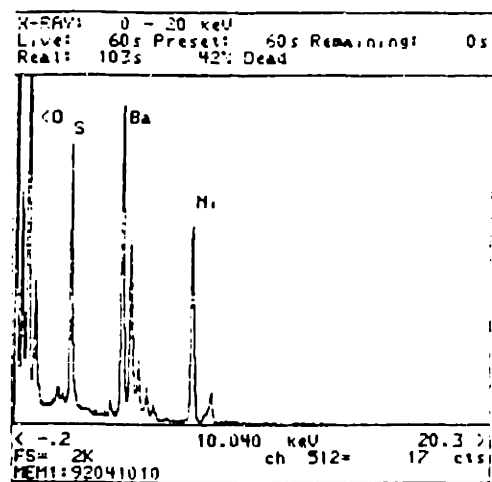
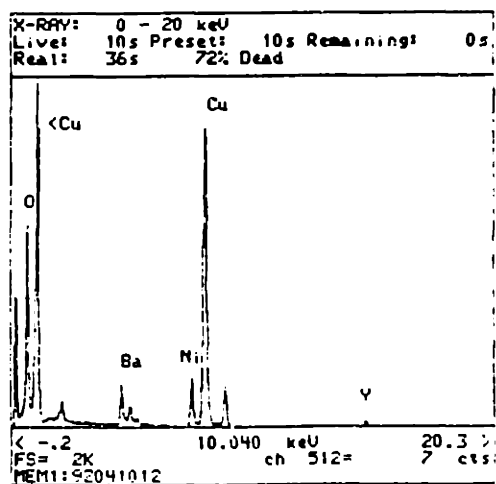
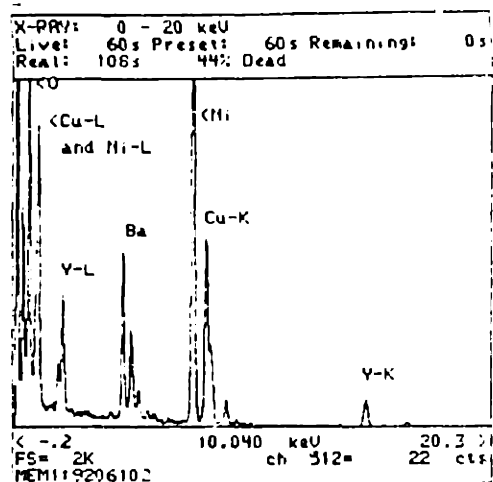
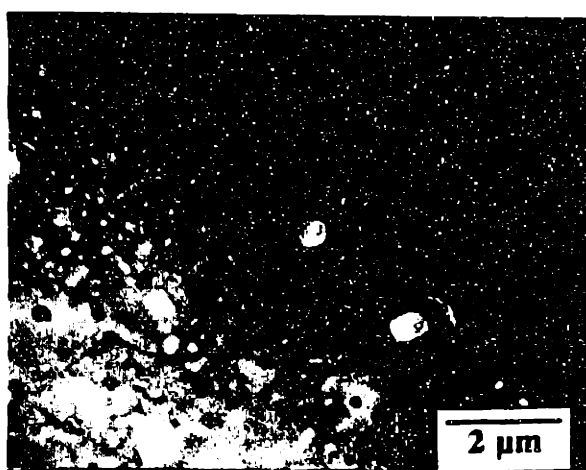


Figure 5.5 Annular dark field STEM image of a chemically derived BYC film of 70-80 nm thickness showing second phase particles, and EDS chemical analyses of b) the BYC film, c) a BaSO_4 surface particle, and d) a CuO particle.

5.4 EXTENDED CRYSTALLOGRAPHIC DEFECTS

5.4.1 Observations

The cross-sectional TEM micrograph in Figure 5.6 shows the structure near the film/substrate interface of a chemically derived BYC film of 70-80 nm thickness. This lattice image, which is representative of cross-sectional images taken of numerous films prepared under similar conditions, indicates the film has a high density of stacking faults. Extended structural defects have been reported frequently in BYC thin films prepared by various growth techniques.^{124, 142, 143} Intergrowths of structurally-related compounds in the Ba-Y-Cu-O system such as $\text{Ba}_2\text{YCu}_4\text{O}_8$, which are metastable under the oxygen pressure and temperature conditions typically employed in BYC film growth, are commonly observed. As noted in Chapter 4, it has been argued that these intergrowths form when the growth velocity in the (001) plane of BYC films deposited from the vapor is too high for surface diffusional processes to maintain correct stoichiometry at the growth front.¹³⁰ Stacking faults related to the $\text{Ba}_2\text{YCu}_4\text{O}_8$ 214 structure can be identified in Figure 5.6 by the occurrence of two adjacent CuO layers (marked by solid arrows), which have bright contrast under the defocusing conditions used to form the image. A 213 unit cell with 1.17 nm lattice parameter is also shown in the figure. Irregularities in stacking have been observed throughout the thickness of the 70-80 nm thick films. This image also shows a 1/2 unit-cell step in the LaAlO_3 surface (open arrow) that altered the stacking sequence in the overlying BYC film, apparently changing the first layer of the film from CuO (right of the arrow) to BaO (left of the arrow).

Figure 5.7 is a cross-sectional micrograph of another region of the film in Figure 5.6, in which stacking faults related to the $\text{Ba}_2\text{Y}_2\text{Cu}_4\text{O}_9$ 224 structure proposed by Ramesh et al.¹²⁴ are evident. These defects are indicated by small open arrows. Intergrowths of the 214 type are also present (marked by solid arrows). The structure of the 214 compound and the proposed structure of 224 are indicated in Figure 5.8. It should be noted that 214-type stacking faults present in these films may be oriented so that the

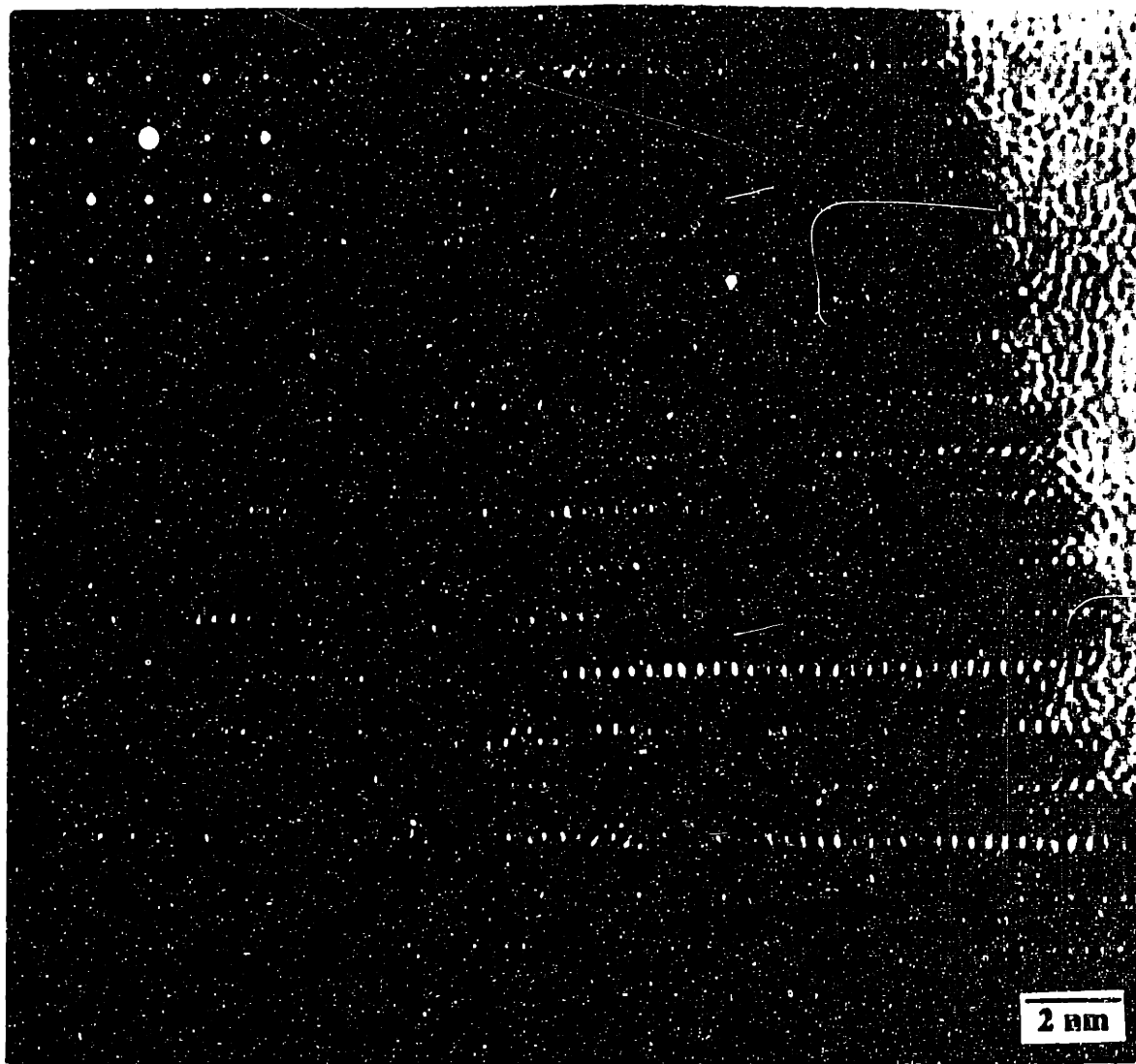


Figure 5.6 Cross-sectional TEM image near the [010] zone axis of a film of 70-80 nm thickness showing the BYC/LaAlO₃ interfacial region.

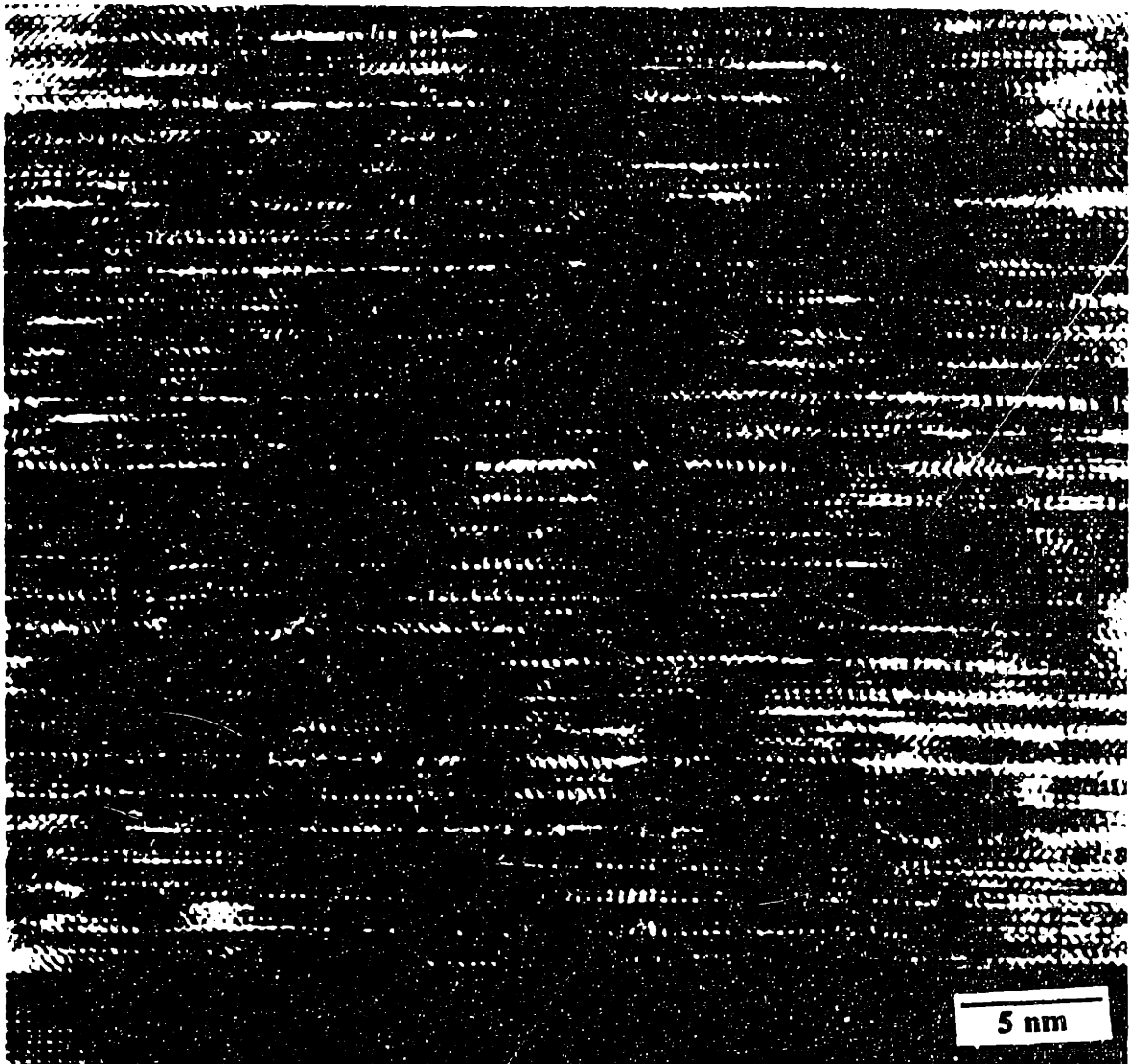


Figure 5.7 Another region of the cross-sectional specimen shown in Fig. 5.6.

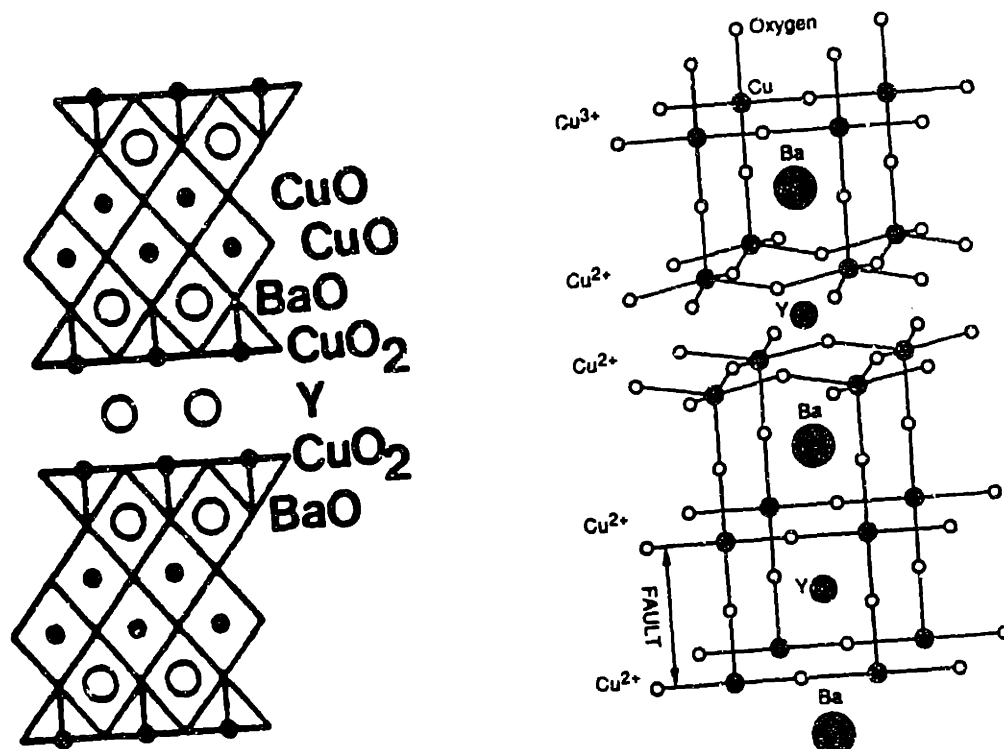


Figure 5.8 Schematic illustrations of the polytype structures to $\text{Ba}_2\text{YCu}_3\text{O}_{7-x}$ (213): a) 214 and b) the proposed structure of 224 (from reference 118).

additional CuO layer is displaced along either the [100] or [010] direction of the film. This is indicated in the high resolution lattice image of a very extensive intergrowth region shown in Figure 5.9. The image, taken on [100] zone axis of the BYC film contains 214 intergrowths of both orientations (labeled in the figure). At only one location in this area is there a "normal" transition between 213 unit cells (without the additional CuO layer), and this is marked by an arrow in the micrograph.

Interfacial steps have been found to cause antiphase boundaries which extend up through much of the film thickness in *in situ* PLD-derived films.³¹ This is shown in the high resolution lattice image in Figure 5.10. The PLD-derived BYC film in this micrograph was deposited at 790°C in a 300 mTorr oxygen ambient onto an artificially stepped LaAlO₃ substrate. The image was taken from the nominally flat trench region of the substrate. In addition to stacking faults along the c-axis of the BYC film (some of which are indicated by open arrows), the region in Figure 5.10 contains two APB's that formed at steps in the (001) LaAlO₃ surface (marked by filled arrows). The substrate surface appears to slope slightly upward from right to left in the figure. The surface step near the center of the image was 2 LaAlO₃ in height; the step near the right of the micrograph was a single unit cell in height. Extended antiphase boundaries are not, however, typically observed in the TFA-derived films. The very high density of stacking fault terminations in the (001) plane of the films appears to interfere with the development of long APB structures in the TFA-derived films.

Cross-sectional TEM images of a chemically derived BYC film of 350 nm nominal thickness in Figures 5.11a and 5.11b show an abrupt transition that occurred from highly faulted BYC near the substrate surface to relatively fault-free 213 in the upper portions of the film. The transition shown in Figure 5.11a was located at ~70 nm above the LaAlO₃ substrate. The density of stacking faults along the c-axis direction of the film was relatively constant in the highly faulted layer and changed discontinuously at the transition height. Figure 5.11b shows a portion of the stacking fault-free material above the faulted layer in Figure 5.11a. Although the situation in Figures 5.11a and 5.11b

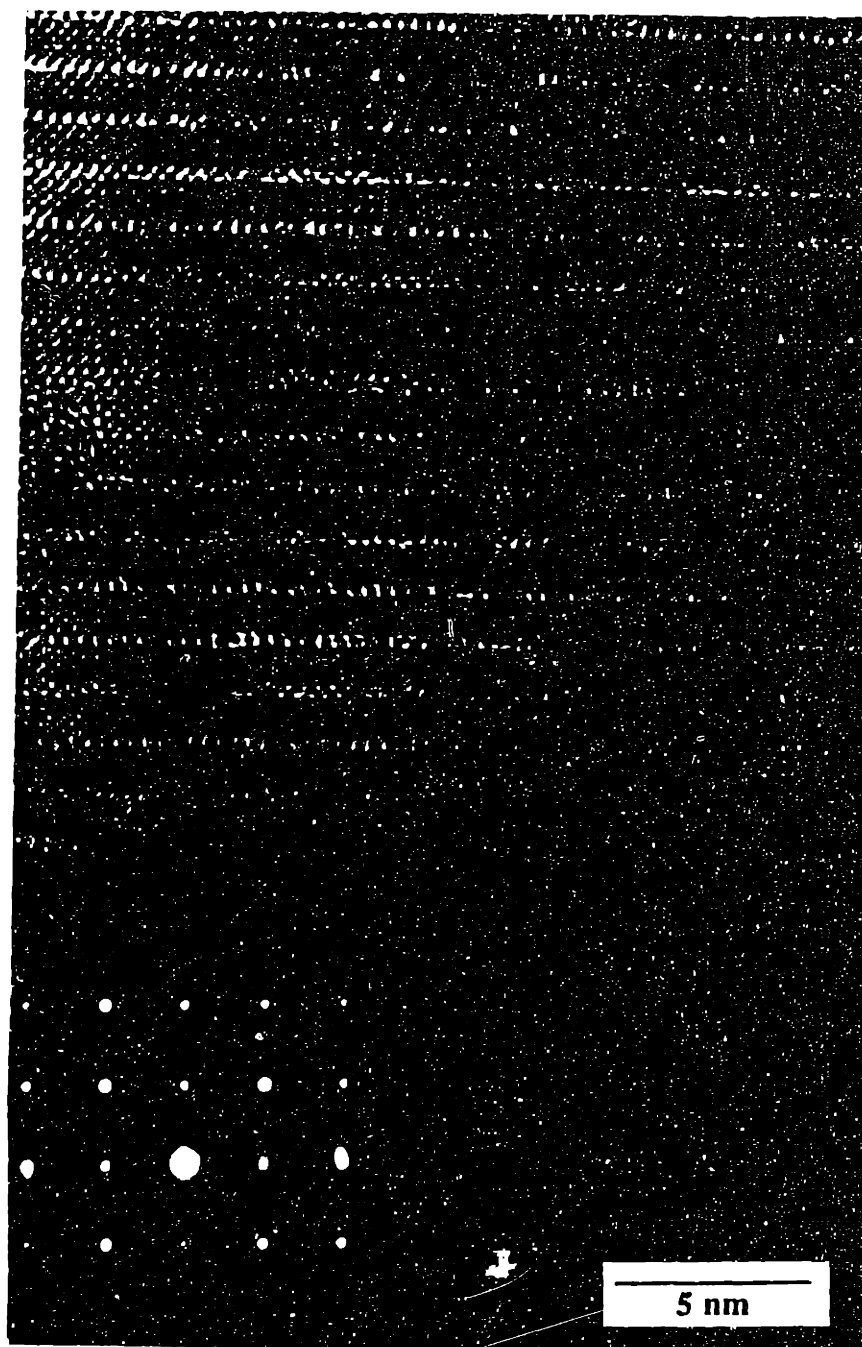


Figure 5.9 High magnification lattice image on the [100] zone axis of a TFA-derived BYC film showing a large intergrowth of the 214-type near the film/substrate interface.



Figure 5.10 Cross-sectional TEM image of the BYC/LaAlO₃ interface of a PLD-derived film.

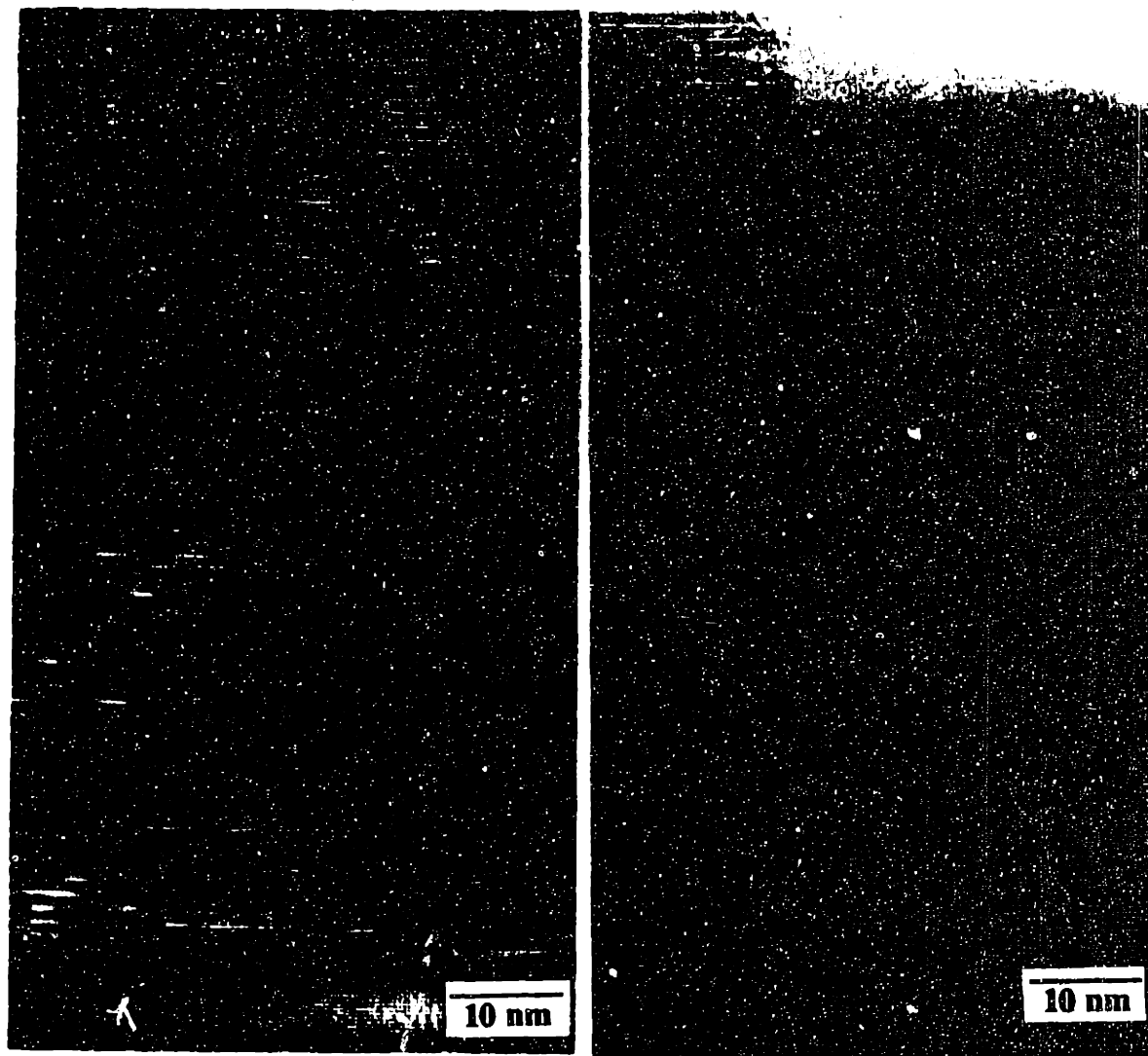


Figure 5.11 Cross-sectional TEM micrographs taken from a TFA-derived film of ~350 nm thickness showing a) the film substrate interface and b) the upper portion of this area of the film.

is particularly dramatic, a decrease in fault density with increasing distance above the BYC/LaAlO₃ interface was observed in several chemically derived films of greater than 200 nm thickness. In some cases, a more gradual variation in intergrowth density with distance above the substrate was found, in which the highly faulted material nearest the interface changed to blocks of relatively fault-free 213 separated by faulted zones higher above the substrate. This situation is shown in the TEM micrograph in Figure 5.12. Cross-sectional TEM studies of the *in situ* PLD-derived films did not indicate any variation in stacking fault density with distance from the substrate surface, nor is this author aware of any reports in the literature of similar inhomogeneities in fault density.

The existence of a significant microstructural inhomogeneity through the thickness of these superconducting films may be related to the previously reported effect of thickness on critical current density. Figure 3.9 in Chapter 3 shows the variation in $J_c(T=77\text{ K}, H_{app}=0)$ with film thickness for chemically derived films prepared under various conditions. A significant decrease in J_c with increasing thickness, independent of synthesis conditions, was measured in the samples described in Chapter 3. The data in Figure 3.9 was used to construct a plot of extrapolated maximum current carried by a line of 1 μm width at 77 K as a function of film thickness. This plot, shown in Figure 3.15, indicates the critical current per micron line width is approximately constant at 4-6 mA over a wide range of BYC film thickness. The reduction in J_c with increasing thickness is consistent with a model in which the majority of the supercurrent is carried by the material nearest the film/substrate interface. The TEM results presented here indicate that this portion of the chemically derived films has the highest density of polytypoidal stacking faults. This suggests that the stacking faults are related to enhancements in J_c , either by contributing directly to flux pinning, or as indicators of other growth related structural defects that increase flux pinning.

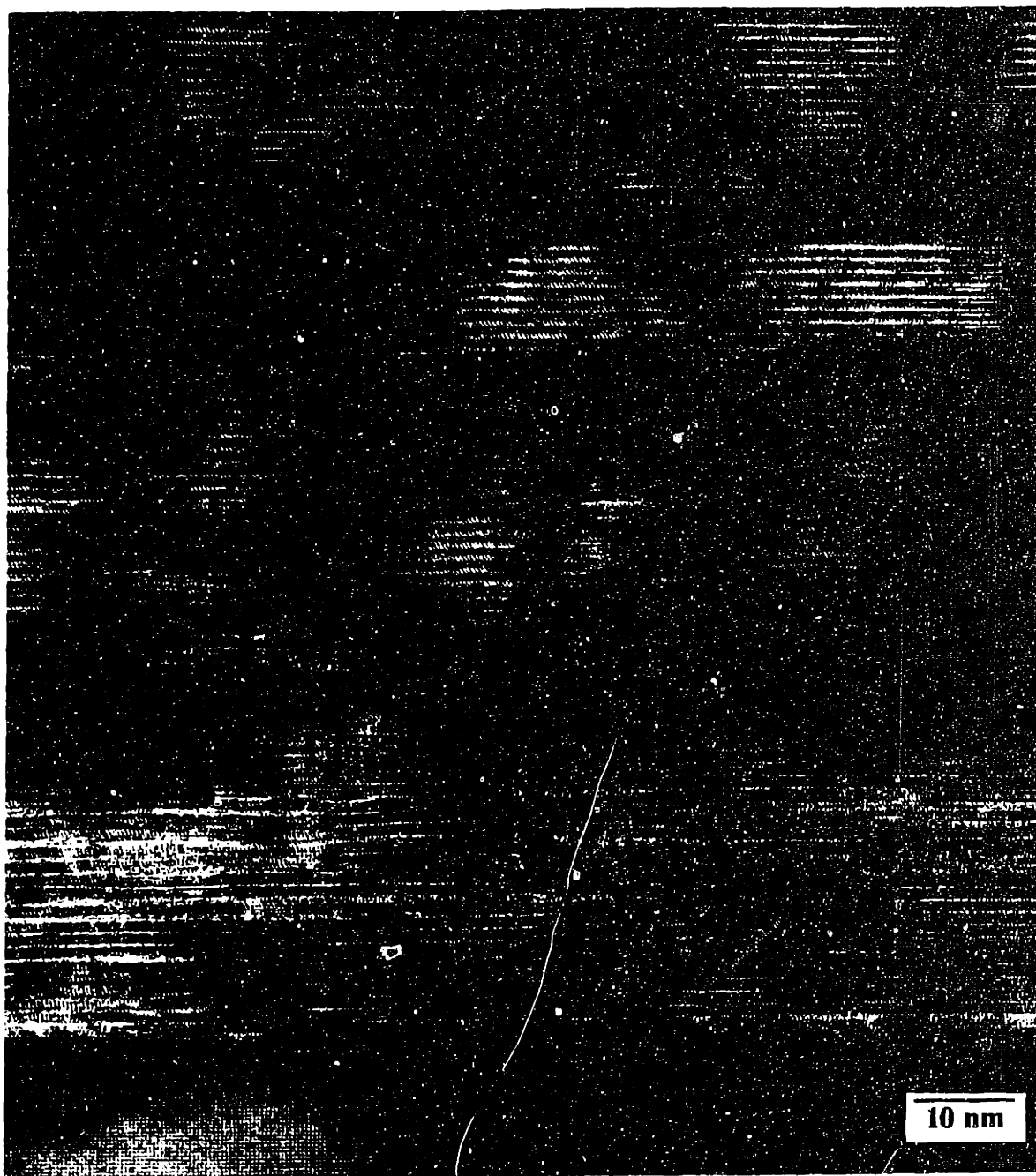


Figure 5.12 Cross-sectional TEM image of a specimen similar to the one in Fig. 5.11 with a more gradual decrease in stacking fault density with distance above the interface.

5.4.2 Discussion

Possible origins of microstructural inhomogeneities

The critical current densities measured in epitaxial BYC thin films are one to two orders of magnitude greater than those of single crystals. It is generally believed that the thin films possess structural defects that act as flux pinning sites, and that the defects arise due to the particular growth conditions used in preparing the films. In *ex situ* synthesis of BYC thin films, the experimental variables that have the greatest effect on the epitaxial quality of the films are annealing temperature and oxygen partial pressure. These variables alter the driving force for the transformation to $\text{Ba}_2\text{YCu}_3\text{O}_{7-x}$ and the BYC growth rate, which ultimately determine the nature of epitaxy and the density of crystallographic defects in the films. The presence of significant microstructural inhomogeneities through the thickness of the films suggest that the film growth conditions are not constant during the transformation process.

Studies of chemically derived BYC thin films rapidly cooled from different points in the high temperature anneal were discussed in Section 4.3 of this thesis, and their results are summarized below. The quenching experiments indicate the BYC nucleates heterogeneously at the substrate surface between 720 and 770°C in the ramp portion of the heat treatment, prior to the 60 min hold at 830°C. Below 720°C, the films are polycrystalline with BaF_2 , CuO , and BaCuO_2 detected by X-ray diffraction analysis of quenched specimens. Upon nucleation of the BYC, the c-axis normal crystallites coalesce rapidly into a continuous film which grows more slowly upward into an overlying, polyphase Ba-Y-Cu-O-F layer. Cross-sectional TEM indicates that essentially full coverage of the (001) LaAlO_3 substrate surface occurs very early in the transformation. The slower rate of upward growth requires an interval of several minutes (in films of 70-80 nm final thickness) for conversion of most of the polycrystalline multiphase film to BYC.

As the transformation to BYC occurs during the ramp portion (25°C/min heating rate) of the heat treatment, the upper part of the film grows at a higher temperature than the initial layers near the substrate surface. This difference in growth temperatures may be responsible for the variation in polytypoidal stacking fault density in the thicker films. A higher local growth temperature would increase both the diffusion rates controlling the arrival of ionic species at the growth front and the rate of attachment to the growing BYC crystal. The relative magnitudes of the activation energies for supplying species to the growth front and attaching them would determine the temperature regime in which stacking defects are liable to form. The process of removal of fluorine from the unconverted material in the film may also contribute to microstructural inhomogeneities through the film thickness. Fluorine is present in BaF₂ in the polycrystalline film prior to transformation to BYC. Differential thermal analysis results (also described in Section 4.3) suggest that the presence of BaF₂ in the precursor film may encourage the transient formation of a small amount of liquid phase by depressing partial melting temperatures in the Ba-Y-Cu-O system. Growth in the basal plane of the BYC thin film is believed to be assisted by the existence of a liquid phase. Decomposition of BaF₂ by reaction with water vapor introduced into the furnace atmosphere occurs during the last few minutes of the ramp to 830°C. If BaF₂ decomposes (to form BaCuO₂, for example) before the transformation to BYC is complete, the film growth mechanism may change from relatively fast, liquid assisted growth to a slower growth mode that is rate-controlled by solid state diffusion. The abrupt change in crystallographic defect density evident in Figures 5.11a and 5.11b may be indicative of such a sudden change in the film growth mechanism.

Neither of these proposed mechanisms for creation of inhomogeneities in polytypoidal stacking fault density are expected to operate in BYC films grown *in situ*. Film deposition with simultaneous growth in PLD or off-axis sputtering takes place on a substrate that is heated to a constant temperature. Although the absolute value of the temperature may be difficult to measure, it should not vary significantly throughout a deposition run. The complex variation in film chemistry that occurs during *ex situ* growth

is also absent from the *in situ* processes; therefore, a sudden change in growth mechanism at a certain point in the run is unlikely.

Implications for flux pinning

Several investigators have attempted to identify the defects responsible for flux pinning in BYC thin films. In an early analysis, based on experimental studies of *in situ* pulsed laser deposited BYC films, Hylton and Beasley¹⁴⁴ argued that a core-type flux pinning mechanism, in which the superconducting order parameter is strongly depressed in the immediate vicinity of the defects, was likely responsible for the observed behavior of the films in low fields. For vortices parallel to the c-axis of the film, the minimum radial distance from a defect in which the order parameter would be suppressed is ξ_{ab} , the coherence length in the a-b plane (~ 1.5 nm). Hylton and Beasley considered the competition between pinning energy and vortex line tension of a flux vortex that meanders through a film, generally parallel to the c-axis. Their calculations suggested a spacing of 4-5 nm in the a-b plane exists between the pinning sites. They concluded that extended crystallographic defects in their films could not account for the high pinning site density because the spacing between these defects was ~ 50 nm, as measured from cross-sectional TEM images. Instead, they argued that point defects in the highly conducting CuO_2 planes of their BYC films were more probable flux pinning sites.

The majority of Hylton and Beasley's analysis is relevant to core-type pinning at any localized crystallographic defects. Their assumption that point defects are the most important defects for pinning at low magnetic induction was largely based on TEM observations showing a low density of "extended defects". Hylton and Beasley did not specify the extended defects to which they were referring; however, TEM results presented in Section 5.4.1 of chemically derived *ex situ* and pulsed laser deposited *in situ* BYC films indicate that lateral spacings of ~ 5 nm between polytypoidal stacking faults (that are required, according to their calculations, by the observed pinning energies) are not unusual.

A more recent paper by McElfresh et al.¹⁴⁵ focused on the possible role of screw dislocations in pinning flux vortices in BYC thin films. As noted in Section 4.1, STM and AFM have revealed that, under certain conditions, BYC films on SrTiO₃ and LaAlO₃ substrates grow via a screw dislocation mechanism.¹⁰⁰⁻¹⁰² The density of spiral growth features observed on the surfaces of *in situ* sputter deposited thin films is $\sim 10^9/\text{cm}^2$.^{100, 101} At the centers of the spirals are screw dislocations that thread up through the film parallel to the c-axis, an orientation that would allow them to pin flux vortices along most of their length. McElfresh et al.¹⁴⁵ argued that, although defect densities of this low magnitude could not be responsible for flux pinning in high magnetic fields, the low field J_c 's could result from either attractive core-type pinning at dislocations or from repulsive dielastic pinning interactions. The latter effect arises because the greater stiffness of the material in the normal state relative to that of superconducting BYC causes a difference in strain energy between structural imperfections located in the vortices and those located in the surrounding superconductor.¹⁴⁶

Screw dislocations may act as flux pinning defects in epitaxial BYC thin films, but it is likely that other types of defects also make significant contributions to pinning at both low and high fields because screw dislocations are not observed in all high- J_c films. Screw dislocation growth occurs in BYC thin films under specific growth conditions. Higher deposition rates (and, thus, higher supersaturations) favor a terraced island growth morphology in films grown *in situ* from the vapor (see Section 4.1 of this thesis). Preliminary STM examination of chemically derived BYC films of 70-80 nm thickness indicates they have the terraced island morphology. An STM image showing the island surface structure of a TFA-derived BYC film of 70-80 nm thickness is shown in Figure 5.13. The image quality was not optimal due to charging; however, the terrace height was estimated to be one c-axis unit cell spacing.¹⁰⁶ The growth spiral morphology was not observed on the sample. The apparent absence of screw dislocations in these films, which have both higher zero field J_c 's and higher critical fields⁸² than the *in situ* films studied by McElfresh and coworkers¹⁴⁵, suggests that growth related screw dislocations are not dominant flux vortex pinning sites in all BYC thin films. Instead, the

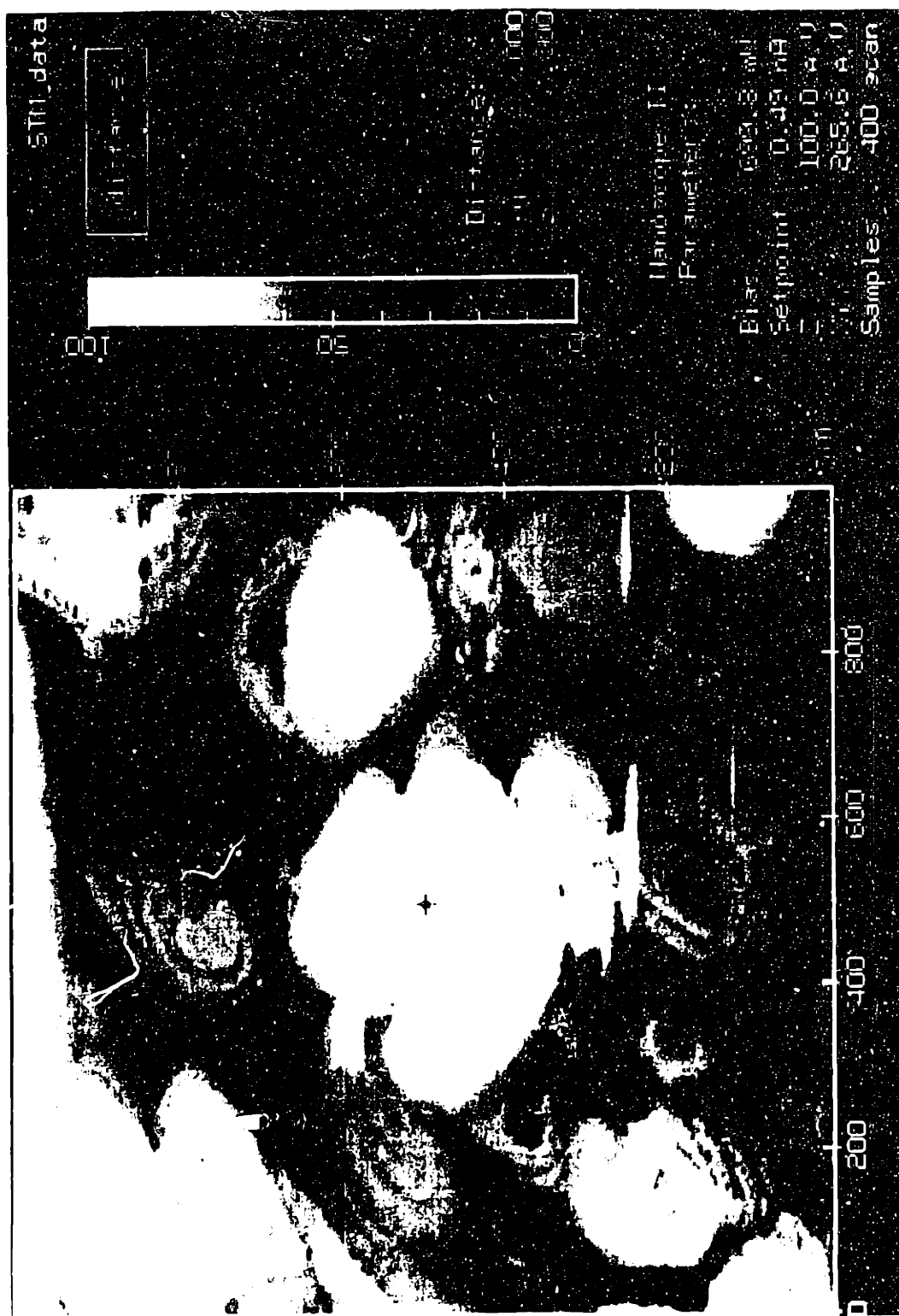


Figure 5.13 Scanning tunneling microscope image of the surface of a TFA-derived film of 70-80 nm thickness.

results presented in Figures 3.9, 5.11, and 5.12 of this thesis suggest, at least indirectly, that stacking faults play a role in flux pinning at low fields in high- J_c films.

Stacking faults may contribute to flux pinning if they produce regions in the film in which the superconducting order parameter is sharply depressed. Intergrowths of other Ba-Y-Cu-O phases in the superconducting films will act as flux pinning sites if they become normal under the temperature and field conditions used in a given application or measurement. Intergrowths of the 80 K 214 superconductor, for example, may be driven normal by the self-field at high current densities in transport measurements at 77 K. The strain field surrounding a dislocation core can also produce a local depression in the order parameter.¹⁴⁶ Where stacking faults of the 214 type intersect with the matrix 213 BYC, edge dislocations in the a-b plane (with Burger's vector parallel to the c-axis) are formed due to the presence of an additional CuO plane in the 214 structure.^{129, 147} This is shown schematically in Figure 5.14. These defects do not have the favorable orientation for pinning flux vortices along the c-axis of the films that growth derived screw dislocations possess. They are, however, highly strained locally and are probably effective core-type pinning sites. Moreover, published TEM studies of *in situ* derived BYC films¹²⁴ as well as our studies of both *in situ* and *ex situ* films suggest stacking faults and associated dislocations occur frequently in films produced over a considerable range of growth conditions.

Recent experiments by Liebenberg et al.⁸², in which large magnetic fields were applied at varying orientations relative to the c-axis of the TFA-derived BYC films, have detected the same anisotropy in high field J_c as observed in other high quality BYC films.¹⁴⁸ The reduction of critical current density with increasing field strength for fields applied both in the (001) plane (90°) and parallel to the c-axis (0°) is shown in Figure 5.15, for a TFA-derived film of 200-250 nm thickness. The more gradual decrease in J_c with H_{app} for the 90° field orientation indicates stronger pinning of flux vortices that run parallel to the basal plane. Although the intrinsic anisotropy of the superconducting properties of $Ba_2YCu_3O_{7-x}$ is believed to be responsible for anisotropic flux vortex pinning in BYC single crystals¹⁴⁹, the higher critical current densities obtained in epitaxial films

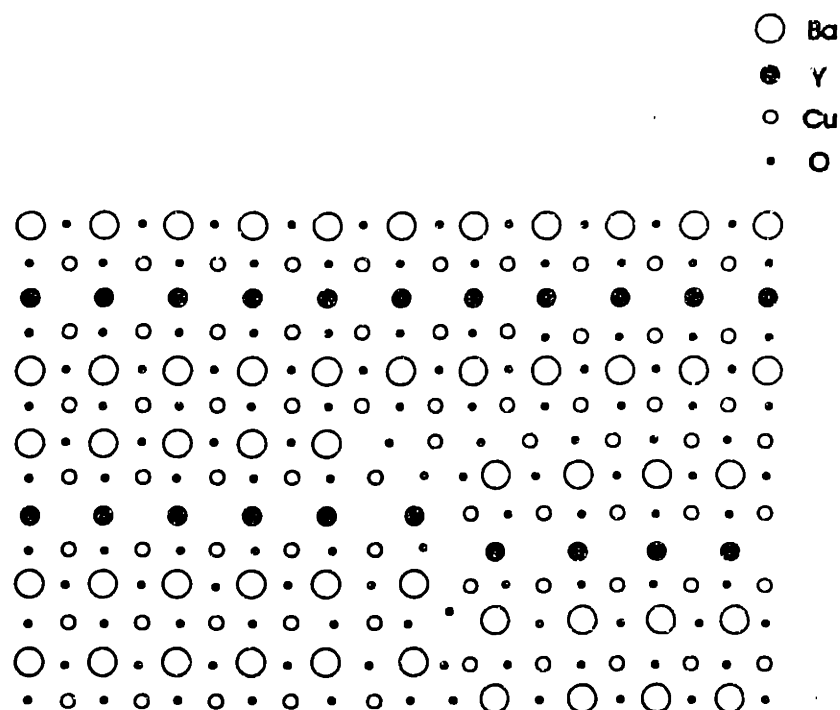


Figure 5.14 Schematic depiction of a CuO dislocation formed when a 214-type stacking fault terminates at a region of fault-free 213.

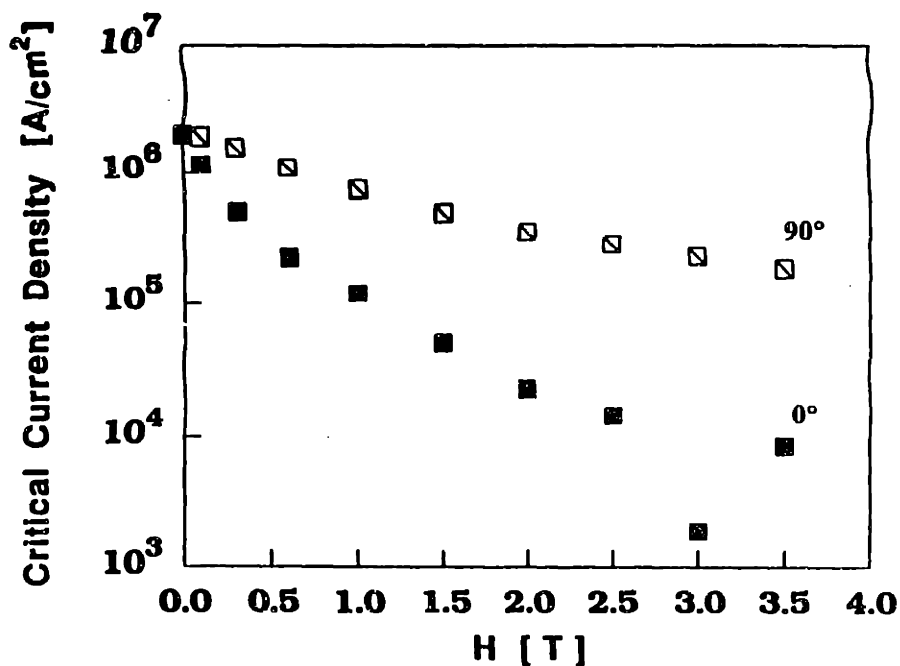


Figure 5.15 Critical current density ($T = 77$ K) of a TFA-derived film of 200-250 nm thickness annealed at 830°C in 250 ppm oxygen as a function of applied magnetic field for two field orientations: parallel to the (001) plane (90°) and parallel to the c-axis (0°).

imply that the nature of the pinning defects may also play an important role. The presence of stacking faults and edge dislocations in the (001) plane, as discussed above, may contribute to the behavior shown in Figure 5.15.

It is possible that the polytypoidal stacking faults in Figures 1 and 2 are indicators of a mode of BYC film growth that produces other structural defects that may act as flux pinning sites. McElfresh et al.¹⁴⁵ analyzed the possible role of surface topography in pinning flux vortices in their discussion of flux pinning in *in situ* derived BYC thin films. Variations in the thickness of superconducting thin films are known to enhance flux pinning in low T_c superconductors.^{150, 151} This effect arises because the energy of a flux line decreases as the thickness of material through which it passes decreases. Vortices, therefore, may be pinned at the steps that occur frequently on the surface BYC films. McElfresh et al.¹⁴⁵ calculated that the pinning force (per unit vortex line length) for a single unit cell step on the surface of a film of 50 nm thickness would be $F_p \sim 3.4 \times 10^{-5}$ N/m. This corresponds to a J_c of $\sim 2 \times 10^6$ A/cm² at 5 K, in the single vortex limit. The zero-field J_c 's of high quality BYC thin films are typically $\sim 5 \times 10^7$ A/cm² at 5 K; however, F_p for this pinning mechanism is proportional to the step height and varies as the inverse of the film thickness. Much higher J_c 's could be produced by sufficiently large steps in thin films. McElfresh et al.¹⁴⁵ pointed out the possibility that surface steps may provide the very high density of pinning sites required for vortex pinning in high magnetic fields. In addition, film defects such as pin holes, where the film thickness drops abruptly to zero, may act as fairly strong pinning sites, perhaps contributing to zero-field J_c .

The dependence of J_c on thickness of the chemically derived BYC films also correlates with observed changes in film morphology. The effect of film thickness on the surface structure of these films was indicated in Chapter 3 in Figure 3.10. It is possible that the decrease in surface roughness with increasing thickness that is evident in Figures 3.10a-3.10c contributes to the decrease in J_c with film thickness that is shown in Figure 3.9. The reduction in porosity of the chemically derived BYC films that occurs as the

film thickness increases may be particularly significant given that the edges of the holes may pin flux vortices quite strongly.

5.5 SUMMARY

Common morphological defects on the TFA-derived films include pin holes, 90°-misoriented BYC outgrowths, and second phase surface particles. As discussed in Chapter 4, formation of the faceted pin holes may result from the volume change on transformation of the polyphase intermediate film to BYC. The c_{\parallel} outgrowths were found to have apparently clean, atomically abrupt 90° grain boundaries with the matrix c_{\perp} film. Micro-chemical analysis using EDS established that three types of non-BYC surface particles were present on the films: $Y_2Cu_2O_5$, $BaSO_4$, and CuO . The presence of these particles was consistent with sulfur contamination of the film during high temperature annealing. Efforts to eliminate possible sources of sulfur contamination from the furnace environment resulted in a reduction in the density of these surface particles, but not their elimination.

An inhomogeneous distribution of polytypoidal stacking faults was observed through the thickness of chemically derived $Ba_2YCu_3O_{7-x}$ films by TEM cross-sectional imaging. A decrease in the density of polytypoidal stacking faults was detected with increasing distance above the film/substrate interface in films of greater than 200 nm thickness. Microstructural variations through the film thickness may have been caused by differences in temperature during growth of the initial layers of BYC compared to that during growth of the upper portion of the film. The abrupt change in defect density observed in some regions of the thicker films is also consistent with a sudden change in the growth mechanism of the BYC, perhaps due to removal of fluorine from the unconverted film before the transformation to BYC was complete. The reduced J_c in zero applied magnetic field that has been observed in thicker chemically derived BYC thin films suggests that the presence of polytypoidal stacking faults may improve flux vortex pinning. However, the reduction in surface roughness and pin hole density that occurs

as the film thickness is increased may also contribute to the decrease in J_c of the thicker films.

CHAPTER 6

CONCLUSIONS AND FUTURE WORK

6.1 CONCLUSIONS

The work reported in this thesis included the development of a reproducible process for synthesizing high temperature superconducting films of $\text{Ba}_2\text{YCu}_3\text{O}_{7-x}$ from metalorganic solution precursors. Post-deposition annealing conditions that resulted in the preparation of heteroepitaxial thin films of BYC with superconducting properties similar to those of the best films prepared by alternate techniques were identified. The epitaxial nucleation and growth processes of the films were studied using X-ray diffraction and high resolution TEM. These studies indicated the importance of the substrate surface structure on the c-axis orientation of the films, and provided insight into the process of phase development during the high temperature anneal. Morphological and extended crystallographic defect structures were also characterized by TEM, STEM, and several other techniques. The following specific conclusions can be drawn from these results:

- 1) A reproducible process for preparing chemically derived BYC films of 70-80 nm thickness with $T_c (R=0) > 92 \text{ K}$ and $J_c (H_{app}=0, T=77 \text{ K}) > 5 \times 10^6 \text{ A/cm}^2$ was demonstrated. The superconducting properties and crystalline quality of the films were best and the amount of c_1 orientation was smallest when the growth anneal was performed at 830° in a mixed N_2/O_2 atmosphere containing 250 ppm oxygen. The smoothness and density of the films were also enhanced by increasing the film thickness,

although this was found to reduce the J_c below that measured in films of 70-80 nm thickness.

2) Large, artificially prepared steps in the (001) LaAlO_3 surface were observed to act as preferred nucleation sites for c_1 crystallites in both *ex situ* TFA-derived and *in situ* pulsed laser deposited BYC films. Comparisons of the microstructures of films synthesized by the two techniques indicated that, for the growth conditions investigated, the ratio of growth rate to nucleation rate of the BYC appeared to be greater in the TFA-derived films than in the *in situ* derived films. Shear strain accompanying the rhombohedral-cubic phase transformation during heating of the substrates to the post-deposition annealing temperature may cause formation of large native steps on portions of the (001) LaAlO_3 surface. Steps that were native to the substrate surface also appeared to act as preferred sites for c_1 nucleation.

3) Studies of TFA-derived films quenched from the ramp segment of the growth heat treatment (in 250 ppm oxygen) indicated heterogeneous nucleation of the BYC occurred on the LaAlO_3 surface between 720 and 770°C. The transformation of the intermediate film to BYC proceeded by early coalescence of the film by growth of c-axis normal BYC parallel to the substrate surface, and slower growth upward into a polycrystalline overlayer that, upon quenching, contained BaCuO_2 , CuO , and BaF_2 (detected by XRD). Characterization of the chemistry of the quenched films by EDS in STEM suggested that both $\text{Y}_2\text{Cu}_2\text{O}_5$ and BaY_2CuO_5 were also present in the intermediate overlayer. The porosity present in the intermediate film prior to the transformation to BYC did not appear sufficient to account for the porosity observed in the final films of 70-80 nm thickness. The volume change of the film on transformation to BYC may be responsible for the additional porosity.

4) The rapid coalescence of the c-axis normal BYC into a continuous film suggested that the growth kinetics may be enhanced by the presence of a liquid phase in the transformation temperature range. Results of thermal analysis of the intermediate material

were consistent with partial melting at $\sim 715^{\circ}\text{C}$ in a 270 ppm oxygen atmosphere.

5) Morphological defects in the films included 90° -misoriented BYC grains, second-phase surface particles, and faceted pin holes. High resolution TEM examination indicated the 90° grain boundaries separating the c_{\perp} and c_{\parallel} orientations were atomically abrupt. Micro-chemical analysis indicated the surface particles were BaSO_4 , CuO , and $\text{Y}_2\text{Cu}_2\text{O}_5$, implying they result from contamination of the film by sulfur. Elimination of obvious potential sources of sulfur contamination in the high temperature furnace environment reduced the density of surface particles, but did not eliminate them.

6) The density of polytypoidal stacking faults in the TFA-derived c-axis normal BYC films varied through the film thickness. The fault density was highest near the film/substrate interface. In some areas, a sudden transition from highly faulted film to relatively fault-free BYC was observed at a certain (variable) height above the LaAlO_3 surface. A more gradual drop in stacking fault density with distance from the interface was observed in other film regions. These observations, when combined with the observed reduction in zero-field J_c with film thickness, suggest that the stacking faults and/or associated edge dislocations play a significant role in flux vortex pinning at low magnetic induction.

Implications for epitaxy in other MOD-derived oxide films

The results described in this thesis demonstrate that epitaxy is possible in oxide thin films derived from metalorganic solution precursors. However, the epitaxial mechanism of TFA-derived BYC films differs in several important respects from mechanisms observed in other epitaxial oxides prepared by MOD. Observations described in Chapter 4 suggest that a fluorine-containing liquid phase is present in the heat treatment temperature range in which nucleation and growth of the TFA-derived films occurs. This melt may enhance the transformation and densification kinetics of the BYC films. The relatively low transformation temperatures and short annealing times required

in preparing these epitaxial BYC films contrast with annealing conditions required for epitaxial grain growth of oxides.^{70, 73, 128} The solid phase heteroepitaxial nucleation and growth mechanism described by Nashimoto et al.⁷⁵ for LiNbO_3 films is not inconsistent with low growth temperatures; however, the solid phase process typically results in films with significant porosity. The high relative densities of the TFA-derived BYC films shown in Figure 3.10, for example, is consistent with improved densification of the films due to the presence a wetting liquid phase. The results presented herein indicate that much of the porosity that is present in the final TFA-derived BYC films is due to volume changes on transformation of the intermediate compounds and not to residual porosity from decomposition of the metalorganic precursor.

The success of this method in preparing high quality epitaxial BYC thin films, particularly compared to results reported for MOD by other investigators^{52, 55, 56}, can be ascribed to the chemistry of the intermediate films that result from decomposition of the metal trifluoroacetate precursors. Formation of BaF_2 instead of BaCO_3 as an intermediate compound allows full transformation to BYC to occur at low temperatures through reaction with water vapor. Furthermore, the presence of fluorine in the intermediate films appears to result in partial melting at lower temperatures than would occur in the ternary oxide system.

6.2 FUTURE WORK

Several important issues arising from the work done in this thesis project remain to be clarified. The effect of substrate surface steps on nucleation of the BYC film is not yet fully understood. The results reported in Chapter 4 suggest that large native steps in (001) LaAlO_3 act as preferred sites for c_1 nucleation. The size and structure of the steps that are most effective nucleation sites for c_1 grains has not been determined, however. Nucleation of BYC on substrate steps that are not as large as those produced by the ion etching process could be studied by polishing single crystal substrates at a slight misorientation from the (001) plane to produce a vicinal surface. These experiments

would involve AFM characterization of the step structure of both the initial vicinal surfaces and the surfaces after annealing the substrates using the standard high temperature heat treatment. The microstructure (orientation, approximate nucleus density) of the BYC films deposited and annealed on the substrates would be characterized by cross-sectional TEM. The AFM studies of the nominally flat (001) perovskite-like single crystal substrates surface recently initiated by Chang¹²⁷ could be continued to characterize variations in the step density and height across the substrates. By determining the ledge separation and height in the same locations on substrates before and after annealing, it may be possible to confirm the role of the *r-c* transformation of LaAlO₃ in generating surface steps. The well-defined 90° [100] tilt boundaries in TFA-derived films on the artificially stepped substrates are also interesting, and their I-V characteristics deserve study. The tendency of the TFA-derived BYC films to form isolated *c*₁ grains on the step slopes may make them useful for applications in Josephson electronics.

A more quantitative understanding of the transformation process could be developed by measuring the volume fraction of the intermediate film transformed to BYC as a function of hold time at various post-deposition annealing temperatures. The activation energy for the transformation can be determined from this data by assuming an Arrhenius relationship between transformation rate and temperature. The TEM observations of quenched films reported in Section 4.3 of this thesis indicate there may be two relevant activation energies: that associated with growth in the basal plane of the *c*-axis normal BYC, which is most significant prior to coalescence of the BYC islands into a continuous film; and that associated with growth parallel to the *c*-axis (or nucleation of the next BYC layer), which is important after coalescence. A similar situation that involved chemical reactions between thin films in which separate interfacial and normal growth events occurred was studied by Coffey et al.¹⁵² These workers used an Avrami¹⁵³ analysis to model the volumetric rate of transformation of reactant films to a single product phase. In this case, calorimetric measurements indicated the same activation energy for both interfacial and normal growth of the product film.¹⁵² The highly anisotropic layered crystal structure of BYC suggests, however, that the activation energy for growth along

the BYC/LaAlO₃ interface plane may be significantly lower than that for growth upward, parallel to the c-axis.

Measurement of the fraction of the intermediate films transformed to BYC was not attempted in cross-sectional TEM studies of the quenched samples. It was not possible to prepare thinned specimens that were electron transparent over large enough areas to obtain accurate statistics on BYC film thickness. Experimental techniques suitable for obtaining this data over large areas of the film include Rutherford backscattering spectroscopy and X-ray diffraction. The former technique has been used by several groups to study epitaxial growth⁷² and regrowth⁷⁴ of (100) Si, and is suitable for characterizing the upward growth of the c-axis BYC (change in thickness of the polycrystalline overlayer) following island coalescence. The integrated intensities of the (00 l) X-ray reflections can also be used to measure the volume fraction of the film transformed as a function of time. In principle, this technique should allow characterization of the initial stage of BYC island growth, prior to island coalescence, and may make possible the determination of both the activation energy for growth in the (001) plane and that for growth in the [001] direction. As described in Section 4.3, it was not possible to use the integrated intensities of XRD reflections as a measure of the fraction of the intermediate film transformed to BYC because the peak intensities varied from sample to sample due to slight misorientations of the specimens in the goniometer. Access to a four-circle diffractometer, in which each sample could be accurately rotated into the orientation that maximized the substrate/film peak intensities, would make possible quantitative XRD characterization of the transformation kinetics.

Further characterization of the fine surface structure of the chemically derived BYC films using STM and/or AFM is needed to confirm the preliminary observations of a terraced island morphology. The observed variation in polytypoidal stacking fault density through the thickness of the films suggests that the nature of the film growth mechanism may change during growth of the thicker films. This may be reflected in changes in the film morphology with thickness. More accurate measurements of thickness

variations (from surface steps and depressions) in the TFA-derived BYC films would also indicate the degree to which these variations may contribute to flux pinning in the films.¹⁴⁵ Measurements of the effect of applied magnetic field orientation on J_c suggest the flux pinning mechanisms in BYC thin films are highly anisotropic.¹⁴⁸ The high critical current densities measured when fields are applied parallel to the a - b plane is qualitatively consistent with vortex pinning at crystallographic defects that lie in the (001) plane, such as the polytypoidal stacking faults and associated edge dislocations. Further work will be undertaken to determine the field-orientation effect on the J_c of thicker TFA-derived films which have lower volumetric stacking fault density than the thinner films already studied.^{82, 154}

BIBLIOGRAPHY

1. M.K. Wu, J.R. Ashburn, G.J. Tomng, P.H. Hor, R.L. Meng, L. Gao, Z.J. Huang, Y.Q. Wang, and C.W. Chu, *Phys. Rev. Lett.* **58**, 908 (1987).
2. H. Maeda, Y. Tanaka, M. Fukutomi, and T. Asano, *Jpn. J. Appl. Phys., Part 2* **27**, L209 (1987).
3. Z.Z. Sheng and A.M. Hermann, *Science* **332**, 55 (1988).
4. K. Sandhage, C.N. Riley, W.L. Carter, *J. Metals* **43**, 21 (1991).
5. D. Larbalestier, *Physics Today* **44**, 74 (1991).
6. A. Inam, M.S. Hegde, X.D. Wu, T. Venkatesan, P. England, P.F. Miceli, E.W. Chase, C.C. Chang, J. M. Tarascon, and J.B. Wachtman, *Appl. Phys. Lett.* **53**, 908 (1988).
7. P.M. Mankiewich, J.H. Scofield, W.J. Skoepol, R.E. Howard, A.H. Dayem, and E. Good, *Appl. Phys. Lett.* **51**, 1753 (1987).
8. A.C. Westerheim, P.C. McIntyre, S.N. Basu, D. Bhatt, L.S. Yu-Jahnes, A.C. Anderson, and M.J. Cima; submitted to *J. Electron. Mater.* (1993).
9. P.C. McIntyre, M.J. Cima, and M.F. Ng, *J. Appl. Phys.* **68**, 4183 (1990).
10. J.D. Jorgensen, M.A. Beno, D.G. Hinks, L. Soderholm, K.J. Volin, R.L. Hitterman, J.D. Grace, Ivan Schuller, C.U. Segre, K. Zhang, and M.S. Kleefisch, *Phys. Rev. B* **36**, 3608 (1987).
11. R.J. Cava, *Science* **247**, 656 (1990).
12. O.R. Monteiro and S.M. Johnson, *J. Am. Ceram. Soc.* **73**, 1159 (1990).
13. S-W. Chan, D.M. Hwang, and L. Nazar, *J. Appl. Phys.* **65**, 4719 (1989).
14. H.J. Scheel and P. Niedermann, *J. Crystal Growth* **94**, 281 (1989).
15. J.W. Matthews, *Epitaxial Growth, Part B.*, (Academic Press, New York, NY, 1975), pp. 437-492.
16. P.S. Peercy, E.G. Bauer, B.W. Dodson, D.J. Ehrlich, L.C. Feldman, C.P. Flynn,

- M.W. Geis, J.P. Harbison, R.J. Matyi, P.M. Petroff, J.M. Phillips, G.B. Stringfellow, A. Zangwill, *J. Mater. Res.* **5**, 852 (1990).
17. E. Bauer, *Z. Cryst.* **110**, 372 (1958).
 18. F.C. Frank and J.H. van der Merwe, *Proc. Roy. Soc. A* **198**, 216 (1949).
 19. R. Bruinsma and A. Zangwill, *Europhys. Lett.* **4**, 729 (1987).
 20. M.H. Grabow and G.H. Gilmer, *Surf. Sci.* **194**, 333 (1988).
 21. O. Meyer, F. Weschenfelder, J. Geerk, H.C. Li, and G.C. Xiong, *Phys. Rev. B* **37**, 9757 (1988).
 22. L.A. Tietz, C.B. Carter, D.K. Lathrop, S.E. Russek, R.A. Buhrman, and J.R. Michael, *J. Mater. Res.* **4**, 1072 (1989).
 23. R.W. Simon, C.E. Platt, A.E. Lee, G.S. Lee, K.P. Daly, M.S. Wire, J.A. Luine, and M. Urbanik, *Appl. Phys. Lett.* **53**, 2677 (1988).
 24. R. Ramesh, D.M. Hwang, T. Venkatesan, T.S. Ravi, L. Nazar, A. Inam, X.D. Wu, B. Dutta, G. Thomas, A.F. Marshall, and T.H. Geballe, *Science* **247**, 57 (1990).
 25. B.H. Moeckly, S.E. Russek, D.K. Lathrop, R.A. Buhrman, J. Li, and J.W. Mayer, *Appl. Phys. Lett.* **57**, 1687 (1990).
 26. M.G. Norton and C.B. Carter, *Scanning Microscopy* **6**, 385 (1992).
 27. S. Geller and V.B. Bala, *Acta Crystallogr.* **9**, 1019 (1956).
 28. H.M. O'Bryan, P.K. Gallagher, G.W. Berkstresser, and C.D. Brandle, *J. Mater. Res.* **5**, 183 (1990).
 29. G-D. Yao, S.Y. Hou, and M. Dudley, *J. Mater. Res.* **7**, 1847 (1992).
 30. J.M. Phillips, M.P. Siegal, R.B. van Dover, T.H. Tiefel, J.H. Marshall, C.D. Brandle, G. Berkstresser, A.J. Strauss, R.E. Fahey, S. Sengupta, A. Cassanho, and H.P. Jenssen, *J. Mater. Res.* **7**, 2650 (1992).
 31. R. Ramesh, A. Inam, D.M. Hwang, T.S. Ravi, T. Sands, X.X. Xi, X.D. Wu, Q. Li, T. Venkatesan, R. Kilaas, *J. Mater. Res.* **6**, 2264 (1991).
 32. M.G. Norton and C.B. Carter, in *Laser Ablation for Materials Synthesis*, edited by D.C. Paine and J.C. Bravman (*Mater. Res. Soc. Symp. Proc.* **191**, Pittsburgh,

PA, 1990), p.165.

33. D.X. Li, X.K. Wang, Q. Li, R.P.H. Chang, and J.B. Ketterson, *J. Appl. Phys.* **66**, 5505 (1989).
34. R. Ramesh, A. Inam, D.M. Hwang, T.D. Sands, C.C. Chang, and D.L. Hart, *Appl. Phys. Lett.* **58**, 1557 (1991).
35. S.E. Babcock, *MRS Bull.* **17** [8], 20 (1992).
36. T.H. Geballe, *MRS Bull.* **17** [7], 70 (1992).
37. A.C. Westerheim, *Sputter Deposition and Characterization of In Situ Superconducting Y-Ba-Cu-O Thin Films*, Ph.D. Thesis (Department of Materials Science and Engineering, M.I.T., 1992), pp. 147-72.
38. W.A. Tiller, *The Science of Crystallization: Microscopic Interfacial Phenomena* (Cambridge University Press, New York, N.Y., 1991), p.199.
39. J.V. Mantese, A.L. Micheli, A.H. Hamdi, and R.W. Vest, *MRS Bull.* **14** [10], 48 (1989).
40. R.W. Vest, *Ferroelectrics* **102**, 53 (1990).
41. S. Hirano and K. Kato, *Adv. Ceram. Mat.* **2**, 142 (1987).
42. B.P. Chang and J.A. Smith, Jr, CPRL Report R20, MIT, p. 74 (1990).
43. B.J.J. Zelinski and D.R. Uhlmann, *J. Phys. Chem. Solids* **45**, 1069 (1984).
44. G.W. Scherer, *Yogyo-Kyokai-Shi* **95**, 21 (1987).
45. S.J. Milne and S.H. Pyke, *J. Am. Ceram. Soc.* **74**, 1407 (1991).
46. D.P. Partlow and J. Gregg, *J. Mater. Res.* **2**, 595 (1987).
47. K.T. Miller and F.G. Lange, *Mater. Res. Soc. Symp. Proc.* **155**, 191 (1990).
48. P.C. McIntyre, M.J. Cima, J.A. Smith, Jr., R.B. Hallock, M.P. Siegal, and J.M. Phillips, *J. Appl. Phys.* **71**, 1868 (1992).
49. C.E. Rice, R.B. van Dover, and G.J. Fisanick, *Appl. Phys. Lett.* **51**, 1842 (1987).
50. A.H. Hamdi, J.V. Mantese, A.L. Micheli, R.C.O Laugal, D.F. Dungan, Z.H.

- Zhang, and K.R. Padmanabhan, *Appl. Phys. Lett.* **51**, 2152 (1987).
51. M.R. Scozzafava, W.E. Rhine, and M.J. Cima, in *Better Ceramics Through Chemistry IV*, edited by B.J.J. Zelinsky, C.J. Brinker, D.E. Clark, and D.R. Ulrich (Mater. Res. Soc. Symp. Proc. **180**, Pittsburgh, PA, 1990), p. 697.
 52. M.E. Gross, M. Hong, S.H. Liou, P.K. Gallagher, and J. Kwo, *Appl. Phys. Lett.*, **52** 160 (1988).
 53. P-Y. Chu, I. Campion, and R.C. Buchanon, *J. Mater. Res.* **8**, 261 (1993).
 54. T. Nonaka, K. Kaneko, T. Hasegawa, K. Kishio, Y. Takahashi, Kobayashi, K. Kitizawa, and K. Fueki, *Jpn. J. Appl. Phys., Part 2* **27**, L867 (1988).
 55. S. Hirano, T. Hayashi, and M. Miura, *J. Am. Ceram. Soc.* **73**, 885 (1990).
 56. S.S. Pak, F.C. Montgomery, D.M. Duggan, K.C. Chen, K.S. Mazdiasni, P.K. Tsai, L.M. Paulius, and M.B. Maple, *J. Am. Ceram. Soc.* **75**, 2268 (1992).
 57. Y.L. Chen, J.V. Mantese, A.H. Hamdi, and A.L. Micheli, *J. Mater. Res.* **4**, 1065 (1989).
 58. A. Gupta, E.I. Cooper, R. Jagannathan, and E.A. Geiss, in *Chemistry of High-Temperature Superconductors II*, edited by D.L. Nelson and T.F. George (American Chemical Society, Washington, D.C., 1988), p. 265.
 59. A.M. Kazakos, S. Komarneni, and R. Roy, *J. Mater. Res.* **5**, 1095 (1990).
 60. B.A. Tuttle, T.J. Headley, B.C. Bunker, R.W. Schwartz, T.J. Zender, C.L. Hernandez, D.C. Goodnow, R.J. Tissot, J. Michael, and A.H. Carim, *J. Mater. Res.* **7**, 1876 (1992).
 61. C.K. Kwok and S.B. Desu, *J. Mater. Res.* **8**, 339 (1993).
 62. S. Desu, C. Peng, L. Kammerdiner, and P. Schuele, in *Ferroelectric Thin Films*, edited by E.R. Meyers and A.I. Kingon (Mater. Res. Soc. Symp. Proc. **200**, Pittsburgh, PA, 1990), p.319.
 63. K. Nashimoto and M.J. Cima, *Mater. Lett.* **10**, 348 (1991).
 64. S. Hirano, T. Hayashi, R.H. Baney, M. Miura, H. Tomonaga, *Chem. Lett.*, 665 (1988).
 65. Z. Wu, H.K. Chae, M.H. Frey, and D.A. Payne, *Mater. Res. Soc. Symp. Proc.*, in

press.

66. H. Endo, CPRL Report R22, MIT, p. 7-1 (1992).
67. V. Joshi, G.K. Goo, and M.L. Mecartney, in *Synthesis and Processing of Ceramics: Scientific Issues*, edited by W.E. Rhine, T.M. Shaw, R.J. Gottschall, and Y. Chen (Mater. Res. Soc. Symp. Proc. **249**, Pittsburgh, PA, 1992) p. 459.
68. M. Amini and M.D. Sacks, in *Better Ceramics Through Chemistry IV*, edited by B.J.J. Zelinsky, C.J. Brinker, D.E. Clark, and D.R. Ulrich (Mater. Res. Soc. Symp. Proc. **180**, Pittsburgh, PA, 1990), p. 675.
69. D.C. Chen, D.F. Ryder, Jr., and W.A. Spurgeon, *J. Am. Ceram. Soc.* **72**, 1495 (1989).
70. G. Braunstein, G.R. Paz-Pujalt, M.G. Mason, T. Blanton, C.L. Barnes, and D. Margevich, *J. Appl. Phys.* **73**, 961 (1993).
71. J.A. Floro and C.V. Thompson, in *Thin Film Structures and Phase Stability*, edited by B.M. Clemens and W.L. Johnson (Mater. Res. Soc. Symp. Proc. **187**, Pittsburgh, PA, 1991), p. 274.
72. B.Y. Tsaur and L.S. Hung, *Appl. Phys. Lett.* **37**, 648 (1980).
73. K.T. Miller and F.G. Lange, in *Processing Science of Advanced Materials*, edited by I.A. Aksay, G.L. McVay, and D.R. Ulrich (Mater. Res. Soc. Symp. Proc. **155**, Pittsburgh, PA, 1989), p. 155.
74. M. von Allmen, S.S. Lau, J.W. Mayer, and W.F. Tseng, *Appl. Phys. Lett.* **35**, 280 (1979).
75. K. Nashimoto, M.J. Cima, P.C. McIntyre, and W.E. Rhine; to be published in *J. Mater. Res.*
76. K. Nashimoto, CPRL Report R20, MIT, 26 (1990).
77. A.S. Shaikh and G.M. Vest, *J. Am. Ceram. Soc.* **69**, 682 (1986).
78. J-F. Campion, D.A. Payne, H.K. Chae, and Z. Xu, in *Ceramic Powder Science IV*, edited by S. Hirano, G.L. Messing, and H. Hausner (American Ceramic Society, Westerville, OH, 1991) p. 477.
79. R. Feenstra, T.B. Lindemar, J.D. Budai, and M.D. Galloway, *J. Appl. Phys.* **69**, 6569 (1991).

80. Applied Technologies Enterprises, Irmo, SC.
81. CM Inc., Bloomfield, NJ.
82. D.H. Liebenberg, P.C. McIntyre, M.J. Cima, T.A. Francavilla; *J. Cryogenics*, in press.
83. See, for example: R.J. Fessenden and J.S. Fessenden, *Organic Chemistry*, 3rd Ed. (Brooks/Cole, Monterey, CA, 1986) pp. 603-05.
84. S. Jurgenson, unpublished work.
85. J.A. Smith, Jr., unpublished work.
86. P.C. McIntyre, M.J. Cima, M.F. Ng, R.C. Chiu, and W.E. Rhine, *J. Mater. Res.* **5**, 2771 (1990).
87. A. Mogro-Campero and L.G. Turner, *Appl. Phys. Lett.* **58**, 417 (1991).
88. M.P. Siegal, S.Y. Hou, J.M. Phillips, T.H. Tiefel, and J.H. Marshall, *J. Mater. Res.* **7**, 2658 (1992).
89. B.T. Ahn, V.Y. Lee, R. Beyer, T.M. Gür, and R.A. Huggins, *Physica C* **167**, 529 (1990).
90. R. Beyers and B.T. Ahn, *Annu. Rev. Mater. Sci.* **21**, 335 (1991).
91. M.P. Siegal, J.M. Phillips, R.B. van Dover, T.H. Tiefel, and J.H. Marshall, *J. Appl. Phys.* **68**, 6353 (1990).
92. T.B. Lindemer, J.F. Hunley, J.E. Gates, A.L. Sutton, Jr., J. Brynestad, and C.R. Hubbard, *J. Am. Ceram. Soc.* **72**, 1775 (1989).
93. X.P. Jiang, M.J. Cima, H.D. Brody, J.S. Haggerty, and M.C. Flemings; pp. 259-60 in *Proceedings of the International Workshop on Superconductivity*, Sponsored by ISTEK and MRS, Honolulu, HA, 1992.
94. S.N. Basu T. Roy, T.E. Mitchell, R.E. Muenchausen, and M.A. Nastasi, in *Proc. Conf. Science and Technology of Thin Film Superconductors*, edited by R. McConnell and R. Noufi, in press.
95. C.W. Nieh, L. Anthony, J.Y. Josefowicz, and F.G. Krajenbrink, *Appl. Phys. Lett.* **56**, 2138 (1990).

96. M.G. Norton and C.B. Carter, *J. Crystal Growth* **110**, 641 (1991).
97. H.I. Smith, M.W. Geis, C.V. Thompson, and H.A. Atwater, *J. Crystal Growth* **63**, 527 (1983).
98. D. Eissler, H.S. Wang, and W. Dietsche, *Appl. Phys. Lett.* **62**, 1292 (1993).
99. F.R.N. Nabarro, *Theory of Crystal Dislocations* (Dover, New York, NY, 1987).
100. C. Gerber, D. Anselmetti, J.G. Bednorz, J. Mannhart, and D.G. Schlom, *Nature* **360**, 279 (1991).
101. M. Hawley, I.D. Raistrick, J.G. Beery, and R.J. Houlton, *Science* **251**, 1587 (1991).
102. H.P. Lang, T. Frey, and H-J. Güntherodt, *Europhys. Lett.* **15**, 667 (1991).
103. W.K. Burton, N. Cabrera, and F.C. Frank, *Phil. Trans. Roy. Soc.*, **A243**, 299 (1951).
104. K.A. Jackson in *Liquid Metals and Solidification*, (American Society of Metals, Metals Park, OH, 1958), p. 180.
105. W.D. Kingery, H.K. Bowen, D.R. Uhlmann, *Introduction to Ceramics*, 2nd Ed. (Wiley-Interscience, New York, NY, 1976), pp. 336-46.
106. A. Roshko, NIST, Boulder, CO; personal communication, 1992.
107. A. Roshko, unpublished work.
108. Y. Tazoh and S. Miyazawa, *Appl. Phys. Lett.* **62**, 408 (1993).
109. C.L. Jia, B. Kabius, K. Urban, K. Herrmann, J. Schubert, W. Zander, and A.I. Braginski, *Physica C* **196**, 211 (1992).
110. M.A. Parker, T.L. Hylton, and J.K. Howard, *Mater. Res. Soc. Symp. Proc.*, in press.
111. C.L. Jia, B. Kabius, K. Urban, K. Herrmann, G.J. Cui, J. Schubert, W. Zander, A.I. Braginski, and C. Heiden, *Physica C* **175**, 545 (1991).
112. R.W. Simon, J.B. Bulman, J.F. Burch, S.B. Coons, K.P. Daly, W.D. Dozier, R. Hu, A.E. Lee, J.A. Luine, C.E. Platt, S.M. Schwarzbek, M.S. Wire, and M.J. Zani, *IEEE Trans. Magn.* **27**, 3209 (1991).

113. C.B. Eom, A.F. Marshall, S.S. Laderman, R.D. Jacowitz, and T.H. Geballe, *Science* **249**, 1549 (1990).
114. A.H. Carim and T.E. Mitchell, *Ultramicroscopy*, to be published.
115. Y. Gao, G. Bai, D.J. Lam, and K.L. Merkle, *Physica C* **173**, 487 (1991).
116. C.B. Eom, A.F. Marshall, Y. Suzuki, B. Boyer, R.F.W. Pease, and T.H. Geballe, *Nature* **353**, 544 (1991).
117. C.B. Eom, A.F. Marshall, Y. Suzuki, T.H. Geballe, B. Boyer, R.F.W. Pease, R.B. van Dover, and J.M. Phillips, *Phys. Rev. B* **46**, 11902 (1992).
118. A.F. Marshall and C.B. Eom, *Physica C* **207**, 239 (1993).
119. J.Z. Sun, IBM, Yorktown Heights, NY; personal communication, 1993.
120. J.F. Benedict, S.J. Klepeis, W.G. Vandygrift, and R. Anderson, *Electron Microscopy Soc. Am. Bull.*, **19** [11], 74 (1989).
121. M-Bond 610; Measurements Group, Inc., Raleigh, NC.
122. Crystalbond; Aremco Products, Inc., Ossining, NY.
123. VCR D500i dimpler; VCR Group, Inc., South San Francisco, CA.
124. R. Ramesh, D.M. Hwang, J.B. Barner, L. Nazar, T.S. Ravi, A. Inam, B. Dutta, X.D. Wu, and T. Venkatesan, *J. Mater. Res.* **5**, 704 (1990).
125. D. Dimos, P. Chaudhari, and J. Mannhart, *Phys. Rev. B*, **41**, 4038 (1990).
126. C. Traeholt, J.G. Wen, V. Svetchnikov, A. Delsing, and H.W. Zandbergen, *Physica C* **206**, 318 (1993).
127. B.P. Chang, unpublished work.
128. K.T. Miller, C-J. Chan, M. Cain, and F.F. Lange; *J. Mater. Res.*, in press.
129. J.G. Wen, C. Traeholt, and H.W. Zandbergen, *Physica C* **205**, 354 (1993).
130. R. Ramesh, C.C. Chang, T.S. Ravi, D.M. Hwang, A. Inam, X.X. Xi, Q. Li, X.D. Wu, and T. Venkatesan, *Appl. Phys. Lett.* **57**, 1064 (1990).
131. S.C. Peterson, *Fabrication of Textured Ba₂YCu₃O_{7-x} Superconducting Films on*

Non-Epitaxial Substrates, Ph.D. Thesis (Department of Materials Science and Engineering, M.I.T., 1992).

132. P.E.D. Morgan, R.M. Housley, J.R. Porter, and J.J. Ratto, *Physica C* **176**, 279 (1991).
133. S.E. Babcock, X.Y. Cai, D.L. Kaiser, and D.C. Larbalestier, *Nature* **347**, 167 (1990).
134. R.B. van Dover, E.M. Gyorgy, L.F. Schneemeyer, J.W. Mitchell, K.V. Rao, R. Puzniak, and J.V. Waszczak, *Nature* **342**, 55 (1989).
135. L. Civale, A. Marwick, M.W. McElfresh, A.P. Malozemoff, F. Holtzberg, J.R. Thompson, and M.A. Kirk, *Phys. Rev. Lett.* **65**, 1164 (1990).
136. S. Vadlamannati, P. England, N.G. Stoffel, R. Ramesh, T.S. Ravi, D.M. Hwang, A. Findikoglu, Q. Li, T. Venkatesan, and W.L. McLean, *Appl. Phys. Lett.* **57**, 2267 (1990).
137. R.A. Camps, J.E. Evetts, B.A. Glowacki, S.B. Newcomb, R.E. Somekh, and W.M. Stobbs, *Nature* **329**, 229 (1987).
138. S. Nakahara, G.J. Fisanick, M.F. Yan, R.B. van Dover, T. Boone, and R. Moore, *J. Crystal Growth* **85**, 639 (1987).
139. S.E. Babcock and D.C. Larbalestier, *Appl. Phys. Lett.* **55**, 393 (1989).
140. M.F. Chisholm and S.J. Pennycook, *Nature* **351**, 47 (1991).
141. D.J. Carlson, M.P. Siegal, J.M. Phillips, T.H. Tiefel, and J.H. Marshall, *J. Mater. Res.* **5**, 2797 (1990).
142. A.F. Marshall, R.W. Barton, K. Char, A. Kapitulnik, B. Oh, R.H. Hammond, and S.S. Laderman, *Phys. Rev. B.* **37**, 9353 (1988).
143. R. Ramesh, A. Inam, T. Sands, and C.T. Rogers, *Mater. Sci. and Eng. B.* **14**, 188 (1992).
144. T.L. Hylton and M.R. Beasley, *Phys. Rev. B.* **41**, 11669 (1990).
145. M. McElfresh, T.G. Miller, D.M. Schaefer, R. Reifenberger, R.E. Muenchausen, M. Hawley, S.R. Foltyn, and X.D. Wu, *J. Appl. Phys.* **71**, 5099 (1992).
146. A.M. Campbell and J.E. Evetts, *Adv. Phys.* **21**, 191 (1972).

147. R. Kontra, *An Electron Microscopy Study of Phase Transformations in Yb-Ba-Cu-O Superconductors*, Sc.D. Thesis (Department of Materials Science and Engineering, M.I.T., 1992).
148. B. Roas, L. Schultz, and G. Saemann-Ischenko, *Phys. Rev. Lett.* **64**, 479 (1990)
149. V. Selvamanickam, K. Forster, and K. Salama, *Physica C* **178**, 147 (1991).
150. D.D. Morrison and R.M. Rose, *Phys. Rev. Lett.* **25**, 356 (1970).
151. A.T. Fiory, A.F. Hebard, and S. Somekh, *Appl. Phys. Lett.* **32**, 73 (1978).
152. K.R. Coffey, L.A. Clevenger, K. Barmak, D.A. Rudman, and C.V. Thompson, *Appl. Phys. Lett.* **55**, 852 (1989).
153. M. Avrami, *J. Chem. Phys.* **7**, 1103 (1939); **8**, 212 (1940); **9**, 177 (1941).
154. P.C. McIntyre, M.J. Cima, D.H. Liebenberg, T.A. Francavilla, *Appl. Phys. Lett.* **58**, 2033 (1991).
155. E.A. Geiss, R.L. Sandstrom, W.J. Gallagher, A. Gupta, S.L. Shinde, R.F. Cook, E.I. Cooper, E.J.M. O'Sullivan, J.M. Roldan, A.P. Segmüller, J. Angilello, *IBM J. Res. Development* **34**, 916 (1990).
156. JCPDS file 4-452.
157. *ibid.*, file 38-1402.
158. *ibid.*, file 25-1200.
159. *ibid.*, file 33-511.
160. *ibid.*, file 5-661.
161. *ibid.*, file 38-1434.
162. *ibid.*, file 38-1433.